X-ray absorption spectroscopy studies on the structure and the catalytic activity of nickel phosphide catalysts

X 線吸収分光法によるニッケルリン化物触媒の構造と触媒特性の研究

Md. Harun Al Rashid

Division of Quantum Science and Engineering,
Graduate School of Engineering, Hokkaido University

September 2021

Table of Contents

Chapter 3:   EXAFS curve fitting analysis for NOCM catalytic active phase determination of Ni phosphide catalysts

Chapter 4:   Theoretical XAFS Analysis of Nickel Phosphide Catalysts with Different Initial Ni and P ratios for NOCM Reactions

Chapter 5:   XANES analysis of nickel phosphide complex system using Full Potential Multiple Scattering (FPMS)

List of Abbreviations

ASP:	Advanced Photon Source
BL:	Beam Line
CF:	Curve Fitting
DCM:	Dehydrogenative Conversion of Methane
ESRS:	European Synchrotron Radiation Source
EXAFS:	Extended X-ray Absorption Fine Structure
EC:	Empty Cell
FP:	Full Potential
FMS:	Full Multiple Scattering
FT:	Fourier Transform
FPMS:	Full Potential Multiple Scattering
FTS:	Fischer-Tropsch Synthesis
GWP:	Global Warming Potential
LEED:	Low Energy Electron Diffraction
MST:	Multiple Scattering Theory
MT:	Muffin Tin
MDA:	Methane Dehydroaromatization
NMT:	Non Muffin Tin
NOCM:	Non-oxidative Coupling of Methane
OCM:	Oxidation Coupling of Methane
PEEM:	Photoemission Electron Microscopy
STM:	Scanning Tunneling Microscopy
SR:	Synchrotron Radiation
SCF:	Self-consistent Field
STEM:	Scanning Transmission Electron Microscopy
TM:	Transition Metal
XAFS:	X-ray Absorption Fine Structure
XANES:	X-ray Absorption Near Edge Structure
XRD:	X-ray Diffraction
XRF:	X-Ray Fluorescence
XAS:	X-ray Absorption Spectroscopy

Acknowledgments

Chapter 1

General Introduction

1.1. Introduction

Catalysts play an important role both economically and environmentally in the industry. It is widely used in various chemical industrial processes such as polymers, petrochemical, agrochemicals, pharmaceuticals, the environmental sector, etc.[1–4] About 75%-80% of chemical products required a catalyst to manufacture them at any stage.[5,6] It is well understood that catalysts are a substance which promotes the reactions without itself any change or being consumed in the chemical reaction. Without the use of catalysts, the reaction will occur with a very low reaction rate. One of the alternatives to improve the reaction rate is to increase the temperature or the pressure to improve the conversion rate. But this process may lead the severe conditions with undesirable energy consumption and damaged instruments and materials. Another use of catalysts is to increase the selectivity toward the desired product, reducing the waste of reactants, time, and energy. That's why more than 20% of all industrial products depend on catalysts.[7] Therefore, catalysis is omnipresent, but finding out efficient catalysts among the various catalysts is always challenging in the catalysis processes. The efficiency of the catalytic process generally depends on the performance of catalyst activity. There are three factors to determine the performance of the catalysts: reaction rate, lifetime, selectivity. These three factors determine the efficiency of the catalyst for any reactions. On the other hand, various factors govern the catalytic activity, such as the number of dispersing atoms on the surface, atomic arrangement, local structure, and nature of the atom. Finding efficient catalysts will be the next research topic globally because of the high production rate, selectivity, low cost, and environmental friendliness. In catalyst synthesis, efficient catalysts require atomic-level characterization because tiny atoms or only specific locations termed active center play an important role in causing a change in their activities and properties.

Methane conversion is an essential reaction because methane is a good candidate for the alternative feedstock of petroleum to produce organic materials. Catalysts can play an important role in most processes for methane conversion. From the 1990s to the recent, hundreds of catalytic materials have been synthesized and examined.[8–11] Unfortunately, the presence of O_2 leads large amount of the thermodynamically stable

products CO_2 and H_2O. The commercial use of oxidation coupling of methane (OCM) to higher hydrocarbon cannot achieve acceptable selectivity.[12,13] Another remarkable problem is the deactivation of the catalyst during catalytic conversion of methane due to coke deposition.[14–16] Despite a large research effort on the direct conversion of methane during the last few years, no promising processes have been developed. The non-oxidative conversion of methane can play an attractive role in upgrading methane to higher hydrocarbon from an industrial perspective. ZSM-5 zeolite-supported Mo catalysts have been extensive studies to overcome the coke problem in the non-oxidative conversion of CH_4 (NOCM).[17–19] Although supported metal catalysts are essential for a wide range of chemical conversion technologies, the detailed mechanism of the heterogeneous reactions is not clear yet, and the properties of active sites formed at the interface of a metal and their underlying oxide support still unclear in front of the researcher. The local structure information is necessary to understand the catalytic activity, the reaction mechanism and develop a better efficient catalyst. X-ray absorption fine structure (XAFS) spectroscopy is a powerful method for atomic-level characterization, providing us local structure information.[20–28] In this research, we applied the XAFS method to determine the efficient catalyst for the non-oxidative coupling of methane (NOCM) reactions. Also, I used two theoretical methods: FEFF and full potential multiple scattering (FPMS) that can provide us theoretical XAFS data, which is used to determine the local structure of the analyzing sample by theoretical approaches.

1.2   Methane Conversion

Methane is the principal component of natural gas currently used for energy in the earth, home, and industrial heating system. It has an enormous heat of combustion relative to the form of CO_2. Methane and carbon dioxide both are well-known greenhouse gases, although methane's global warming potential (GWP) is approximately 25 times higher than that of carbon dioxide.[29] Large amounts of methane are reserved in nature in the form of natural gas, while a large amount of the greenhouse CO_2 gas put into the atmosphere comes from natural gas burning. The effective use of natural gas is considered the lowest emissions of greenhouse gas to prevent the rise in earth's temperature, which is known as global warming. As crude oil reserve depletion and widely fluctuating oil prices, natural gas is considered a source of clean fossil energy and a feedstock for chemicals. However, large amounts of natural gas are located in depopulated areas, where the transportation of methane in pipelines over a long

distance is not economically viable. Therefore the conversion of methane to other chemicals or liquid fuels such as olefins, aromatics, and hydrogen, which are more easily transportable products, is an acceptable way to exploit natural gas.[30,31] Methane, in general, is very stable because C-H bonds are strong (425 kJ/mol), and it contains no functional group. That's why it is very challenging to activated the methane C-H bond in the gas phase usually requires a high temperature. Methane can be converted to valuable chemicals by two major routes directly and indirectly (Figure 1-1).[32–35] The indirect method involves the intermediate production syngas ($CO+H_2$) mainly from steam reforming or partial oxidation followed by the Fischer-Tropsch (FT) process that converts the syngas to higher hydrocarbon.[36,37] These processes need a large amount of energy and cost because of the intermediate step. A large amount of the capital cost is associated with the production of methane to syngas. The increased demand for effective use of methane has motivated direct conversion without going through intermediate syngas.[14,34]
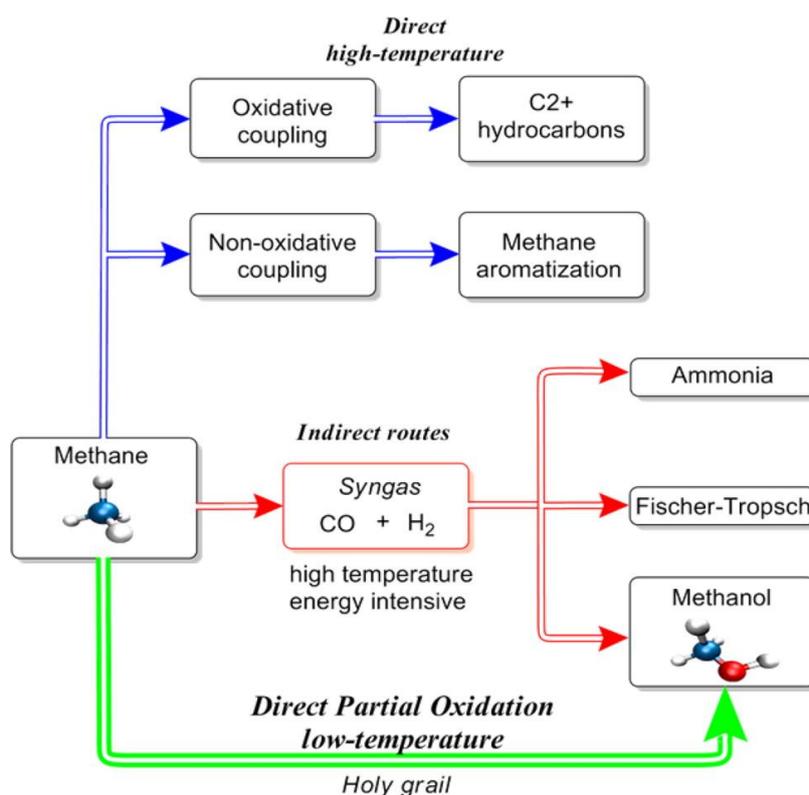
Figure 1-1. Overview of the different routes for the valorization of methane.[32]

1.2.1. Indirect Methods for Methane Utilization

In the indirect route, methane can be converted to fuel and liquid chemicals by multiple steps, via synthesis gas ($CO+H_2$) either by reforming or by partial oxidation. The products such as diesel fuel, gasoline, olefins, methanol, paraffin, dimethyl ether, and oxygenates can be obtained from synthesis gas using the well-established technology of Fischer-Tropsch synthesis (FTS).[38,39] The drawbacks of this process are that syngas production is energy and cost-consuming. Around 70-80% of the capital and almost all the energy consumed to operate the plant. The appropriate ratios of CO and H_2 production are achieved through the following process:

1. Steam reforming for syngas:

$$CH_4 + H_2O \xrightarrow[800-870°C]{Ni} CO + 3H_2 \quad (\Delta H^\circ_{298K} = 206 kj/mol)$$

2. Dry reforming for syngas:

$$CH_4 + CO_2 \xrightarrow[800-1000°C]{Ni/Pt} 2CO + 2H_2 \quad (\Delta H^\circ_{298K} = 247 kj/mol)$$
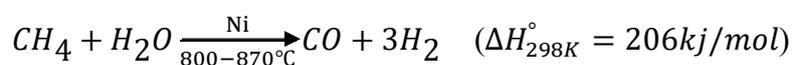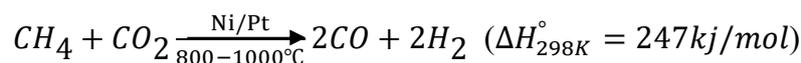
3. Partial oxidation for syngas:

$$CH_4 + \frac{1}{2}O_2 \xrightarrow[650-700°C]{Ni} CO + 3H_2 \quad (\Delta H^\circ_{298K} = -35 kj/mol)$$
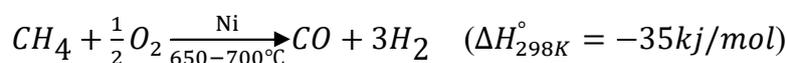
Finally, higher hydrocarbon and methanol have been synthesized from syngas using the Fischer-Tropsch process:

$$nCO + (2n+1)\ H_2 \xrightarrow[300\text{-}350\ ^0C]{Ru/Fe/Co} C_nH_{2n+2} + nH_2O$$
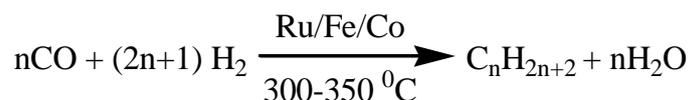
1.2.2. Direct Methods for Methane Utilization

In the indirect process, more than 60% cost of the plant is associated with the reforming of methane to synthesis gas. That's why a large intention has been paid for the direct conversion of methane without going through synthesis gas as an intermediate. Direct conversion of methane to valuable products without a complicated route is a beneficial way to utilize natural gas. The study of the direct conversion oxidation coupling of methane (OCM) was started in the early 1980s. The pioneering work of

Keller and Bhasin first reported the direct conversion of methane in 1982.[40] This experimental result initiated worldwide research to explore the high temperature (>1073) oxidative coupling of methane (OCM) to C2 hydrocarbon.[41,42] Despite the direct conversion of CH_4 is more economical and environmentally friendly, the conversion of methane is an associated problem both thermodynamically and kinetics. This high temperature is challenging because C-H bonds in methane are stronger than those in the resulting products (C-H bond strength in methanol 389 kj/mol). It means that achieving acceptable selectivity is, therefore, a challenge than reactivity. Several different approaches have been proposed to overcome this problem below as:

1. Thermal and catalytic pyrolysis of methane.

2. Oxidative coupling of methane.

3. Partial oxidation of methane to methanol and formaldehyde.

4. Different processes (plasma, halogenation, photocatalysis, membranes, etc.).

Catalyst can play an important role in most processes for methane conversion. From the 1990s to recent, hundreds of catalytic materials have been synthesized and examined.[10,42,43] Unfortunately, the presence of O_2 leads large amount of the thermodynamically stable products CO_2 and H_2O. For the commercial use of oxidation coupling of methane (OCM) to higher hydrocarbon cannot achieve acceptable selectivity.[44] Another remarkable problem is the deactivation of the catalyst during catalytic conversion of methane due to coke deposition.[15,16,45] Despite a large research effort on the direct conversion of methane during the last few years, no promising processes have been developed. At the present non-oxidative conversion of methane can play an attractive role in upgrading methane to higher hydrocarbon from an industrial perspective.

1.2.3. Non-oxidative Conversion of Methane

There is two way to achieve the non-oxidative conversion of methane to higher hydrocarbons commonly known as non-oxidative coupling of methane (NOCM) reactions. The first approach is produced primarily ethane and further hydrocarbons. The second approach is methane dehydroaromatization (MDA) to produce benzene. Both approaches are achievable at high temperatures with selective catalysts. The desired productions C_2H_6 and C_2H_4 from CH_4 can be represented as:

$$2CH_4 \rightarrow \ H_2 + \ C_2H_6; \quad \Delta H^0_{298} = +65 \ kJ$$

$$2CH_4 \rightarrow \ 2H_2 + \ C_2H_4 \ ; \quad \Delta H^0_{298} = +202 \ kJ$$
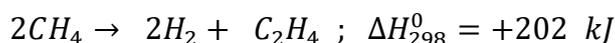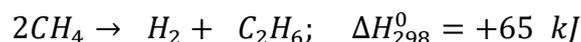
The non-oxidative conversion of methane retains H_2O as a reaction product because there is no involvement of oxygen or oxygen species. In some cases, NOCM is more attractive than OCM due to no oxidizing agent and the formation of H_2 with high selectivity and less coke formation during conversion reactions. To illustrate, ZSM-5 zeolite-supported Mo catalysts have been extensive studies to overcome the coke problem in the dehydrogenative conversion of CH_4 (DCM).[18,46,47] However, non-oxidative conversion of methane is now considering an important process to produce higher hydrocarbon from methane. But this reaction has a high-temperature barrier. Guo et al. reported a direct non-oxidative CH_4 conversion to ethylene, benzene, and naphthalene at > 1223 K on single-iron sites embedded in a silica matrix (Fe/Si$_2$O) with negligible coke formation. In this process, methane conversion reached a highest at 48.1% at 1363K, whereas the total selectivity of hydrocarbons was about 99%.[48]
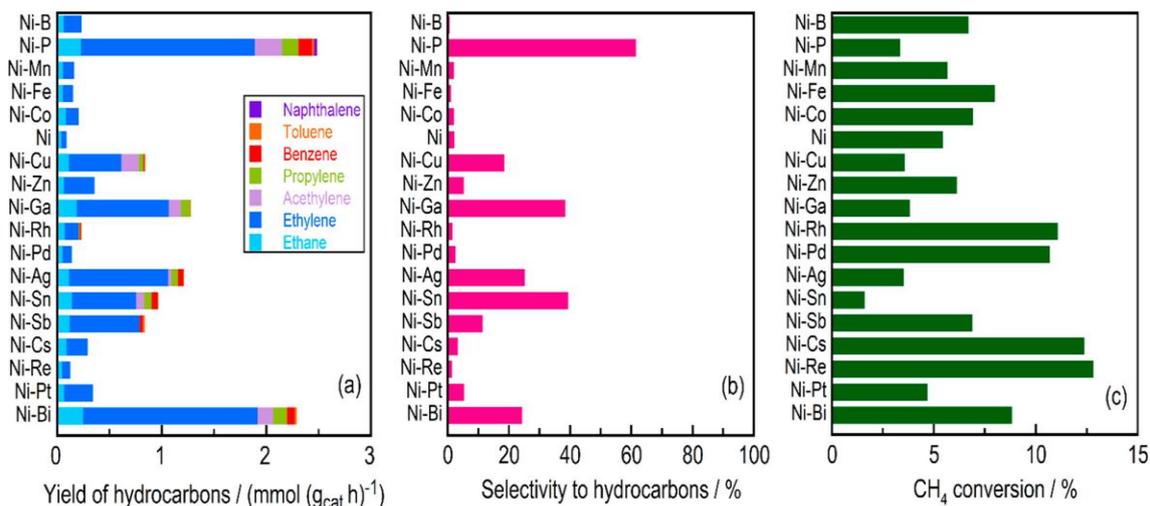
Figure 1-2. (a) The yield of hydrocarbons and (b) selectivity to hydrocarbons and (c) methane conversion in the NOCM reaction at 1173 K over Ni/SiO$_2$ and Ni-M/SiO$_2$ catalysts. [49]

Recently, Prof. Yamanaka and his research group tried to find out the efficient catalyst for methane convert to higher hydrocarbon. For Non-oxidative coupling of methane (NOCM) reactions, the catalytic activity of Ni/SiO$_2$ and various Ni-M/SiO$_2$

((M = B, P, Mn, Fe, Co, Cu, Zn, Ga, Rh, Pd, Ag, Sn, Sb, Cs, Re, Pt, and Bi) were analyzed at 1173K, using a conventional fixed-bed gas flow system as shown in Figure 1-2.[49] These results indicated that the Ni-P/SiO$_2$ catalyst efficiently promoted the methane activated than Ni/SiO$_2$. Here P atom is a key factor in controlling the catalytic activity.

1.3. Transition Metal Phosphide

Phosphorus reacts with most of the periodic elements to form a diverse class of compounds termed phosphides. The bonding range of the phosphide materials are ionic for the alkali and alkaline earth metals and metallic or covalent for the transition elements. More than one hundred binary transition metal phosphides with metal-rich M$_4$P to phosphorus-rich MP$_{15}$ are known.[50] The metal-rich compounds, MP or M$_2$P of the transition metal, which have metallic properties, are more active than the semiconducting phosphorus-rich compounds, MP$_2$, MP$_3$.[51]

Table 1-1. Unit cell and space group data of nickel phosphides.

Phosphide	Crystal system	Space group	Unit cell dimensions (Å)				Ref.
			a	b	c	z	
Ni$_3$P	Tetragonal	$I\bar{4}$	8.954	8.954	4.386	8	[57]
Ni$_{12}$P$_5$	Tetragonal	$I4/m$	8.646	8.646	5.070	2	[57]
Ni$_2$P	Hexagonal	$P\bar{6}2m$	5.859	5.859	3.382	3	[58]
Ni$_5$P$_4$	Hexagonal	$P63mc$	6.789	6.789	1.0989	4	[59]
NiP	Orthorhombic	$Pbca$	6.050	4.881	6.890	8	[57]
NiP$_2$	Monoclinic	$C12/c1$	6.366	5.615	6.072	4	[60]
NiP$_3$	Cubic	$Im\bar{3}$	7.816	7.816	7.816	8	[61]

Nickel phosphides have seven different forms, namely Ni$_3$P, Ni$_{12}$P$_5$, Ni$_2$P, Ni$_5$P$_4$, NiP, NiP$_2$, and NiP$_3$.[52,53] The differences in composition with various elements lead to a wide range of electronic, magnetic, optical, and catalytic properties. Metal-rich Ni$_3$P catalysts are known to exhibit high selectivity for the hydrogenation of dimethyl oxalate to

methyl glycolate.[54] The P-rich catalyst NiP_2 has been used as an active reversible Li-ion battery electrode.[55] $Ni_{12}P_5$ exhibits high conductivity and has been used in hybrid battery–superconductor devices.[56] Ni_2P has been used to catalyze hydro-treatment and hydrogen evolution reactions.

However, their catalytic properties depend on their microscopic properties, which govern by interatomic bonds and some active centers in the crystal. Their crystallographic structural information has been listed in Table 1-1. The detail of the crystal structure of nickel phosphides have been discussed below:

Ni_3P Crystal structure: The Ni_3P crystal structure has been shown in Figure 1-3. Ni_3P is the metal-rich phosphide that crystallizes in the tetragonal $I\bar{4}$ space group. There three inequivalent Ni sites: In the first Ni(0) site is bonded to four equivalent P3 atoms, which form NiP4 tetrahedral local structure. In the tetrahedral structure, the Ni-P
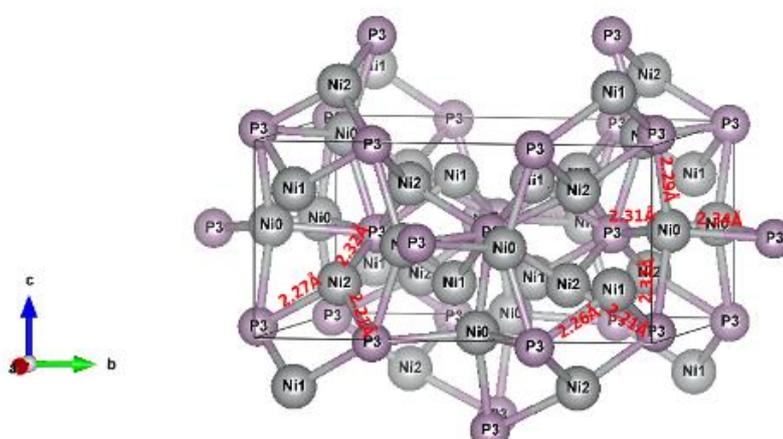
Figure 1-3. Ni_3P crystal structure

bond distances ranging from 2.29-2.34 Å. The Ni(1) site is bonded in a water-like geometry to two equivalent P3 atoms. Here, the shortest bond distance is 2.21 Å, where the other one is 2.26 Å. In the third Ni(2) site, Ni(2) location is bonded in a distorted non-coplanar geometry to three equivalent P3 atoms. Here, the Ni-P bond distances spreading from 2.21-2.32 Å.

$Ni_{12}P_5$ Crystal Structure: The $Ni_{12}P_5$ crystal structure has been shown in Figure 1-4. Metal-rich $Ni_{12}P_5$ crystal is the tetragonal $I4/m$ space group. It has two inequivalent Ni sites: The first Ni(0) site is bonded to four P atoms to form NiP4 tetrahedra local structure. Here the Ni-P bond distances ranging from 2.21-2.45 Å. In the second Ni(1)

site, the Ni(1) is formed see-saw like geometry with four P atoms. The two shortest Ni-P bond distances are 2.23 Å, where the two longest Ni-P bond distances are 2.58 Å.
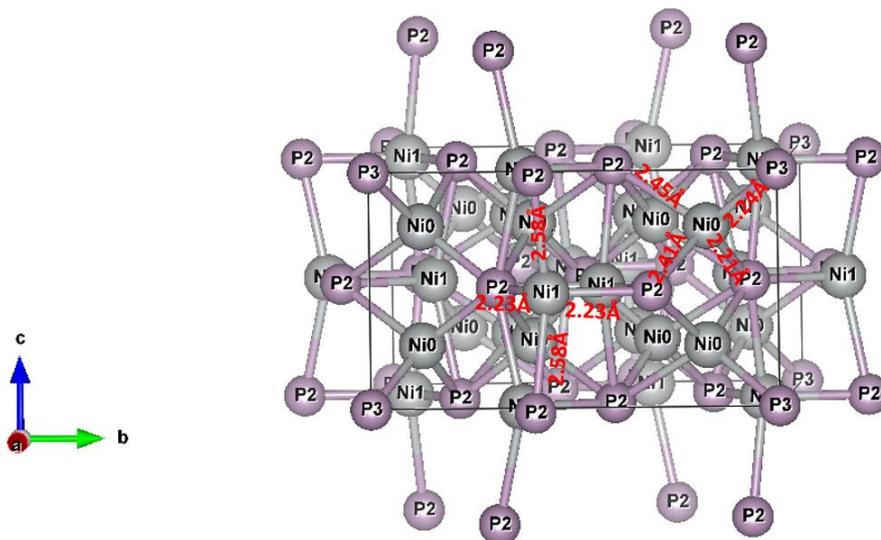
Figure 1-4. $Ni_{12}P_5$ crystal structure

Ni₂P Crystal Structure: The Ni_2P crystal structure has been shown in Figure 1-5. Ni_2P is hexagonal $P\bar{6}2m$ space group crystal. There are two inequivalent Ni sites: The first Ni(1) site is bonded with four P atoms to form NiP4 tetrahedra structure. In this local structure, two shorter 2.21 Å and two longer 2.27 Å Ni-P bonds are present. In the second Ni(2) site, Ni(2) is bonded to five P atoms to form distorted NiP5 trigonal bipyramidal. One Ni-P bond (2.34 Å) and four longer (2.46 Å) Ni-P bonds are present in the Ni_2P crystal.
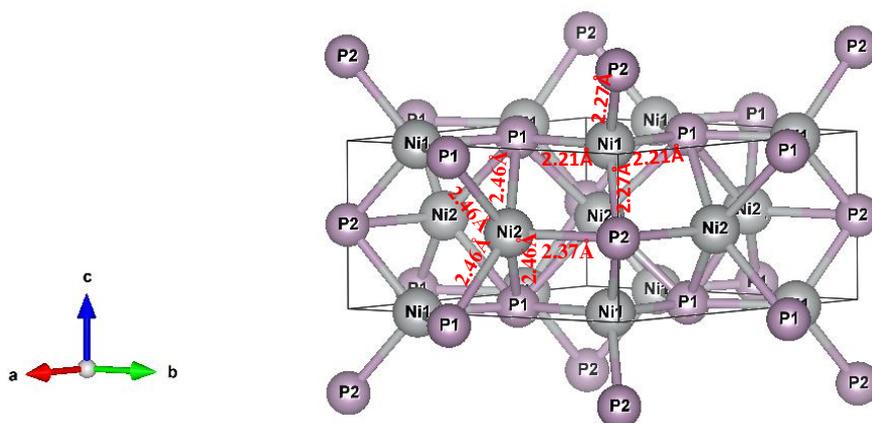
Figure 1-5. Ni_2P crystal structure

Ni₅P₄ Crystal Structure: The Ni$_5$P$_4$ crystal structure has been shown in Figure 1-6. Metal-rich Ni$_5$P$_4$ is the hexagonal *P63mc* space group crystal. There are four inequivalent Ni sites. In the first Ni(0) site, Ni(0) is bonded to five P atoms to form distorted NiP5 trigonal bipyramidal. The Ni-P bond distances are spreading from 2.27-2.46 Å. The second Ni(1) site is bonded with four P atoms to form a distorted tetrahedra local structure. There are three shorter 2.16 Å Ni-P bond distances and one longer 2.19 Å Ni-P bond distances present. The second Ni(1) site is bonded with four P atoms to form NiP4 trigonal pyramidal. In this structure, there are three shorter 2.16Å and one longer 2.19 Å Ni-P bond. The third Ni(3) site is bonded with four P atoms to form a distorted NiP4 tetrahedra structure; This structure has a spread of Ni-P bond distances ranging from 2.27-2.46 Å. In the fourth Ni(4) site is constructed distorted NiP5 trigonal bipyramid with five P atoms. The Ni-P bond distances are spreading range from 2.28-2.41 Å in this local structure.
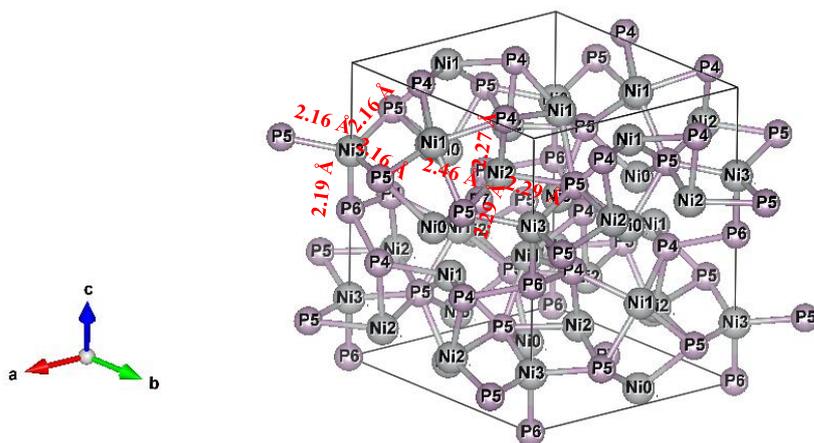
Figure 1-6. Ni$_5$P$_4$ crystal structure

NiP Crystal Structure: The NiP crystal structure has been shown in Figure 1-7. NiP is crystallized in the orthorhombic *Pbca* space group. This crystal has only Ni(0) site form 5-coordinate geometry to five equivalent P atoms. Here the Ni-P bond distances are spreading from 2.25-2.33 Å.
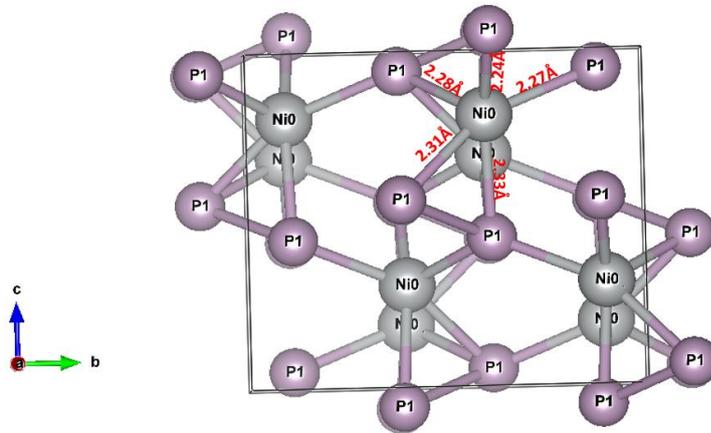
Figure 1-7. NiP crystal structure

NiP$_2$ Crystal Structure: The NiP$_2$ crystal structure has been shown in Figure 1-8. Phosphorus-rich NiP$_2$ is the monoclinic $C12/c1$ space group crystal. There is one Ni(1) site that is bonded four equivalent P atoms to form square co-planar geometry. All Ni-P bond distances are 2.21 Å.
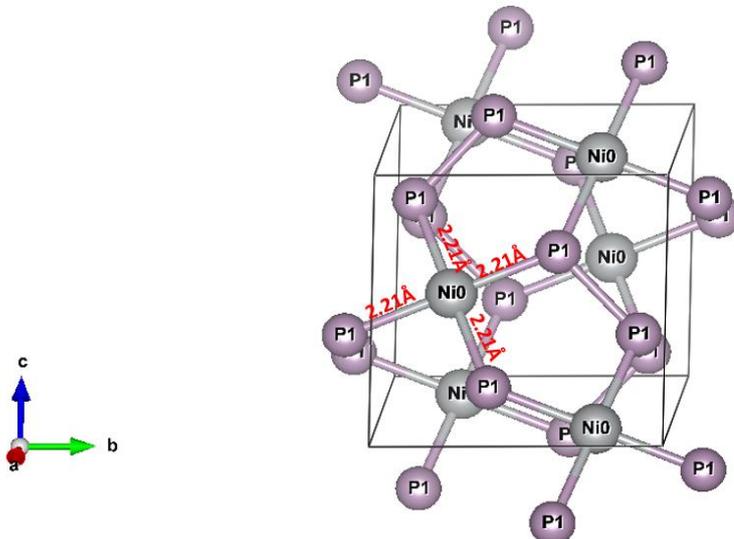
Figure 1-8. NiP$_2$ crystal structure

NiP₃ Crystal Structure: The NiP_3 crystal structure has been shown in Figure 1-9. Phosphorus-rich NiP_3 is crystallized in the cubic $Im\overline{3}$ space group. There is one local structure. The Ni (1) site is bonded to six equivalent atoms to form NiP6 octahedra structure. All Ni-P bond distances are 2.28 Å.
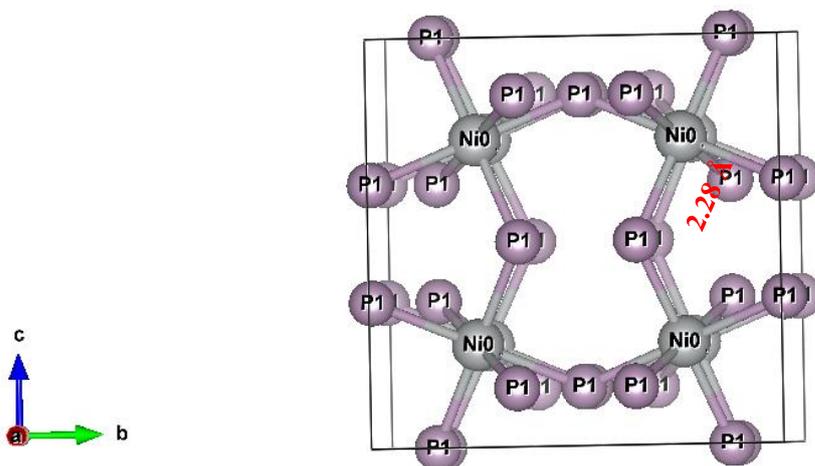
Figure 1-9. NiP_3 crystal structure

1.4. X-ray Absorption Fine Structure (XAFS)

The main goal of active catalytic materials is to determine the active sites and the local structure of the materials. X-ray absorption spectroscopy is the important method for catalyst characterization, an element-specific characterization technique that can reveal information about the local geometry of the central atom, such as bond distances coordination numbers and the oxidation states of the absorbing elements. Other surface characterization techniques like XRD, XPS, TEM, SEM, STEM, PEEM, etc. cannot provide that information.

X-ray is ionizing radiation with energies ranging from ~ 500 eV to 500 keV, or wavelengths from 25 Å to 0.25 Å, sufficient energy to eject a core electron from an atom. When an experimental sample is bombarded with the X-ray, some of the X-rays are absorbed by the atom in the sample. When the incident X-ray energy exceeds the binding energy, the core electron is ejected from the atom. Albert Einstein discovered this quantum mechanical phenomenon in 1905, known as the photoelectric effect. This absorption energy can be quantified by comparing the intensity of incident energy to the transmitted energy. This absorption is slightly changed for one incident X-ray energy. As the energy of the incident X-rays approaches, the core binding energy provides us

the threshold of the excitation, called the absorption edge, where the absorption intensity suddenly and strongly changes, as shown in Figure 1-10. The sharp rise is called an edge. It occurs because below the absorption edge, and the incident X-ray does not have enough energy to excite the electrons from some particular orbital, while the absorption edge they do it. This lead to an abrupt increase in absorption. When the X-ray photons excite an electron in the 1st orbital and leading to a sharp increase in the absorption known as K-edge. The L1–edge of X-ray absorption corresponds to the excitation from 2s orbital, M1-edge of X-ray absorption corresponds to the excitation from 3s orbital, and so on.
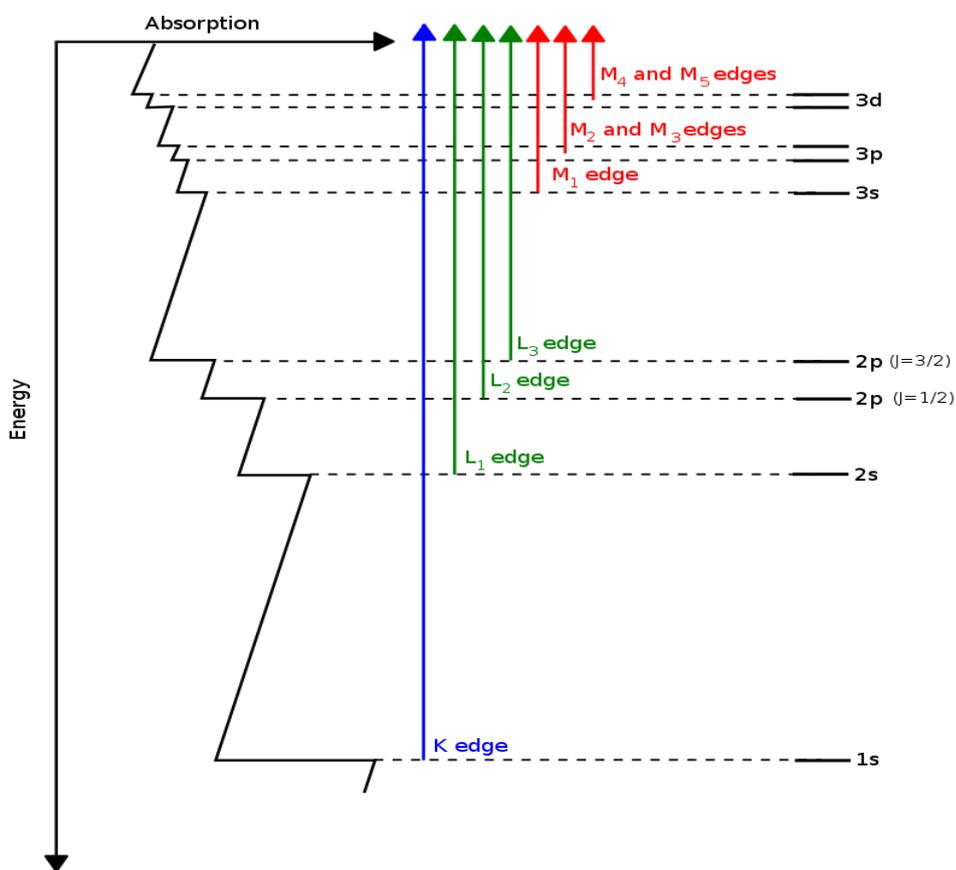
Figure 1-10. Diagram showing XAS edge transitions and the energy levels responsible for them.[62]

Figure 1-11 shows the K-edge of absorption of some 3d transition metals Cr to Zn, where the absorption edge clearly shifts with atomic number. This Figure clearly proves the elemental selectivity of X-ray absorption. Above the edges, the spectra clearly show some of the fine structure, which is the subject of this contribution. The absorption edge energy substantially differs about 100 eV in the different atomic number, but the absorption edge derivate only a few eV by changing environmental change around the absorption atom. This important feature provides us the elemental information. The local environmental changes affect the X-ray absorption spectral shape, called X-ray absorption fine structure (XAFS). XAFS analysis is the investigation of the dependence of the absorption intensity on incident X-ray energies which can directly be related to the local information around the absorbing atom.
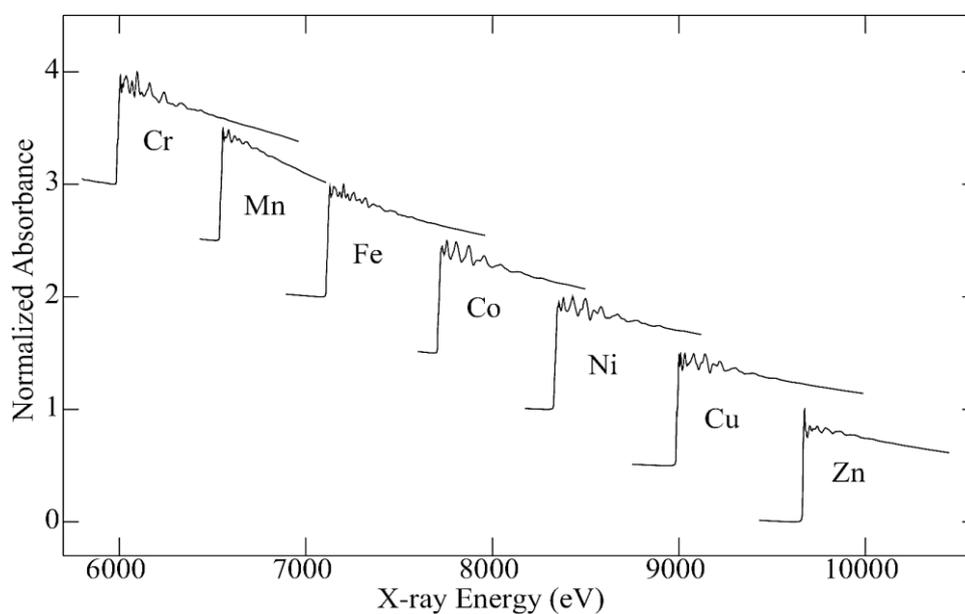
Figure 1-11.   X-ray K-edge absorption of some 3d transition-metal foils.[63]

X-ray absorption fine structure (XAFS) is the modulation of the X-ray absorption probability due to the chemical and physical state of atoms. XAFS are sensitive to the oxidation number, coordination number, distances, and the nature of the surrounding select atom. XAFS provides a simple way to determine the oxidation state and the local atomic structure for a selected atomic species. XAFS is widely used in scientific fields, including biology, environmental science, material science, and catalysts research. An atom-specific technique, XAFS, required specific energy to remove an electron from an

inner atomic orbital which depends on the binding energy between the electron and the nucleus. If the incident X-ray photon energy exceeds the binding energy of an electron in a material, the x-ray can be absorbed, and the electron can be excited from an inner orbital to a vacant excited state or to a continuum and released from its orbital. Then this electron called a photoelectron propagates as a wave and scatters off of nearby atoms. The waves can interfere with the backscattered wave. At the absorbing atom site, the interference may be constructive, enhancing the change that a given x-ray photon is absorbed and destructive, decreasing that change (Figure 1-12).
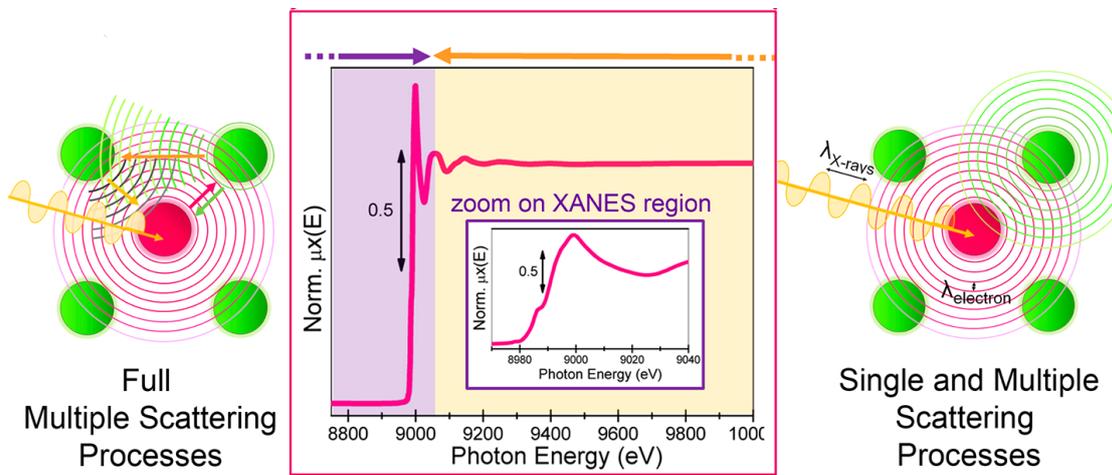
Figure 1-12. Diagram of Cu K-edge XAFS. The conventional division between XANES and EXAFS region and the schematic models of full multiple and single (and multiple) scattering processes, dominating the XANES and EXAFS region, respectively, are indicated.[64]

The kinetic energy of the photoelectron is equal to the incident photon energy E ($h\nu$) minus whatever energy necessary to remove the photoelectron from the absorbing atom is given by Equation (1.1); h is plank's constant, and ν is frequency.

$$T = h\nu - E_0 \tag{1.1}$$

The outgoing electron can be represented as a spherical wave as defined in Equation 1.2

$$\lambda = \frac{2\pi}{k} \tag{1.2}$$

15

$$where, k = \frac{1}{\hbar}\sqrt{2m_e(E - E_0)}$$

X-ray absorption spectroscopy (XAS) is the measurement of the absorption coefficient of a sample during the penetration of X-rays through a thin sample (Figure 1-13). The result is the intensity of the radiation I after passing through the sample is less than the incident radiation I_0. The absorption coefficient is determined by the decay of incident X-ray intensity I_0 with distance t. This can be related through the Beer-Lambert Law, the X-ray absorption coefficient μ is described using intensity I, which is transmitted through the sample Equation (1.3); where μ is the absorption coefficient, t is the thickness of the sample, I_0 and I are the initial and transmitted X-ray intensities.

$$I = I_0e^{-\mu t} \tag{1.3}$$
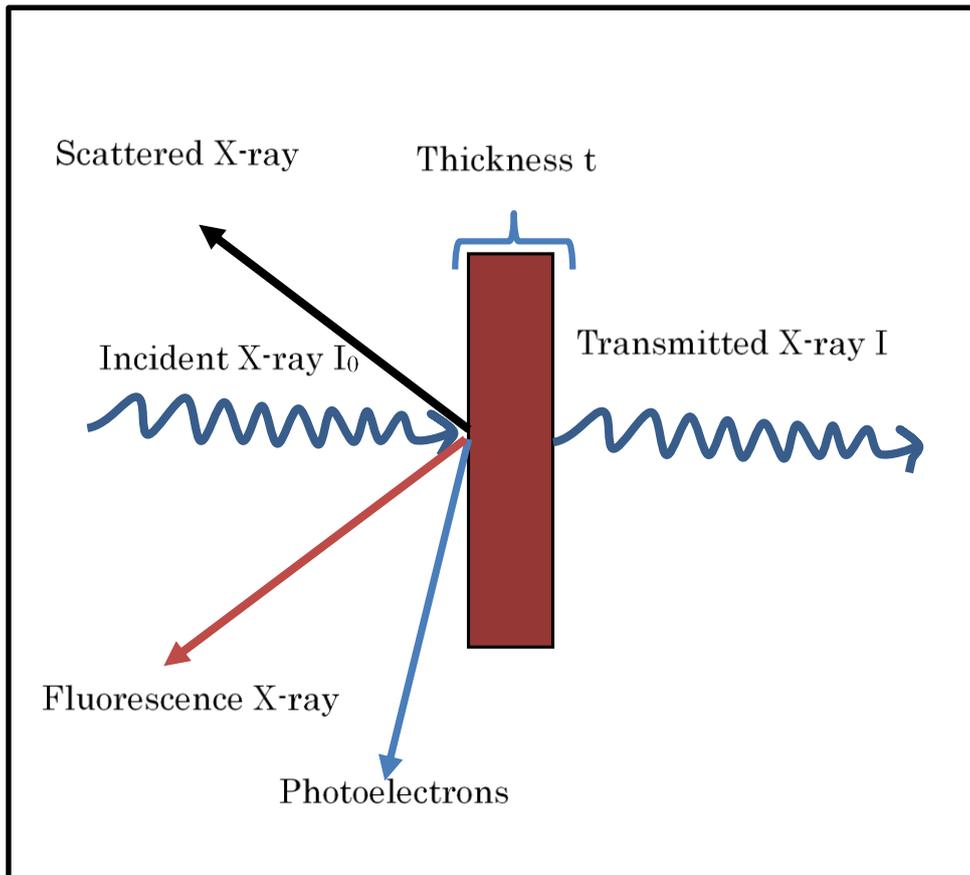
Figure 1-13. Diagram showing the transmission of an x-ray beam through a sample and the various effects this produces.

The Fermi Golden rule state that the absorption coefficient, $\mu(E)$, is proportional to the initial state to a final state for the transition in a system:

$$\mu(E) = \left|\langle \psi_i|H|\psi_f\rangle\right|^2 ; H = (\hat{\epsilon}.\bar{r})e^{\left(i(\hat{k}.\bar{r})\right)} \tag{1.4}$$

Where, ψ_i is the initial state function which describes a core level electron, X-ray photon, and no photoelectron; ψ_f is the final satte function which describes a photoelectron, core hole, and no X-ray; H is the interaction Hamiltonian between the electromagnetic field vector of the X-ray and the electron. The Hamiltonian expression includes the electric field vector of the X-ray $\in$, the forward scattering vector k, and the electron coordinate vector r.

Since the absorption depends on the incoming photon energy, an X-ray absorption spectrum is given by a plot of absorption versus photon energy, and the spectrum shows the sharp rise called absorption edges (Figure 1-12). Around the absorption edge, there is a fine oscillation structure called an X-ray absorption fine structure (XAFS). XAFS is classified into two energy regimes: X-ray absorption near edge structure (XANES) in the energy region up to about 50 eV of the absorption edge and extended X-ray absorption fine structure (EXAFS) in the higher energy region from 50-1000 eV beyond the absorption edge. XANES and EXAFS have been widely used in different fields in science like biology, material science, fundamental physics, which are carried out by measuring the x-ray absorption coefficient of a substance as a function of energy.[65]

There are some advantages and limitations of the XAFS method as follows:

Advantages

1) X-ray absorption fine structure (XAFS) is element-specific so that one can focus on aimed element information without interference from other elements present in the sample.

2) The sample is not necessary to obtain a single crystal of the material to extract the local structure of the element and not depend on the state of the sample because it is sensitive only to the local metal site structure.

3) XAFS can be applied to high temperature and high-pressure conditions so that in situ or operando measurements can be carried out.

Limitations

1) Hard X-rays can be damage samples during the XAFS experiments.

2) It is very sensitive around the X-ray absorbing atom but challenging to obtain the information of far atoms.

3) It cannot distinguish the scattering atoms with little difference in atomic number like C, N, O or S, Cl.

1.4.1. X-ray Absorption Near Edge Structure (XANES)

X-ray absorption near-edge structure (XANES) spectroscopy technique is a well-established technique that focuses on the area of the XAFS spectra before and immediately after the edge (Figure 1.12). Multiple scattering is predominant in the XANES region. XANES region is sensitive to the chemistry of the materials that can provide us the oxidation state and local structure geometry of the absorbing atom.[66,67]
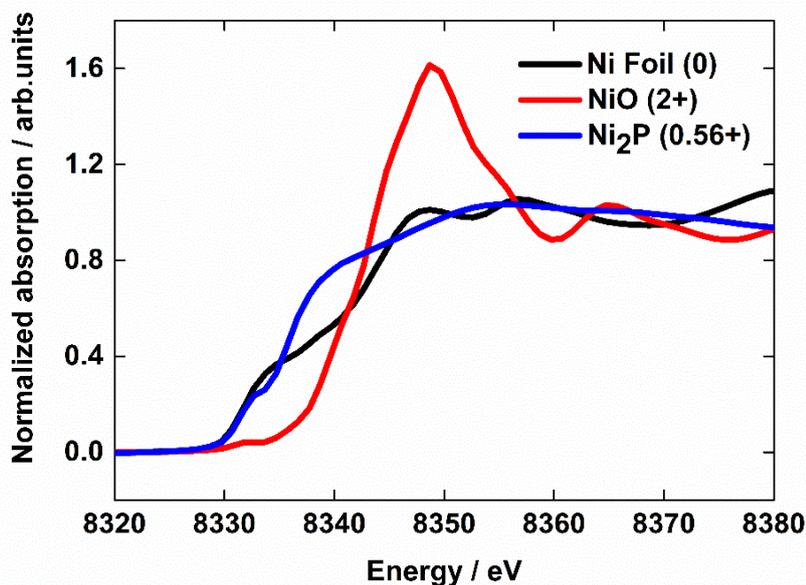
Figure 1-14.   XANES spectra of Ni K-edge with different oxidation states.

In XANES, an incident photon is absorbed by the core electron and excited from a core state to an empty state. At certain energy, a sharp rise in the absorption is observed, called an absorption edge. In the XANES experiment, the change in the absorption of X-rays due to the photoelectric effect is measured. The position of the absorption edge depends on the chemistry of the sample. In general, the absorption edge position shifts to higher energy with an increasing oxidation state, as shown in Figure 1-14.

So, it can be an indicator of the oxidation state of the absorbing atom. XANES spectra also are affected by the structural symmetry around X-ray absorbing atoms. The weak pre-edge feature in the XANES region is observed causes by forbidden quadrupole electronic transition, e.g., a 1s to 3d transition in a K-edge spectrum. The intensity of the pre-edge peak feature is proportional to the transition probability to 3d state. As a result of mixing 3d and 4p orbital, the pre-edge peaks appear in XANES spectra affected by the quadrupole transition, indicating that the absorbing atom geometry site distorts from a centrosymmetric geometry (Figure 1-15). Another important feature of the XANES is the white line intensity. Some XAS spectra a sharp feature at the top of the absorption edge. This feature is called the white line. In such a way, XANES strongly reflects the electronic configuration and symmetry of the central atom. It can provide a detailed picture of the local electronic structure of the element sample.
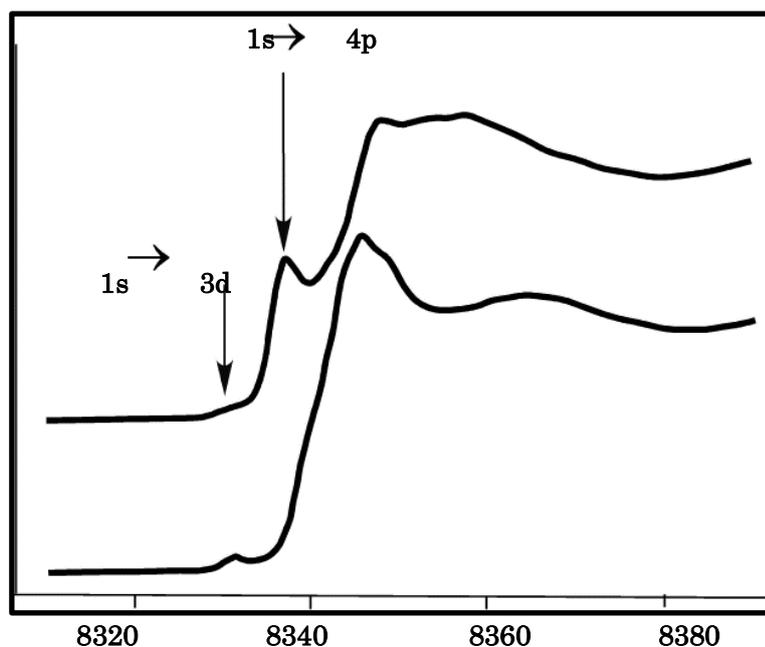
Figure 1-15. XANES spectra for 4-coordinate Ni^{II}. Top Ni(cyclam) $(ClO_4)_2$ (square planer); bottom $(Me_4N)_2NiCl_4$ (tetrahedral).[68]

1.4.2. Extended X-ray Absorption Fine Structure (EXAFS)

Extended X-ray absorption fine structure (EXAFS) appears in the oscillatory spectrum 50-1000 eV above the absorption edge.[69,70] For the first time, Fricke experimentally observed the fine structure beyond the absorption edges of selected atoms on K-edge[71] and Hertz on L-edge in 1920.[72] The effect of the physical and chemical state of the sample have on the fine structure of the XAS spectra was observed by Hanawalt in 1931.[73] After that many years were needed to exploit the potentiality of EXAFS for extracting quantitative information. The first theoretical attempt to explain the fine structure in the XAS was proposed by Kronig on the presence of long-range order in the system in the years 1931-32. [74,75] But it was unable to explain the EXAFS signals observed in gases, liquids, solutions, and amorphous solids. After a long time, XAFS was only just a spectroscopic curiosity and not yet a powerful characterization technique that was unable to provide quantitative information on the local structure of the absorbing atom in the observed materials. It was not until the groundbreaking theory by Sayers, Stern, and Lytle that the Fourier transforms (FT) of the background-subtracted oscillations provide R space which closes to the radial distribution of atomic density.[76] After that, many progressive works have been done with brilliant and broadband synchrotron X-ray radiation sources, established that EXAFS and XANES spectroscopies are reliable tools to understand the structure and the electronic configuration of unknown systems.

A common definition of the EXAFS function $\chi(E)$ is extracted from the X-ray absorption coefficient by subtracting the atomic background normalized the edge jump, as:

$$\chi(E) = \frac{\mu(E) - \mu_0(E)}{\Delta\mu_0(E)} \tag{1.5}$$

Where, $\mu(E)$ is the measured absorption coefficient, $\mu_0(E)$ is a smooth background function representing the absorption of the X-ray by an isolated atom, $\Delta\mu_0(E)$ is the measured edge jump.

The EXAFS oscillation was quantitatively parametrized by Sayers et al. in 1971 by the following equation:

$$\chi(k) = S_0^2 \sum_{i=1}^{n} \frac{N_i F_i(k)}{k r_i^2} \exp(-2k^2 \sigma_i^2) \sin(2k r_i + \varphi_i(k)) \tag{1.6}$$

Here, N_i = the coordination number of absorbing atom

$F_i(k)$ = backscattering amplitude

S_0^2= inelastic loss factor

$\varphi_i(k)$= phase shift of final state

r_i= interatomic bond distance

σ_i^2= Debye-Waller factor is the term for static disorder and thermal effect

E_0= Binding energy of the photoelectron

k= photoelectron wave number

For example, the experimental raw data of Ni_2P converted to k is shown in Figure 1-16. After conversion to k, the data are now ready for analysis. The transformation needed to decompose into constitute sine waves is known as Fourier transformation. A Fourier transform (FT) of the EXAFS function generates a radial distribution function for the absorbing atoms [77]; the resulting spectrum can look like Figure 1-16 (left side). This can be used to extract information about the nearest neighbor coordination shell of the atom and the local structure of the X-ray absorbing atom.[78]
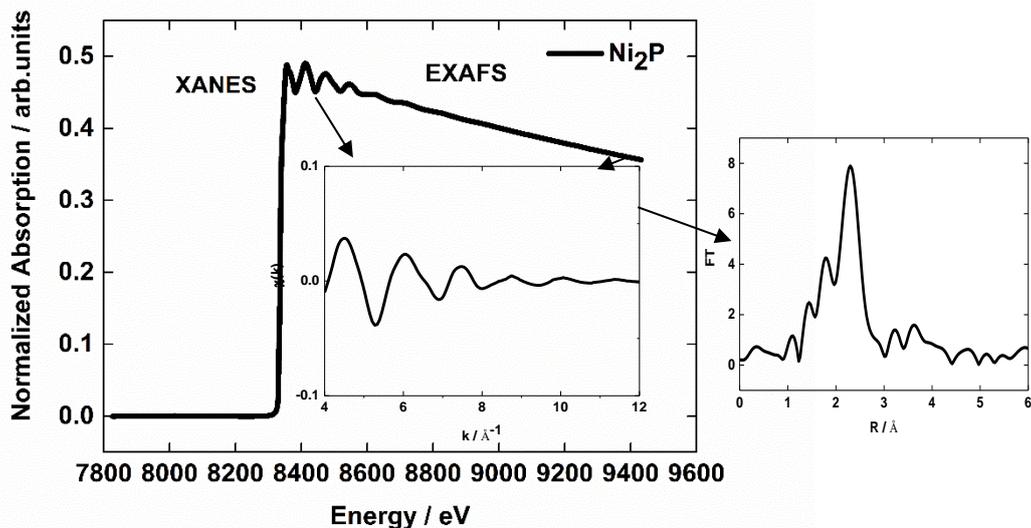
Figure 1-16. Ni k-edge EXAFS data reduction. Fourier transform of the k-space EXAFS data is shown on the right.

The EXAFS gives us the main information below as:

1) Bond distances between X-ray absorbing atom and neighboring atom

2) Coordination number of the central atom

3) The nature of the neighboring atom

Since EXAFS is the short-range order technique, element-specific, and provides us the local structure, it is considered the most suitable tool for investigating the local structure of an unknown sample. In this case, I applied the EXAFS technique to determine the active phase of silica-supported nickel phosphide catalysts for non-oxidative coupling of methane (NOCM) reactions. We usually use the Curve Fitting (CF) method for the EXAFS data analysis discussed below.

1.4.2.1. Curve Fitting (CF) Method

A typical complex structure might have different nearest-neighbor distances. Although each distance has a small signal contribution to the overall EXAFS, it is not realistic to extract all the different absorber-scatter interactions. Typically, a similar scatter at approximately the same distance from the absorber is group into a "Shell".
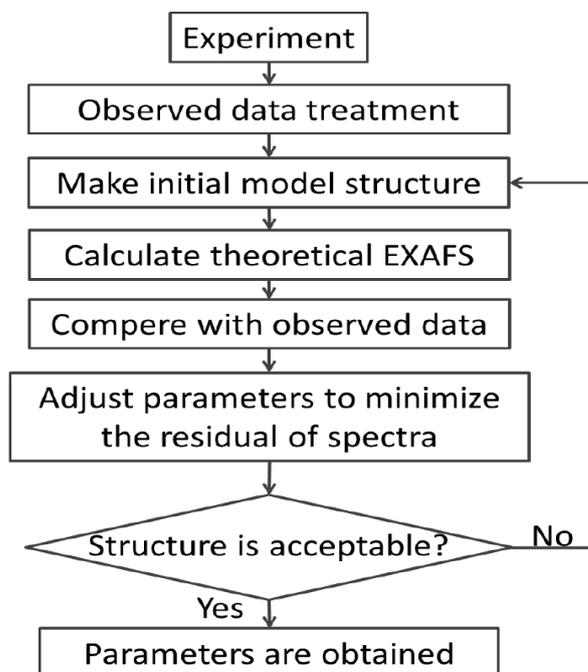
Figure 1-17. The flow chart of curve fitting (CF) analysis.

A non-linear least-square fitting algorithm is used to model the experimental EXAFS data using Equation 1.6.[79,80] This method is known as the Curve Fitting (CF) method. The flow chart of the CF method is shown in Figure 1-17.

The observed data are fitted with model structure using the EXAFS equation 1.6, where fitting parameters are coordination number (N), bond lengths (R), edge shift (dE), and Debye-Waller factor (σ^2). For curve fitting, backscattering factor F(k) and phase shift ϕ(k) is calculated using ab initio theoretical calculated program FEFF. Extracting parameters from the EXAFS spectrum of a reference sample involves performing a Fourier Transform and isolating a single peak, deriving backscattering factor F(k) and phase shift ϕ(k) from the calculated χ(k); analyzing an unknown sample according to normal analysis procedures. But the frequent problem is to determine all structural parameters whether the inclusion of an additional shell. Since data are available only over a finite k space and there is always some noise at the high k range. Usually, the number of independent points and the number of parameters that we can use in the fitting is defined by the following Equation:

$$N_{ind} = \frac{2\Delta k.\Delta R}{\pi} + \alpha \qquad (1.7)$$

Here, Δk and ΔR are the Fourier and inverse Fourier transform range of the observed data. Stern et al. suggested that the α value might be +1 or +2.[81]

Usually, the number of parameters is limited in the fitting. The number of extracted parameters on CF analysis must not exceed this degree of freedom. If we analyze the data from k = 3.0-10.0 Å^{-1} and R = 1.0-3.0 Å, then we will have 9 to 11 independent points calculate from Equation (1.7). If four parameters R, σ^2, and N and dE are refined per shell; then, you can only fit the spectrum up to 2 shells. The number of degrees of freedom increases linearly with the R range; therefore, if data can be detected to a high R range, it should be possible to obtained sufficient data to permit a detailed description of the structure. It sounds like a lot, but it is difficult to refine parameters if you analyze the complicated system. In the complex system composed of many atoms surrounded by the absorbing atom, you might find more than 2 shells in the fitting. But the number of searching parameters on CF analysis must not exceed this degree of freedom to obtain reliable results. For example, $Ni_{12}P_5$ complex system which has different Ni and P site and different Ni-P and Ni-Ni bond distances. Specifically, $Ni_{12}P_5$ has 5 Ni-P bonds demands 20 parameters to analyze each bond separately. But in this case, the degree of freedom is around 16 even though the k-range is 3-20 Å^{-1}. Therefore,

the limitation of the degree of freedom becomes a problem for the complex system.

In CF analysis, we also need to consider the R-factor. The residual of EXAFS oscillation between the experimental and calculated data one is minimized in the CF method. The degree of the fitting is evaluated by R-factor as shown in Equation (1.8).

$$R - factor = \sum_{i=1}^{N} \frac{\{\chi_{data} - \chi_{calculated}\}^2}{(\chi_{data})^2} \qquad (1.8)$$

Here χ_{data} and $\chi_{calculated}$ is EXAFS oscillation of experimental and calculated data. If the R-factor is small, then the fitted model is very similar to the experimental data.

1.5. XAFS Data Modeling

We can theoretically calculate the scattering amplitude and phase shift. To extract quantitative information from the experimental EXAFS data, we need to have an accurate value for the scattering amplitude and phase shift. These functions are actually calculated using one of a few computer programs FEFF, GNXAS, and EXCURVE. Here the FEFF program was used for the calculations.[82] The calculated factors are not restricted only to the first shell and can account for multiple scattering. The results of the FEFF calculation are stored in simple files that can be used directly in the analysis program. Currently, the software program REX2000 comes with the freely FEFF for calculating the theoretical EXAFS model.[83]

The general approach for the determination of structural information around the absorbing atom from EXAFS data is to generate a theoretical model for the sample, and the theoretical model calculation is done by FEFF for the EXAFS spectra. We can adjust the structural parameters R, N, σ^2 and also allow dE in the EXAFS equation until a least-square fit is obtained between the theoretical and experimental EXAFS spectra. The model is adjusted as needed until the best possible fit is observed in the theoretical and experimental spectra. The parameters that are often determined from a fit of EXAFS spectra which affected by the amplitude of the EXAFS spectra (N, S_0^2, σ^2) or the phase shift of the oscillations (ΔE_0 and ΔR). The best fit in R-space is shown in Figure 1-18. This typical fit of the Ni foil give us a Ni-Ni bond distance of R = 2.48 Å, the coordination number of N = 9.45, a mean square disorder of σ^2 = 0.0042 Å^2 and a shift in dE = -3.83 eV
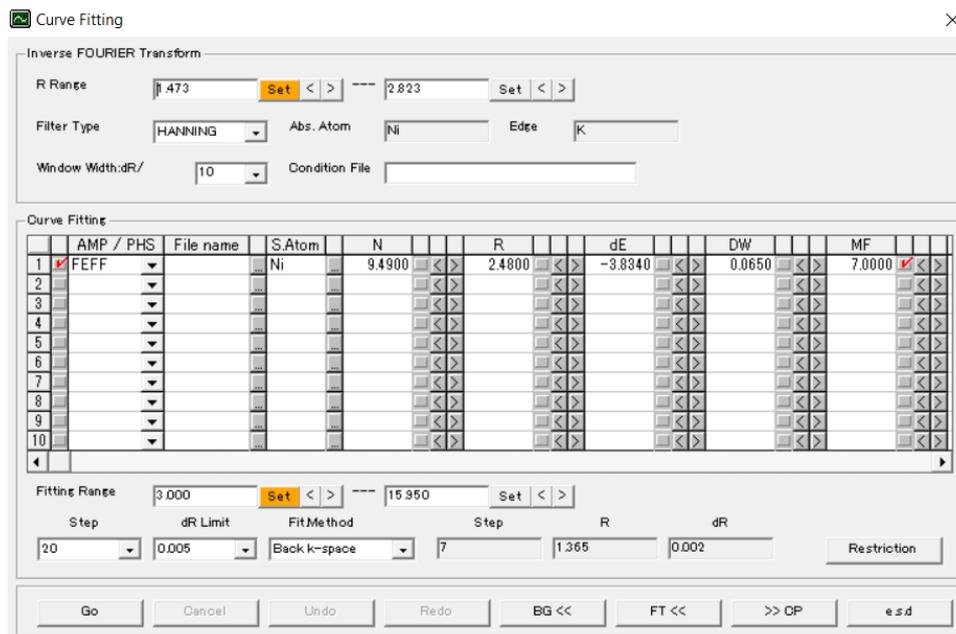
Figure 1-18. Screen capture from REX2000. The curve fitting analysis of Ni foil using REX2000.

XANES analysis is comparatively more complicated than EXAFS analysis. The interpretation of XANES is problematic because there is not a simple analytical or even physical description of XANES. Precise and accurate calculations of all spectral features are not always reliable and still difficult to calculate. Quantitative analysis of XANES spectra using ab initio calculations is not available. There is much chemical (qualitative) information obtained from the XANES spectra, notably oxidation state and coordination environment (Figure 1.14 and 1.15). This Figure clearly shows the edge position, and the shape of XANES spectra is sensitive to oxidation state, coordination environment, and molecular geometry. That's why XANES can be considered as a fingerprint to identify the phases. Although much progress has been made in the theoretical modeling of XANES, most of the applications of the XANES energy region remain qualitative analysis. But the recent development in multiple scattering formulas has shown that XANES spectra can provide element-specific information on bonding environment, such as coordination number and interatomic distances.

1.6. Problem of XAFS Analysis on the Ni-P/SiO₂ for NOCM Reaction

The main objective of this thesis is to reveal the active structure and make the relation between reaction activity and structure of nickel phosphide catalysts for non-oxidative coupling of methane (NOCM) reaction. To achieve this goal, I investigated the structure of Ni-P/SiO₂ catalysts with different initial Ni:P ratios of 1:1, 2:1, and 3:1 by XAFS. XAFS is the most suitable technique to investigate the local structure of the unknown sample. It provides us qualitative information (valence state and coordination geometry) and quantitative information (bond distance R, coordination number N) around the X-ray absorbing atom from XANES and EXAFS analysis, respectively. However, there are several drawbacks in EXAFS and XANES analysis. I analyze the EXAFS data using the conventional curve fitting method to achieve the catalytically active structure of SiO₂-supported nickel phosphide among the three samples which have been found highly active for non-oxidative coupling of methane (NOCM) reaction. I observed that Ni_2P/SiO_2 shows the high activity for NOCM reaction, which is demonstrated in chapter 3. But the conventional analysis of EXAFS by curve fitting (CF) method has the limitation of parameters by Nyquist theory. This limitation cannot allow me to analyze the data because of the complex nickel phosphide system, which contains many scattering atoms. Even if I reduce the number of fitting parameters, the obtained data were not directly related to a real structure. Due to the lack of references and limitation of parameters, I cannot confirm the structure of the other two structures with Ni and P ratios of 2:1 and 3:1.

On the other hand, XANES gives the electronic state and geometrical symmetry around the X-ray absorbing atom in the complex system straightforwardly. XANES studies require pattern fitting by comparing the reference and unknown as a fingerprint. But the lack of a reference sample hindered our XANES analysis. The recent development of XANES calculation like FEFF enables us to provide the theoretical reference which is demonstrated in Chapter 4. Another brand new method has been used for the theoretical XANES calculations called FPMS (full potential multiple scattering), which is demonstrated in Chapter 5.

1.7 Purpose and Construction of this Thesis

In order to elucidate the structure of nickel phosphide catalysts with three different compositions 1:1, 2:1, and 3:1, without experimental reference compounds, I developed theoretical model analysis methods for both XANES and EXAFS and try to show the

new possibilities to analyze the complex system without experimental reference compounds by XANES and EXAFS.

The thesis is composed of 6 chapters to describe the new way of XAFS analysis for the complex structure. In Chapter 1, I discuss the background of my research and an introductory discussion of the XAFS method. In Chapter 2, I introduce the experimental setup for conventional XAFS measurement and a fundamental discussion of experimental and theoretical data analysis. In Chapter 3, I analyze the experimental EXAFS data by conventional curve fitting (CF) method to find out the active phase of SiO_2-supported nickel phosphide for NOCM reaction. The structure of Ni-P/Si_2O (Ni:P = 1:1) is confirmed by the EXAFS analysis, where the other two samples, Ni-P/Si_2O (Ni:P = 2:1) and Ni-P/Si_2O (Ni:P = 3:1) structure is still unknown, discuss in this chapter. In Chapter 4, I discuss the structure of unknown sample Ni-P/SiO_2 with different Ni:P ratios of 1:1, 2;1, and 3:1 using a theoretical model. The theoretical XANES and EXAFS data reproduction has been demonstrated in this chapter. This approach is different from the conventional XAFS data analyses. Finally, I confirm the structure of SiO_2-supported Ni-P catalysts and discuss the structure-catalytic relations. In Chapter 5, I discuss the new FPMS method for XANES analysis. FPMS is a still-developing and challenging method. The FPMS calculated XANES spectra are compared with the FEFF spectra. Also, the advantages, difficulties, and future directions of the FPMS method will be discussed here. In Chapter 6, I discuss the general conclusion of this thesis and the future directions for this research.

Reference

1.   Ranade, V. V., & Joshi, S. S. (2016). Catalysis and Catalytic Processes. In *Industrial Catalytic Processes for Fine and Specialty Chemicals* (pp. 1-14). (Elsevier Inc., 2016).

2.   Brown, T. L., LeMay, H. E., Bursten, B. E. & Brunauer, L. S. Chemistry: The Central Science. **8**, 1–4 (1994).

3.   Chang, R. & Overby, J. *Chemistry*. 13 ed., (McGraw-Hill Education, 2019).

4.   Zumdahl, S. S. & DeCoste, D. J. *Introductory chemistry : a foundation*. (Cengage learning, 2019).

5.   Rasmussen, S. B.; Bañares, M. A.; Bazin, P.; Due-Hansen, J.;Ávila, P.; Daturi, M., *Phys. Chem. Chem. Phys.* **14**, 2171–2177 (2012).

6.   Hagen, J. *Industrial Catalysis: A Practical Approach: Second Edition*. *Industrial Catalysis: A Practical Approach: Second Edition* (Wiley, 2006).

7.   Marcilly, C. Present status and future trends in catalysis for refining and petrochemicals. in *Journal of Catalysis* vol. 216 47–62 (Academic Press Inc., 2003).

8.   Solymosi, F., Erdöhelyi, A. & Szöke, A. Dehydrogenation of methane on supported molybdenum oxides. Formation of benzene from methane. *Catal. Letters* **32**, 43–53 (1995).

9.   Zhu, Q. *et al.* Sulfur as a selective 'soft' oxidant for catalytic methane conversion probed by experiment and theory. *Nat. Chem.* **5**, 104–109 (2013).

10.   Weckhuysen, B. M., Rosynek, M. P. & Lunsford, J. H. Characterization of surface carbon formed during the conversion of methane to benzene over Mo/H-ZSM-5 catalysts. *Catal. Letters* **52**, 31–36 (1998).

11.   Qiu, P., Lunsford, J. H. & Rosynek, M. P. Characterization of Ga/ZSM-5 for the catalytic aromatization of dilute ethylene streams. *Catal. Letters* **52**, 37–42 (1998).

12.   Ruitenbeek, M. & Weckhuysen, B. M. A Radical Twist to the Versatile Behavior of Iron in Selective Methane Activation. *Angew. Chemie Int. Ed.* **53**, 11137–11139 (2014).

13.   Otsuka, K. Direct Conversion of Methane to Higher Hydrocarbons. *J. Japan Pet. Inst.* **30**, 385–396 (1987).

14.   Holmen, A. Direct conversion of methane to fuels and chemicals. *Catal. Today* **142**, 2–8 (2009).

15.   Karakaya, C. & Kee, R. J. Progress in the direct catalytic conversion of methane

to fuels and chemicals. *Progress in Energy and Combustion Science* vol. 55 60–97 (2016).

16. Ma, S., Guo, X., Zhao, L., Scott, S. & Bao, X. *Recent progress in methane dehydroaromatization: From laboratory curiosities to promising technology. Journal of Energy Chemistry* vol. 22 (2013).

17. Wang, L. *et al.* Dehydrogenation and aromatization of methane under non-oxidizing conditions. *Catal. Letters* **21**, 35–41 (1993).

18. Morejudo, S. H. *et al.* Direct conversion of methane to aromatics in a catalytic co-ionic membrane reactor. *Science.* **353**, 563–566 (2016).

19. Yang, S. Study on coke formation over Mo/HZSM-5 catalyst in non-oxidative methane dehydroaromatization reaction, Doctoral dissertation (2015).

20. Chen, Y. *et al.* Metal Phosphides Derived from Hydrotalcite Precursors toward the Selective Hydrogenation of Phenylacetylene. *ACS Catal.* **5**, 5756–5765 (2015).

21. Fujita, S. *et al.* Unique Catalysis of Nickel Phosphide Nanoparticles to Promote the Selective Transformation of Biofuranic Aldehydes into Diketones in Water. *ACS Catal.* **10**, 4261–4267 (2020).

22. Oyama, S. T. *et al.* In situ FTIR and XANES studies of thiophene hydrodesulfurization on Ni 2P/MCM-41. *J. Catal.* **268**, 209–222 (2009).

23. Cho, K. S. & Lee, Y. K. XAFS studies on highly dispersed Ni2P/SiO2 catalysts for hydrodesulfurization of 4,6-dimethyldibenzothiophene. *Nucl. Instruments Methods Phys. Res. Sect. A Accel. Spectrometers, Detect. Assoc. Equip.* **621**, 690–694 (2010).

24. Zhao, H., Oyama, S. T., Freund, H. J., Włodarczyk, R. & Sierka, M. Nature of active sites in Ni2P hydrotreating catalysts as probed by iron substitution. *Appl. Catal. B Environ.* **164**, 204–216 (2015).

25. Kawai, T. *et al.* EXAFS measurements of a working catalyst in the liquid phase: An in situ study of a Ni2P hydrodesulfurization catalyst. *J. Catal.* **241**, 20–24 (2006).

26. Frenkel, A. I. *et al.* Combining X-ray absorption and X-ray diffraction techniques for in situ studies of chemical transformations in heterogeneous catalysis: Advantages and limitations. *J. Phys. Chem. C* **115**, 17884–17890 (2011).

27. Kawai, T. *et al.* In situ EXAFS studies on Ni2P hydrodesulfurization catalysts in the presence of high pressure and high temperature oil. *AIP Conf. Proc.* **882**, 616–618 (2007).

28. Oyama, S. T. & Lee, Y. K. The active site of nickel phosphide catalysts for the

hydrodesulfurization of 4,6-DMDBT. *J. Catal.* **258**, 393–400 (2008).

29. Yuliati, L. & Yoshida, H. Photocatalytic conversion of methane. *Chem. Soc. Rev.* **37**, 1592–1602 (2008).

30. Rival, O., Grandjean, B. P. A., Guy, C., Sayari, A. & Larachi, F. Oxygen-free methane aromatization in a catalytic membrane reactor. *Ind. Eng. Chem. Res.* **40**, 2212–2219 (2001).

31. Aboul-Gheit, A. K., Awadallah, A. E., El-Kossy, S. M. & Mahmoud, A. L. H. Effect of Pd or Ir on the catalytic performance of Mo/H-ZSM-5 during the non-oxidative conversion of natural gas to petrochemicals. *J. Nat. Gas Chem.* **17**, 337–343 (2008).

32. Olivos-Suarez, A. I. *et al.* Strategies for the Direct Catalytic Valorization of Methane Using Heterogeneous Catalysis: Challenges and Opportunities. *ACS Catal.* **6**, 2965–2981 (2016).

33. Choudhary, T. V., Aksoylu, E. & Goodman, D. W. Nonoxidative activation of methane. *Catalysis Reviews - Science and Engineering* **45**, 151–203 (2003).

34. Lunsford, J. H. *Catalytic conversion of methane to more useful chemicals and fuels: a challenge for the 21st century. Catalysis Today* vol. 63 (2000).

35. Hu, Y. H. & Ruckenstein, E. Catalytic Conversion of Methane to Synthesis Gas by Partial Oxidation and CO2 Reforming. *Advances in Catalysis* vol. 48 297–345 (2004).

36. Torres Galvis, H. M. *et al.* Iron particle size effects for direct production of lower olefins from synthesis gas. *J. Am. Chem. Soc.* **134**, 16207–16215 (2012).

37. Wu, Y., Feng, J. & Li, W. Development of Integrated High Temperature and Low Temperature Fischer-Tropsch System for High Value Chemicals Coproduction. in *Energy Procedia* vol. 142 1259–1266 (Elsevier Ltd, 2017).

38. Fazlollahi, F. *et al.* Preparation of Fe-Mn/K/Al2O3 fischer-tropsch catalyst and its catalytic kinetics for the hydrogenation of carbon monoxide. *Chinese J. Chem. Eng.* **21**, 507–519 (2013).

39. Dry, M. E. *The Fischer-Tropsch process: 1950-2000. Catalysis Today* vol. 71 (2002).

40. Keller, G. E. & Bhasin, M. M. Synthesis of ethylene via oxidative coupling of methane. I. Determination of active catalysts. *J. Catal.* **73**, 9–19 (1982).

41. Lunsford, J. H. The Catalytic Oxidative Coupling of Methane. *Angewandte Chemie International Edition in English* vol. 34 970–980 (1995).

42. Arakawa, H. *et al.* Catalysis research of relevance to carbon management: Progress, challenges, and opportunities. *Chemical Reviews* vol. 101 953–996

(2001).

43.   Solymosi, F., Szske, A. & Cser6nyi, J. *Conversion of methane to benzene over Mo2C and Mo2C/ZSM-5 catalysts. Catalysis Letters* vol. 39 (1996).

44.   Ruitenbeek, M. & Weckhuysen, B. M. A Radical Twist to the Versatile Behavior of Iron in Selective Methane Activation. *Angew. Chemie - Int. Ed.* **53**, 11137–11139 (2014).

45.   Ma, D. *et al.* Carbonaceous deposition on Mo/HMCM-22 catalysts for methane aromatization: A TP technique investigation. *J. Catal.* **208**, 260–269 (2002).

46.   Budde, P. K., Singh, A. K. & Upadhyayula, S. Non-oxidative methane dehydroaromatization reaction over highly active α - MoC 1 - x ZSM-5 derived from pretreatment. *J. Chem. Sci.* **130**, (2018).

47.   Wang, L. *et al.* Dehydrogenation and aromatization of methane under non-oxidizing conditions. *Catal. Letters* **21**, 35–41 (1993).

48.   Guo, X. *et al.* Direct, non-oxidative conversion of methane to ethylene, aromatics, and hydrogen. *Science (80-.).* **344**, 616–619 (2014).

49.   Dipu, A. L. *et al.* Direct non-oxidative conversion of methane to higher hydrocarbons over silica-supported nickel phosphide catalyst. *ACS Catal.* **10**, 375–379 (2020).

50.   Hulliger, F. *Crystal chemistry of the chalcogenides and pnictides of the transition elements. Structure and Bonding* (Springer Berlin Heidelberg, 1968).

51.   Oyama, S. T. Novel catalysts for advanced hydroprocessing: Transition metal phosphides. in *Journal of Catalysis* vol. 216 343–352 (2003).

52.   Massalski, T. B., Okamoto, H. & International., A. S. M. Binary Alloy Phase Diagrams. in *Alloy Phase Diagrams* 89–89 (ASM International, 1990). doi:10.31399/asm.hb.v03.a0006247.

53.   Ren, J., Wang, J. guo, LI, J. fen & LI, Y. wang. Density functional theory study on crystal nickel phosphides. *Ranliao Huaxue Xuebao/Journal Fuel Chem. Technol.* **35**, 458–464 (2007).

54.   Zhu, J. *et al.* Nanoporous Ni 3 P Evolutionarily Structured onto a Ni Foam for Highly Selective Hydrogenation of Dimethyl Oxalate to Methyl Glycolate. *ACS Appl. Mater. Interfaces* **11**, 37635–37643 (2019)..

55.   Gillot, F. *et al.* Electrochemical reactivity and design of NiP2 negative electrodes for secondary Li-Ion batteries. *Chem. Mater.* **17**, 6327–6337 (2005).

56.   Gan, Y. *et al.* High conductivity Ni12P5 nanowires as high-rate electrode material for battery-supercapacitor hybrid devices. *Chem. Eng. J.* **392**, (2020).

57.   Larsson, E. An X-ray investigation of Ni-P system and crystal structures of NiP

and NiP2. *Ark. Kemi* **23**, 335 (1965).

58. Rundqvist, S. *et al.* X-Ray Investigations of Mn3P, Mn2P, and Ni2P. *Acta Chemica Scandinavica* vol. 16 992–998 (1962).

59. Elfström, M. Physical properties of lower nickel phosphides. *Acta Chem Scand* **19**, 1694 (1965).

60. Donohue, P. C., Bither, T. A. & Young, H. S. High-Pressure Synthesis of Pyrite-Type Nickel Diphosphide and Nickel Diarsenide. *Inorg. Chem.* **7**, 998–1001 (1968).

61. Rundqvist, S. & Larsson, E. The crystal structure of Ni12P5. *Acta Chem. Scand* **13**, 551–560 (1959).

62. XANES - Theory. (2020). https://chem.libretexts.org/@go/page/1869

63. Gordon E. Brown, J. & Stanford. Interfaces, Heavy Metals, Microbes, and Plants: Shedding New Light on Environmental Science at the Molecular Level. 1–132 (2005).

64. Bordiga, S., Groppo, E., Agostini, G., Van Bokhoven, J. A. & Lamberti, C. Reactivity of surface species in heterogeneous catalysts probed by in situ x-ray absorption techniques. *Chem. Rev.* **113**, 1736–1850 (2013).

65. Rehr, J. J. & Albers, R. C. Theoretical approaches to x-ray absorption fine structure. *Rev. Mod. Phys.* **72**, 621–654 (2000).

66. Ankudinov, A. & Ravel, B. Real-space multiple-scattering calculation and interpretation of x-ray-absorption near-edge structure. *Phys. Rev. B - Condens. Matter Mater. Phys.* **58**, 7565–7576 (1998).

67. Henderson, G. S., De Groot, F. M. F. & Moulton, B. J. A. X-ray absorption near-edge structure (XANES) spectroscopy. *Reviews in Mineralogy and Geochemistry* vol. 78 75–138 (2014).

68. Penner-Hahn, J. E. X-ray Absorption Spectroscopy. in *Encyclopedia of Life Sciences* 159–182 (John Wiley & Sons, Ltd, 2005).

69. Iwasawa, Y., Asakura, K. & Tada, M. *XAFS Techniques for Catalysts, Nanomaterials, and Surfaces. XAFS Techniques for Catalysts, Nanomaterials, and Surfaces* (Springer chem. 2017).

70. Rehr, J. J. & Albers, R. C. Theoretical approaches to x-ray absorption fine structure. *Rev. Mod. Phys.* **72**, 621–654 (2000).

71. Fricke, H. The K-characteristic absorption frequencies for the chemical elements magnesium to chromium. *Phys. Rev.* **16**, 202–215 (1920).

72. Hertz, G. über die Absorptionsgrenzen in der L-Serie. *Zeitschrift für Phys.* **3**, 19–25 (1920).

73. J. D. Hanawalt. The dependence of X-ray Absorption Spectra upon Chemical and Physical State. *Phys. Rev.* **37**, 715 (1931).

74. Kronig, R. de L. Zur Theorie der Feinstruktur in den Röntgenabsorptionsspektren. *Zeitschrift für Phys.* **70**, 317–323 (1931).

75. Kronig, R. de L. Zur Theorie der Feinstruktur in den Röntgenabsorptionsspektren. III. *Zeitschrift für Phys.* **75**, 468–475 (1932).

76. Stern E A, Sayers D E & Lytle F W. Extended x-ray-absorption fine-structure technique. III. Determination of physical parameters. *Phys. Rev. B* **11**, 4836–4846 (1975).

77. Sayers, D. E., Stern, E. A. & Lytle, F. W. New technique for investigating noncrystalline structures: Fourier analysis of the extended x-ray-absorption fine structure. *Phys. Rev. Lett.* **27**, 1204–1207 (1971).

78. Rehr, J. J., Kas, J. J., Vila, F. D., Prange, M. P. & Jorissen, K. Parameter-free calculations of X-ray spectra with FEFF9. *Phys. Chem. Chem. Phys.* **12**, 5503–5513 (2010).

79. Asakura, K. Analysis of EXAFS. in (ed. Iwasawa, Y.) vol. 58 33–58 (world scientific, 1996).

80. Teo, B. K., Antonio, M. R. & Averill, B. A. Molybdenum K-Edge Extended X-ray Absorption Fine Structure (EXAFS) Studies of Synthetic Mo-Fe-S Clusters Containing the MoS4 Unit: Development of a Fine Adjustment Technique Based on Models. *J. Am. Chem. Soc.* **105**, 3751–3762 (1983).

81. Stern, E. A. Number of relevant independent points in x-ray-absorption fine-structure spectra. *Phys. Rev. B* **48**, 9825–9827 (1993).

82. Zabinsky, S. I., Rehr, J. J., Ankudinov, A., Albers, R. C. & Eller, M. J. Multiple-scattering calculations of x-ray-absorption spectra. *Phys. Rev. B* **52**, 2995–3009 (1995).

83. Taguchi, T., Ozawa, T. & Yashiro, H. REX2000: Yet another XAFS analysis package. *Phys. Scr. T* **T115**, 205–206 (2005).

Chapter 2

Conventional Experimental and Analytical Method

2.1. Introduction

Various techniques have been used for the structural analysis: XRD, XRF, PEEM, STEM, XAFS, etc., and among them, the X-ray absorption fine structure (XAFS) spectroscopy technique is extensively used in structural analysis in short-range order because it is element-specific and does not require the long-range order. Over the last four decades, the XAFS technique has undergone tremendous progress due to the availability of synchrotron radiation, theoretical analysis development, and easy access to software packages, leading to a more accurate explanation of the surface structure of different classes materials. To elucidate the local structure of nickel phosphide catalysts with different Ni:P ratios for the non-oxidative coupling of methane (NOCM) reaction, I applied the conventional XAFS method and the theoretical XAFS method.

2.2. Conventional XAFS Measurement

Conventional XAFS measurement has been well established in the last few decades.[1,2] In this chapter, the general part of XAFS measurement has been described. In conventional XAFS measurement, data have been collected by transmission mode and fluorescence mode. The methodology of collecting data processing has also been well established. In this process, I only focus on the method of obtaining and analyzing the XAFS spectrum that I can extract structural information from the analyzing sample. Background removal and normalization are carried out to get EXAFS and XANES oscillation from experimental data. The XANES spectrum is directly compared with standard compounds, where the objective is to confirm the unknown structure of the analyzing sample. After the Fourier transformed (FT), the EXAFS spectrum is analyzed to directly obtain the local structure information. Due to the lack of reference compounds, I also carried out two theoretical models: a conventional FEFF and a brand new FPMS method to calculate the theoretical XANES spectra. The details of the theoretical approaches have been described in Chapter 4 and Chapter 5, respectively.

2.3. Equipment's of XAFS Measurement

For the conventional XAFS measurement, synchrotron radiation (SR) is mainly used as the X-ray source with others equipment: monochromator, focusing mirror, bending magnet, Insertion device (undulator), etc. An undulator comprises a complex array of small magnets, which force the electrons to follow an undulating or wavey trajectory. The SR emitted at each consecutive bend overlaps and interfered with that from other bends. The emitted X-ray is focused by a mirror, and selective energy is chosen by the monochromator. The schematic arrangement of XAFS measurement is shown in Figure 2-1.
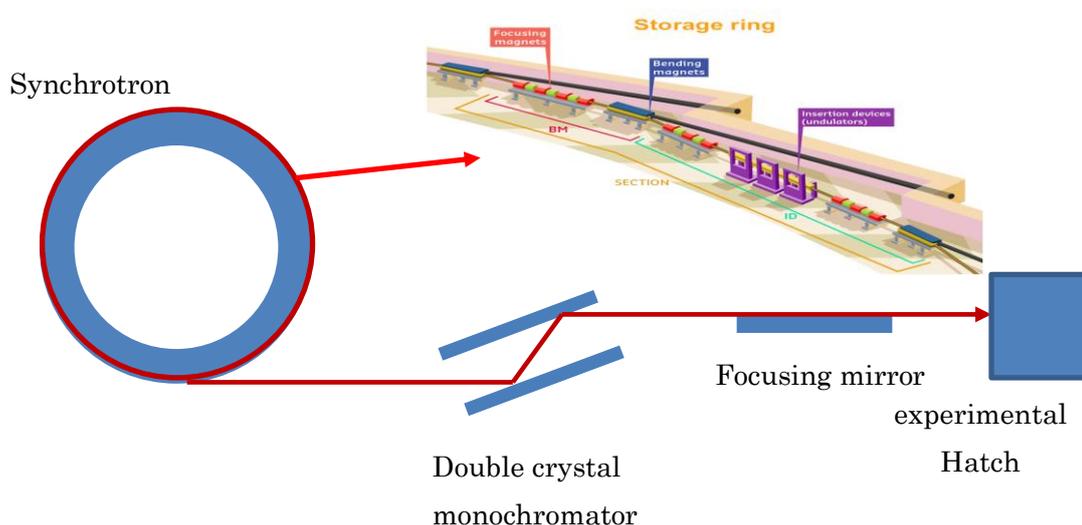
Figure 2-1.   Arrangement of the beamline for XAFS measurement.[3]

2.3.1. Synchrotron X-ray Sources

Synchrotron radiation (SR) is emitted from an electron when it travels at almost the speed of light, and a magnetic field bends its path. Synchrotron radiation was first observed in 1947.[4] In the case of synchrotron radiation, electrons are accelerated to near-light velocity and achieved high energy stored in the electron storage ring. Finally, an X-ray is generated when the electron is bent by a bending magnet.

The general features of synchrotron radiation are as following:

- High brightness and high intensity than X-rays produce in

conventional X-ray tubes.

- Highly directional X-ray.

- Linearly or circularly polarized X-ray.

- It is pulsed with controlled intervals.

- Temporally and spatially stable.

These important features of synchrotron radiation make the XAFS analysis more practicable. At first, synchrotron radiation was extracted from a storage ring by a bending magnet used in experimental analysis on metallic copper at the Stanford Synchrotron Radiation Facility.[5] At this moment, third-generation storage rings operate worldwide in the European Synchrotron Radiation Source (ESRS), France, Advanced Photon Source (APS), USA, and Spring-8, Japan.

2.3.2. XAFS Beamline: Photon Factory BL-9C

In this thesis, XAFS measurements were carried out at beamline BL9C of the photon factory, Institute of Materials Structure Science (IMSS), high Energy Accelerator Research Organization (KEK). The ring energy and current were 2.5 Gev and 450 mA, respectively. The major component area bent cylindrical mirror (Rh coated), Si (111) double crystal monochromator, two flat mirrors for higher-order reduction. The incident X-ray is monochromatized by Si (111) and focused by a bent cylinder mirror (Rh coated). The energy range is 4-23 keV, Ca K-edge to Rh K-edge.

2.3.3. Gas-Filled Detector

When the radiation passes through a gas, it produced electron-ion pair in the gas-filled detector. Both electron and ion move under the influence of the electrical field. Their motion induces a current on the electrodes or is transformed into a pulse. Based on their signal detection, the first one is known as the current or integrating chamber, and the second one is called the pulse chamber.

The charge collected depends on the applied high voltage. If the voltage applied to the detector is steadily increased, then the charge collected per unit time changes, as shown in Figure 2-2.
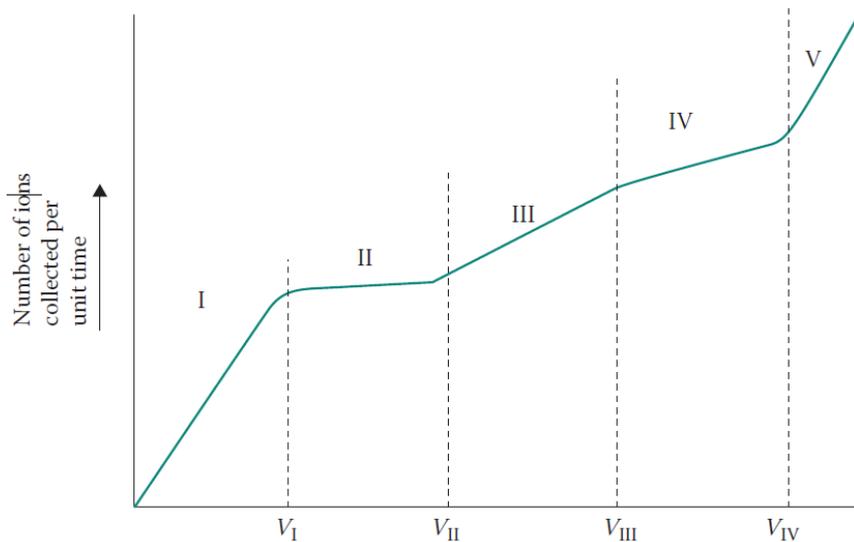
Figure 2-2. The relationship between the voltage applied to the detector and the charge collected.[6]

Depends on the applied voltage region, the gas-filled detector is known as ionization chambers, proportional counters, and GM counter. An ionization chamber is widely used to detect the incident X-ray I_0. In the transmission mode measurement, the intensity of transmitted X-ray, I, is measured using this chamber. In this research, an ionization chamber has been used to measure the incident X-ray intensity (I_0) and transmitted X-ray intensity (I).

The ionization chamber operates in region II. In this region, no charge multiplication and no new charge occur; that's why the charge collected stays constant despite a change in the voltage. If the high voltage is not supplied enough, then the charge collection linearity will be lost. Thus the high voltage supplied is necessary for the ionization chamber. Here the output signal is proportional to the particle energy dissipated in the detector. Such detectors detect only the strongly ionizing particle. We can measure the particle energy using this detector easily and be reliable.

2.3.4. Scintillation Detectors

In the fluorescence mode, the intensity of the X-ray is measured by the scintillation counter. Scintillators produce sparks or scintillations of light when ionizing radiation passes through them. In 1903, William Crookes first observed scintillations when alpha particles hit the ZnS screen. A counting system using a scintillator that produces light. The scintillation light intensity is very low. It must be amplified with a device known as the photomultiplier tube or phototube (Figure 2-3). A photomultiplier consists of a photocathode at the inlet and several dynodes in the interior. When a photon is produced in the scintillator, it hit the photocathode and emits electrons. This electron goes to dynode guided by the electric field and hits the dynodes. The secondary electron form when the electron impinges upon it. The secondary electrons from the first dynode move toward the second dynode and move toward the third, and so on. The magnitude of the light output is the most important property of the scintillator. The light output affects the number of photoelectrons generated at the input of the photomultiplier. The filter and solar slit are used between the sample and the scintillation counter because the scintillation counter cannot remove the background from the scattered X-ray in itself.
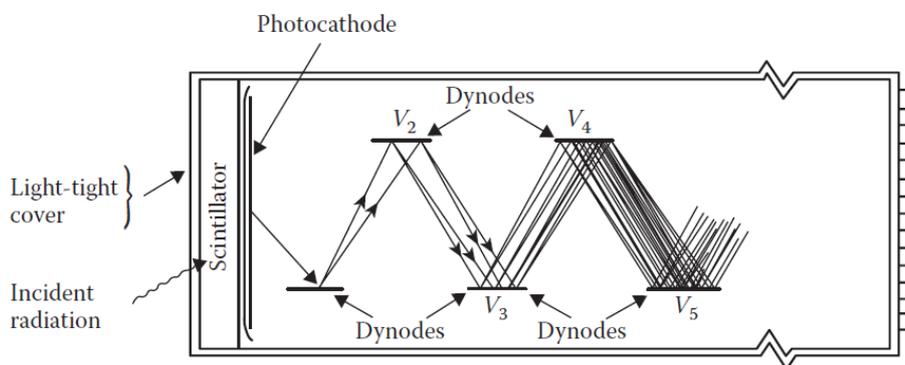
Figure 2-3. Schematic diagram of the interior of a photomultiplier tube.[6]

2.4. X-ray Absorption Measurement

Although different methods have been developed to measure the X-ray absorption spectra, two main experimental setups are usually used for the X-ray absorption data collection, transmission and fluorescence mode. Each mode has some advantages and disadvantages. Sometimes it is possible to measure data in both transmission and fluorescence mode simultaneously depends on the beamlines facilities, but it is not

available in all beamlines. The beamlines that have been set up depends on the concentration of the sample and the nature of the materials being studied.[7] A short summary of the XAFS spectra measurement setup has been described below.

2.4.1. Transmission Mode

The most straightforward mode is the transmission mode that has been used to study the structure of nickel phosphide catalysts. In this setup, the intensity of the incident X-ray (I_0) and transmitted X-ray (I) by a sample of thickness X is measured simultaneously. That's why two detectors have been used, one before and another after the sample, as shown in Figure 2-4.
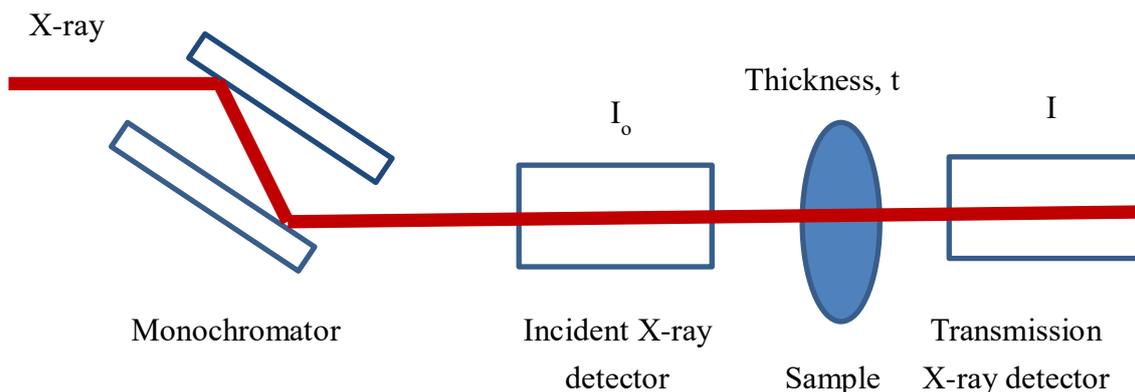
Figure 2-4. Diagram of typical XAS set up for transmission.

The X-ray comes from synchrotron radiation with large-scale energy so that the x-ray energy is needed to extract by the monochromator. The monochromator is composed of a single crystal, e.g., Si (111), which can diffract the certain energy of X-ray and then be focused by mirror toward the incident ion chamber. In the ion chamber, incident X-ray intensity (I_o) is measured before going through the sample. Then the X-ray goes through the sample, and the intensity of the X-ray (I) is measured in the ion chamber. The absorption coefficient μ is described by the Beer-Lambard law by Equation (2.1).

$$\mu t = ln \ \frac{I_0}{I} \qquad\qquad (2.1)$$

40

This transmission method is suitable for relatively high concentrated and very thickness studying samples. The measurement of the EXAFS and XANES spectra with minimizing the signal to noise ratio using this mode requires that the sample would be of constant thickness and does not have any holes.

2.4.2. Fluorescence Mode

Fluorescence mode is applied to collect the fluorescence photons and electrons where it is not possible to collect transmission mode. The set up of fluorescence mode is shown in Figure 2-5.
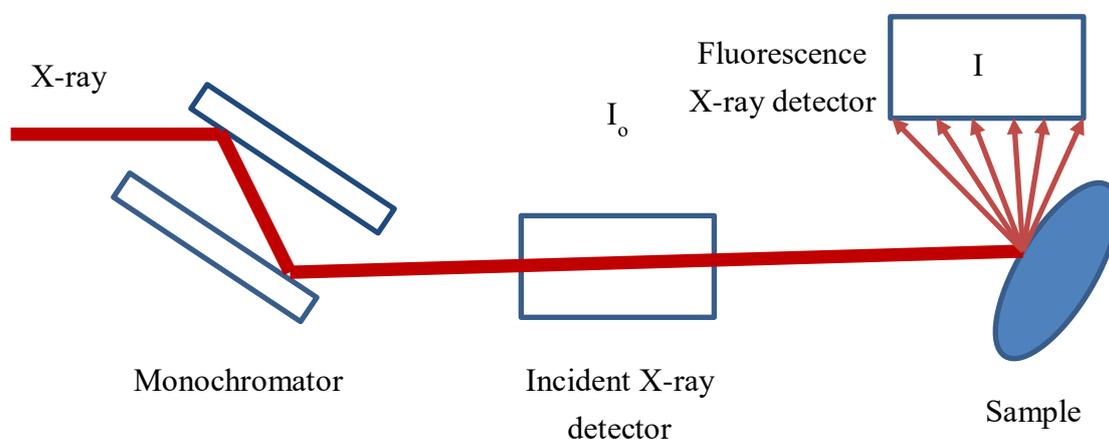
Figure 2-5. Diagram of typical XAS set up for fluorescence.

The arrangement of fluorescence mode is almost the same as transmission mode, where X-ray is transferred, monochromatized, and focused in the same way from synchrotron radiation. But in the fluorescence mode, the sample is placed at a 45^0 angle to the incident beam to ensure the minimum amount of fluorescence electrons are detected, and the fluorescence detector is positioned at 90^0 to the incident beam to minimize the scatter. The intensity of fluorescence X-ray (I_f) is measured in a fluorescence detector that comes from the sample. The absorption coefficient is an approximation in Equation (2.2).

$$\mu t = \frac{I_f}{I_0} \qquad (2.2)$$

A low or dilute concentration sample is used in fluorescence mode due to it having a

better signal-to-noise ratio than the corresponding transmission data.

2.5. Data Processing

For the data collection, at first, we need to set up a beamline for the desired absorption edge. The required X-ray energy is achieved by tuning the monochromator. The ion chamber I_0 and I are filled by 100% N_2 and (15% N_2 + 85% Ar) mixture of gases to ensure sufficient absorption. It is ideal for running either a standard material or a foil, e.g., for Ni K-edge running either NiO powder or Ni metal foil. This standard is used to determine the data quality and check the edge position to ensure the monochromator is calibrated properly. If we get good results from the standard sample, then everything is ready to start experiments.

In this thesis, I will focus on analyzing the EXAFS spectrum, as that how quantitative information can be obtained on the short-range order structure. At the same time, I will focus on analyzing the XANES spectrum by comparing the sample with standard compounds; the objective is to find the unknown phase of Ni-P/SiO$_2$ with different Ni:P ratios of 1:1, 2:1, and 3:1.

2.5.1. EXAFS Data Analysis

To obtain the structural parameters from the EXAFS spectrum, a procedure was established that consists of converting raw data into normalized EXAFS oscillations $\chi(k)$ and then extracting the structural parameters. There are several data processing steps to refine the final spectrum for analysis.[7–11] Before the analysis of experimental data, several steps have been carried out, as shown in Figure 2-6. The details of each process discuss as follows:
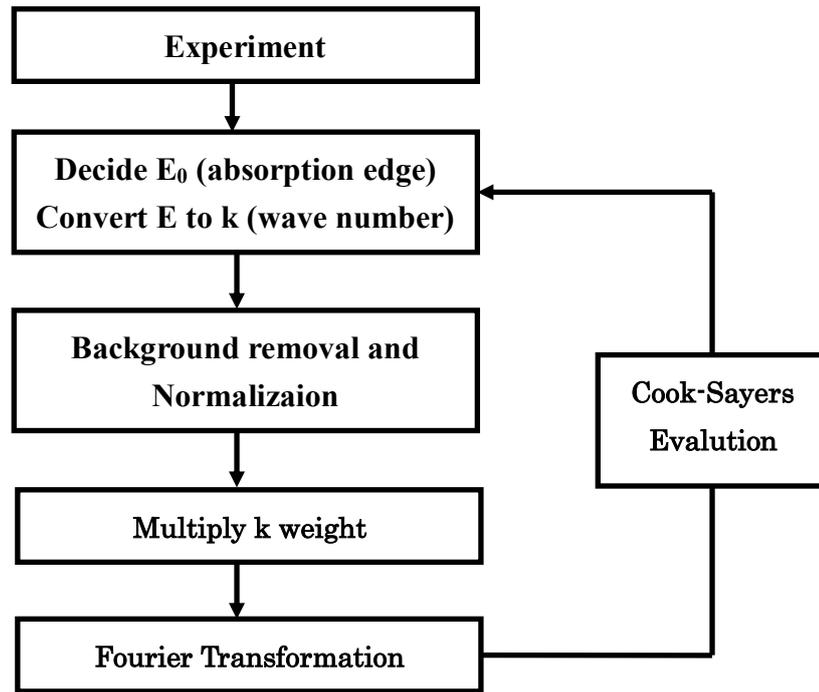
Figure 2-6. Flow diagram for analyzing the experimental EXAFS data using curve fitting method.

2.5.1.1. Convert Measured Intensities to μ(E)

The absorption coefficient is obtained as a function of the X-ray photon energy. We construct measured absorption coefficient, μ(E) for transmission mode by using the following Equation

$$I = I_0 e^{-\mu(E)t} \tag{2.3}$$

$$\mu(E)t = \ln\left(\frac{I_0}{I}\right) \tag{2.4}$$

Here, I_0 is incident X-ray energy intensity, I is the transmittance X-ray energy intensity, and t is the thickness of the sample.

2.5.1.2. Background Removal and Normalization

To obtain the χ(K) function from the atomic absorption, the first step is to remove the background, which is extrapolated to the region after the absorption edge. Background

removal was performed using the computer software package named REX2000.[12,13] The pre-edge region, $\mu(E)$ and post-edge region, $\mu_0(E)$ are decided like Figure 2.7 for normalizing the spectrum.
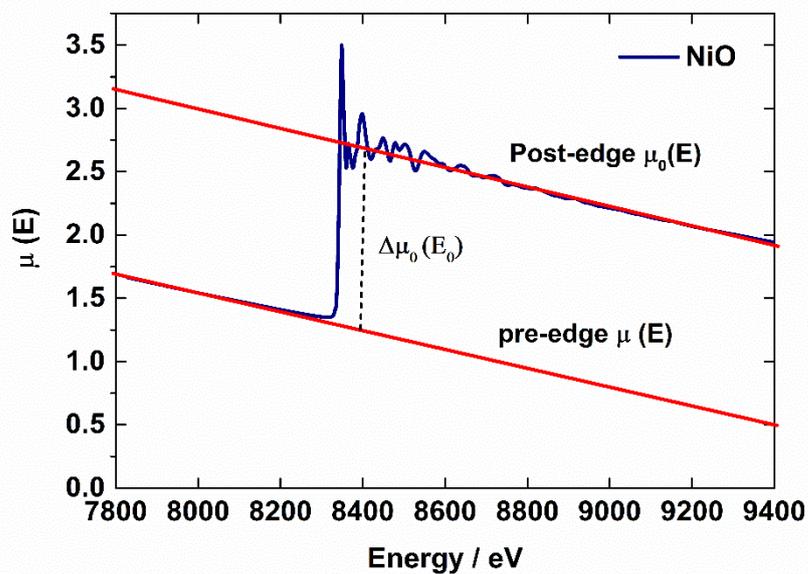
Figure 2-7. EXAFS spectrum and extraploted line for background removal.
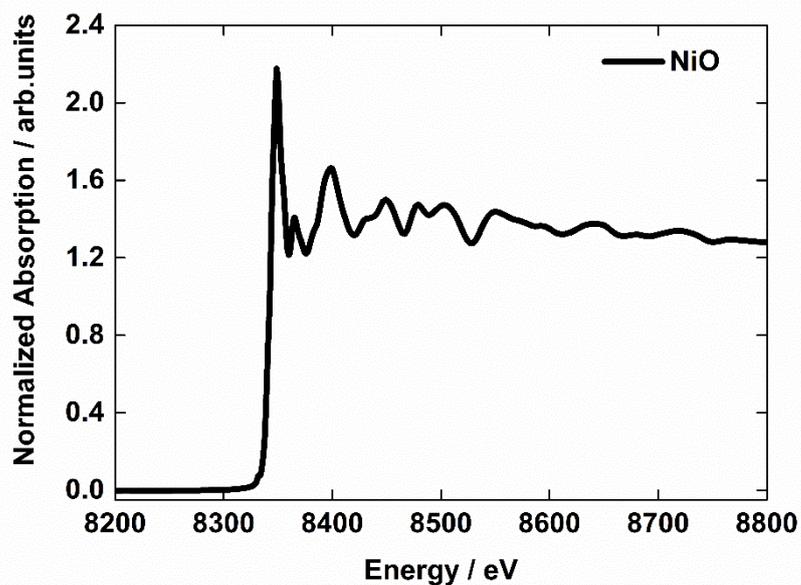
Figure 2-8. Normalized EXAFS spectra after background removal.

Spectrum was normalized, and background was removed by the following Equation (2.5):

$$\chi(E) = \frac{\mu(E) - \mu_0(E)}{\Delta\mu_0(E_0)} \qquad (2.5)$$

Removal of a post-edge smooth background function $\mu_0(E)$ from the spectrum is isolated the XAFS $\chi(E)$ and normalized by the edge jump $\Delta\mu_0(E_0)$ (Figure 2-8). We don't have a measurement of $\mu_0(E)$ (the absorption coefficient without neighboring atoms). We approximate $\mu_0(E)$ by an adjustable, smooth function: a spline. Then, fit a smooth polynomial spline to the XAFS to remove the slowly varying (low-frequency) components of $\mu(E)$.

Then, decide the absorption edge (E_0) from the spectrum, and the raw data convert from energy E to wavenumber (k) using Equation (2.6).

$$k = \sqrt{\frac{2m}{\hbar^2}(E - E_0)} \qquad (2.6)$$
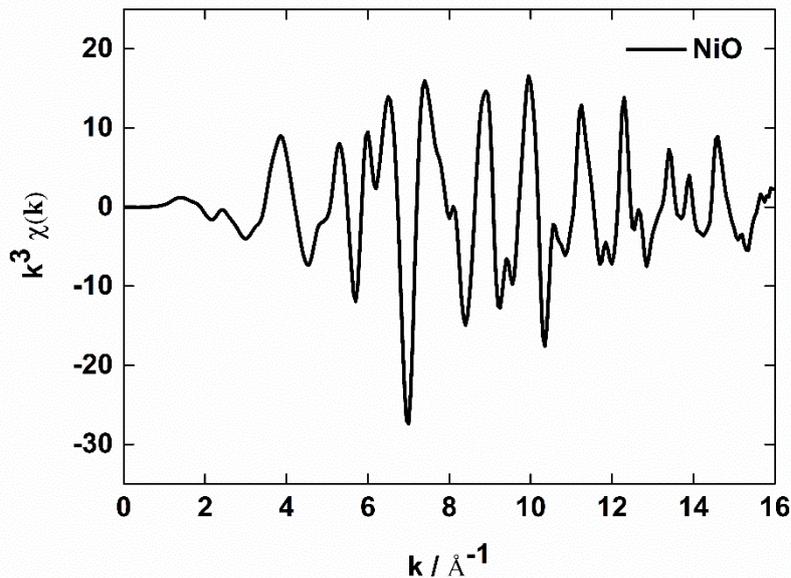
Figure 2-9. k^3 weighted EXAFS data of NiO.

The determination of the atomic absorption is the most important step during the extraction of the EXAFS spectrum. A miscalculation lead to a distorted EXAFS signal and truncated abnormal at a low frequency. The raw EXAFS $\chi(k)$ is usually quickly damped with k at the high wavenumber region and difficult to assess or interpret it. To better visualize the spectrum at the high k range, we multiply the $\chi(k)$ by $k^{n,}$ where n is equal to 1, 2, 3 (Figure 2-9).

2.5.1.3.   Fourier Transform

Lytle, Stern, and Sayers were first applied to separate the different contributions from individual coordination shells of χ(k) into a distance (real) space through Fourier Transform (FT).[14–16] The Fourier transform of the χ(k) EXAFS spectra in a k-space defined between k_{min} and k_{max} provide a radial distribution function (Figure 2-10), which gives us a quantitative interpretation of the local structure around the absorber atom. But the peak position will be approximately 0.2 Å to 0.5 Å shorter than the actual bond distance since the phase shift is disregarded. The minimum value of k_{min} is selected between 2.0-3.0 Å to avoid the multiple scattering around the absorption edge.
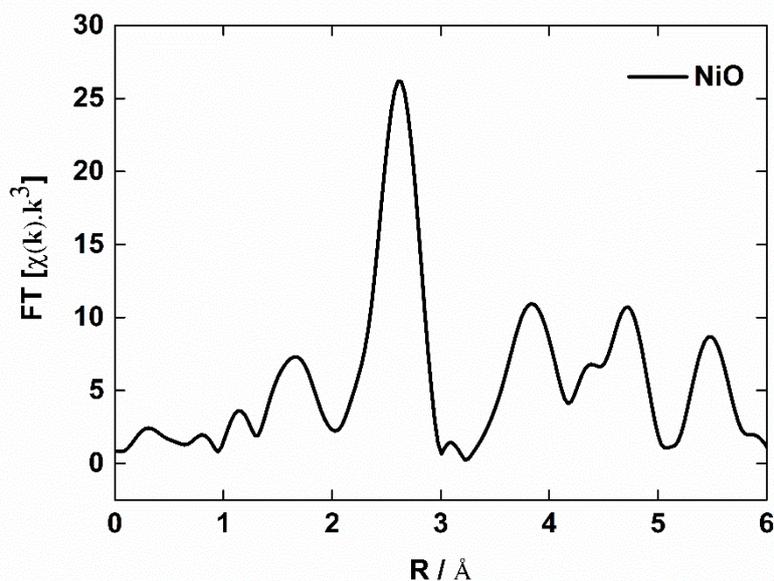
Figure 2-10.   Fourier transform EXAFS of NiO.

The maximum value of k_{max} should be selected as large as possible so long as it can be distinguished from noise. REX2000 was used to calculate the Fourier transform, and inversely Fourier transforms data for curve fitting (CF).

2.5.1.4. Fitting Procedure: Determination of Structural Parameters

For the determination of structural parameters, the fitting procedure is the last step. This step provides us quantitative information of the analyzed sample (coordination number (N), bond length (R), Debye-Waller factor (σ)) through the theoretical fit of the experimental EXAFS spectrum (Figure 2.11). To model the EXAFS, we use the EXAFS Equation (2.7).

$$\chi(k) = S_0^2 \sum_1 \frac{N_i.F_i(k)}{kr_i^2} \exp(-2k^2.\sigma_i^2).\sin(2k.r_i + \varphi_i(k)) \qquad (2.7)$$

Where backscattering amplitude and phase shift are calculated using the theoretical FEFF code. [17,18]
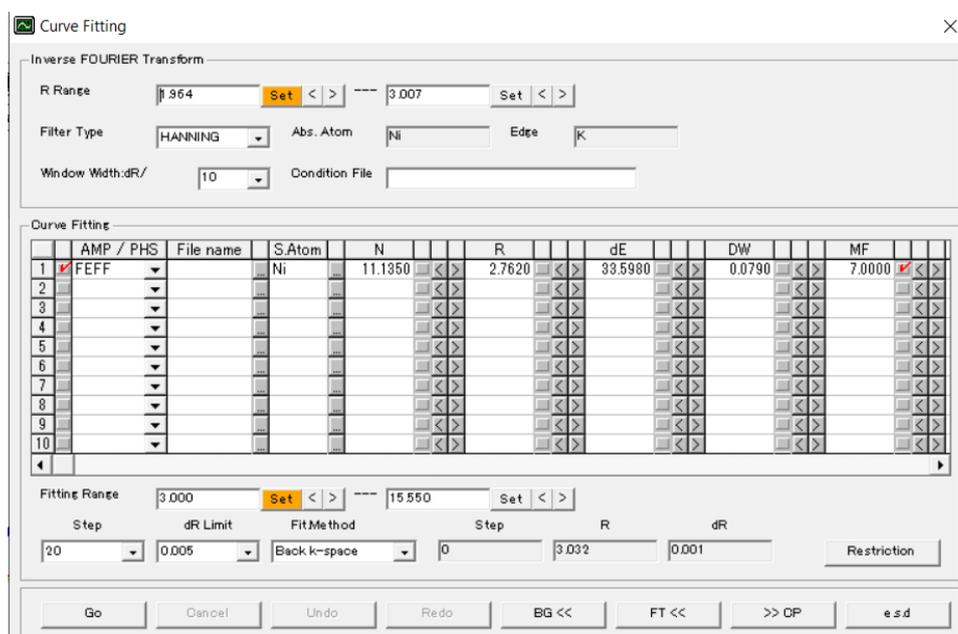
Figure 2-11. Screen capture from REX2000 during curve fitting of NiO.

2.5.2.   XANES Data Analysis

XANES data analysis is relatively simple and done using software REX2000. There is no matter whether $\mu(E)$ is measured in transmission or fluorescence mode. Data reduction steps include possible correction for self-absorption effects, removal of the background using Victorian or Constant method, and normalization of the edge jump to one. The outline of the data reduction step is following as:

1. Convert measured intensities to absorption coefficient $\mu(E)$.

2. Subtract a smooth pre-edge function from $\mu(E)$ to remove any instrumental background and absorption from other edges. In this thesis, the background of the pre-edge region is calculated using the constant method where uses the pre-edge start value as the background for the entire area.

3. Identify the absorption energy E_0, typically calculated from the half maximum of the edge or the maximum of the first derivative of $\mu(E)$.

4. Normalized $\mu(E)$ will have a value near 0 below the edge, and 1 will have above the edge to represent the absorption of one X-ray.

5. Finally, the pre-edge substracted $\mu(E)$ is divided by edge step $\Delta\mu_0(E_0)$. The value of the low-order polynomial is extrapolated to E_o to give the edge step. These normalized spectra are ready for XANES interpretation.

These steps are best shown graphically in Figures 2.12 and 2.13. Throughout these figures, transmission XAFS data from Ni_2P is demonstrated.
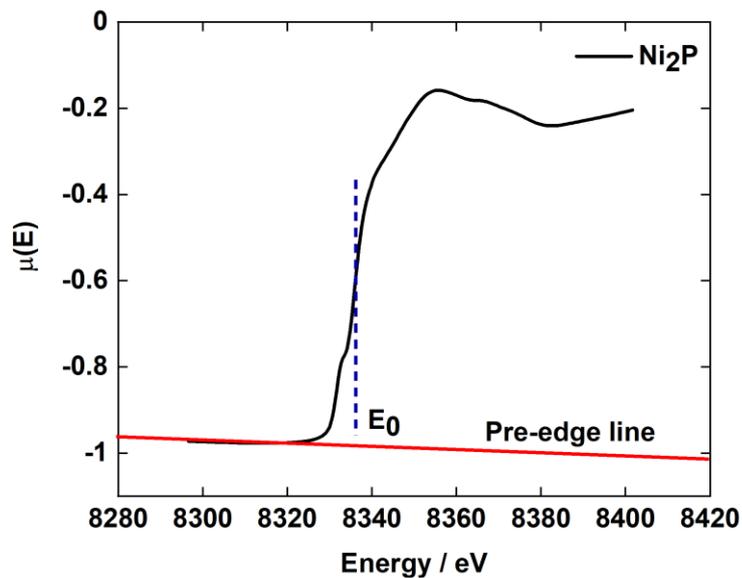
Figure 2-12. The XANES portion of XAFS spectrum and a pre-edge line (or simple polynomial) is fitted to the spectrum below the edge (red line).
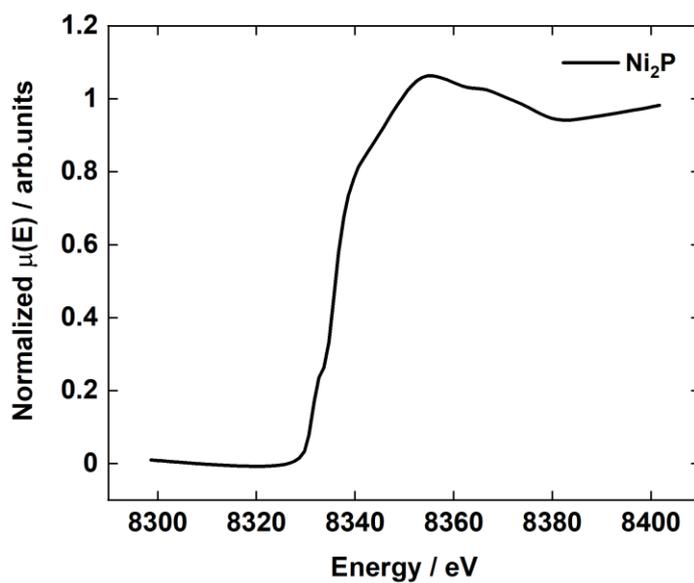
Figure 2-13. Normalized XANES spectra of Ni_2P.

2.5.2.1. Pre-edge Analysis

Pre-edge is the important feature present before the edge. Before analysis and interpretation of the pre-edge features, we need to proceed with further correction. The

49

background of the edge under the pre-edge features needs to be removed by fitting a polynomial spline function. The step smoothly reproduces the slope of the data prior to the pre-edge and immediately following the pre-edge peaks. For extracting the pre-edge, the background may also be described by the tail of a Gaussian or Lorentzian function [19]. The background removal by a spline function is shown in Figure 2-14.
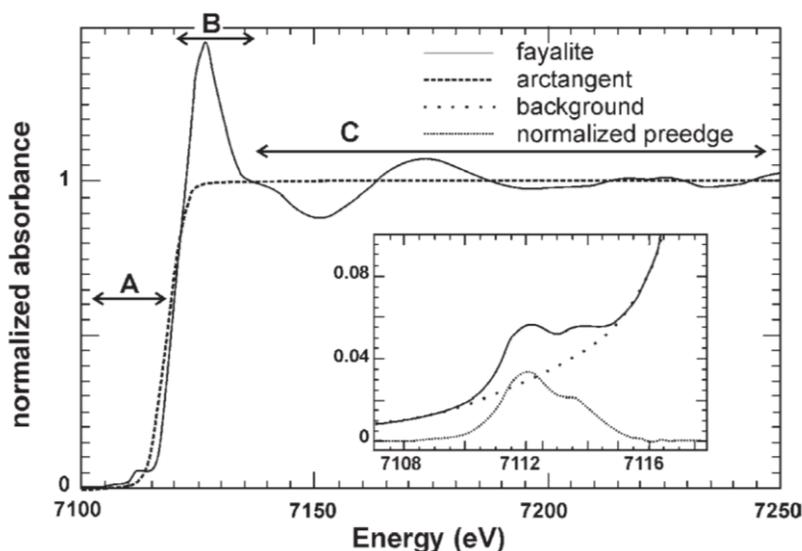
Figure 2-14. The arctan function and normalization of the pre-edge. The inset shows the background fit for the pre-edge region. The pre-edge (A), edge (B), and post-edge (C) regions are indicated. The inset shows the background removal under the pre-edge features.[20]

2.6.   Theoretical XAFS Analysis

XANES analysis is comparatively more complicated than EXAFS analysis. The interpretation of XANES is complicated because there is not a simple analytical or even physical description of XANES. Precise and accurate calculations of all spectral features are not always reliable and still difficult to calculate. Quantitative analysis of XANES spectra using ab initio calculations is not available. There is much chemical (qualitative) information obtained from the XANES spectra, notably oxidation state and coordination environment. The edge position and the shape of XANES spectra are sensitive to oxidation state, coordination environment, and molecular geometry. That's why XANES can be considered as a fingerprint to identify the phases. Although much progress has been made in the theoretical modeling of XANES, most of the applications

of the XANES energy region remain qualitative analysis. But the recent development in multiple scattering formulas has shown that XANES spectra can provide element-specific information on bonding environment, such as coordination number and interatomic distances.

2.6.1. Theoretical FEFF Model

FEFF is an ab initio multiple-scattering code for calculating excitation spectra and electronic structure. Phase shift and backscattering amplitude are calculated for EXAFS analysis, although ab initio calculations are rare for quantitative analysis of XANES. FEFF uses a real-space Green's function approach, including a screened core-hole inelastic losses and self-energy shifts and Debye-Waller factors based on self-consistent, spherical muffin tin scattering potentials. Rehr et al. was developed this FEFF code for theoretical calculations.[17,21] For theoretical model generating, FEFF requires an initial guess of atom placement around the central atom. The initial guess can be used to define the list of x, y, z coordinates for a cluster atom. The program REX2000 has a special interface called "Atoms" that convert crystal structure information into atomic x, y, z coordinates for use in FEFF computations. The Atom interface also inserts a user-defined identifier tag, e.g., Ni_1 and Ni_2, to distinguish nickel atoms in a different shell. FEFF creates muffin tin potentials about the position of each atom.[22] FEFF has many modules corresponding to the calculation procedure. The scattering and phase shift for each path was calculated, and feff00N (N=1,2….) file was generated for CF analysis. The use of crystal structure information provides us a reliable method, FEFF, for providing well space atomic potential for EXAFS simulations. That's why this approach is extremely used to fit EXAFS data in both crystalline and non-crystalline samples.

2.6.2.   Theoretical XAFS Calculations

The theoretical XAFS can be calculated using the FEFF program, which can calculate the details of the scattering processes from a cluster of atoms. This program was developed by Prof. Rehr et al. of the University of Washington. FEFF uses an ab initio real-space multiple scattering (Green's function) approach based on self-consistent, spherical muffin-tin scattering potentials includes improve treatment of many-body effects such as inelastic losses, core hole effects, vibrational amplitudes. In

this research, I use FEFF8 to calculate the theoretical XAFS of the nickel phosphide complex system. This theoretical XAFS spectrum has been compared with the experimental spectrum to determine the unknown phase of the analyzed sample. The details of the FEFF program and calculation procedure are described following as:

FEFF [23,24] calculate theoretical XAFS in two basic ways; first, calculate well space atomic potential followed by calculation of the scattering phase shift, then using this phase shift, scattering paths are found and calculate the scattering amplitudes of each path. This program completes this work in two ways: using an explicit enumeration summation that is appropriate for extended absorption spectra or using the implicit summation of full multiple scattering that is appropriate for near-edge absorption spectra. Finally, these scattering amplitudes are combined to calculate a particular type of spectra like EXAFS or XANES (Figure 2-15).
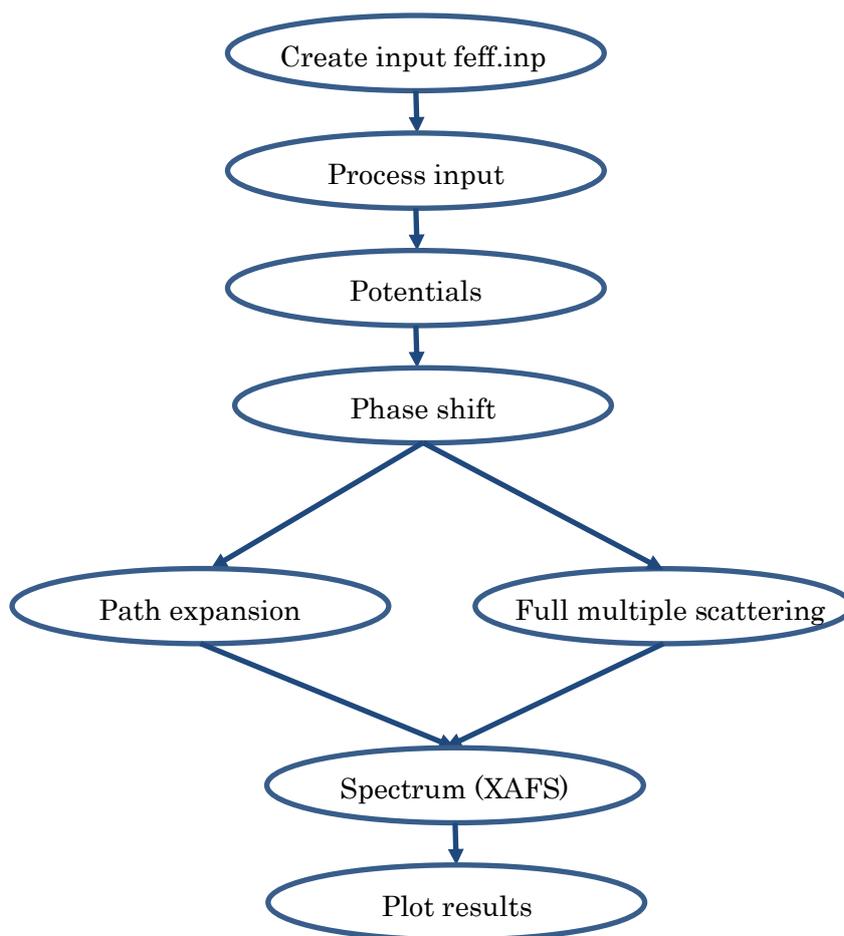
Figure 2-15.   Functional flow chart of the FEFF program.

To apply the FEFF program for calculating EXAFS or XANES, FEFF requires an atomic structure that indicates the position of all the atoms in the lattice. The FEFF program consists of a set of program modules that control by a single input file, "feff.inp".[25] The program "REX2000" has a special interface called ÄTOM" that can converts crystal structure information into a cluster of atoms and provides a list of atomic cartesian X, Y, Z coordinates for use in the FEFF input file (feff.inp file). Another third-party tool, "webatoms" developed by B. Ravel that can set up "feff.inp" file based on atomic positions or crystallographic information. The input file "feff.inp" is a loosely formatted and line-oriented text file that can modify to what you want to do. Each type of input can be read by the program in on a line starting with a CARD: a keyword possibly followed by some numbers or words. The sequence of keywords is arbitrary. The card used default values if any card or optional data is omitted. Most calculations do require the POTENTIALS card and either the ATOMS card or the OVERLAP card. Together, the POTENTIALS and ATOMS/OVERLAP cards specify the physical structure of the molecule or solid one is interested in. FEFF uses Cartesian coordinates and Angstrom units. There are many optional cards to specify the material property to calculate and control how FEFF calculates it. All distances are in Angstrom (Å), and energies are in electron–volts (eV).

Table 2-1.   FEFF input file component for XANES and EXAFS calculations.

XANES	EXAFS
Title Ni	Title Cu complex
CONTROL 1 1 1 1 1 1	EDGE k
EXCHANGE 0 0 0 0	S02 1.0
SCF 5.0 0 100 0.2	CONTROL 1 1 1 1 1 1
XANES 5.0 0.07 0.0	CORRECTIONS 4 0 1.0
FMS 5.0 0.0	SIG2 0.006
POTENTIALS	EXAFS 20.0
0 28 Ni	RPATH 3.5
1 28 Ni	POTENTIALS
	0 29 Cu
	1 28 Cu
	2 8 O
	3 7 N

For XANES or EXAFS calculations, separate input files have to be generated.[25] Some of the components of the "feff.input" file for XANES and EXAFS are shown in Table 2-1. The regular XAS output file 'xmu.dat' is used for calculated spectrum that compared with a measured spectrum from an experiment.

2.6.2.1. Theoretical XANES Calculations Using FEFF

XANES calculations usually take more time and require more attention than EXAFS calculations. The self-consistent (SCF) and full multiple scattering (FMS) is must be required to run the "feff.inp" file in FEFF8 for XANES calculations. The SCF and FMS adjust the number of atoms used in the calculation. The number of atoms included in the calculations process until no distinct change occurs in the simulated spectrum indicating convergence is reached. The results can be better with larger clusters, but typically, the convergence is about 100-300 atoms. In the present calculation for XANES spectra, self-consistent (SCF) potential with a cluster radius of 5.0 Å and full multiple scattering (FMS) cluster size 5.0 Å have been used. The theoretical XANES spectra for Ni K-edge is shown in Figure 2-16. In this figure, the experimental and theoretical XANES spectra have been compared.
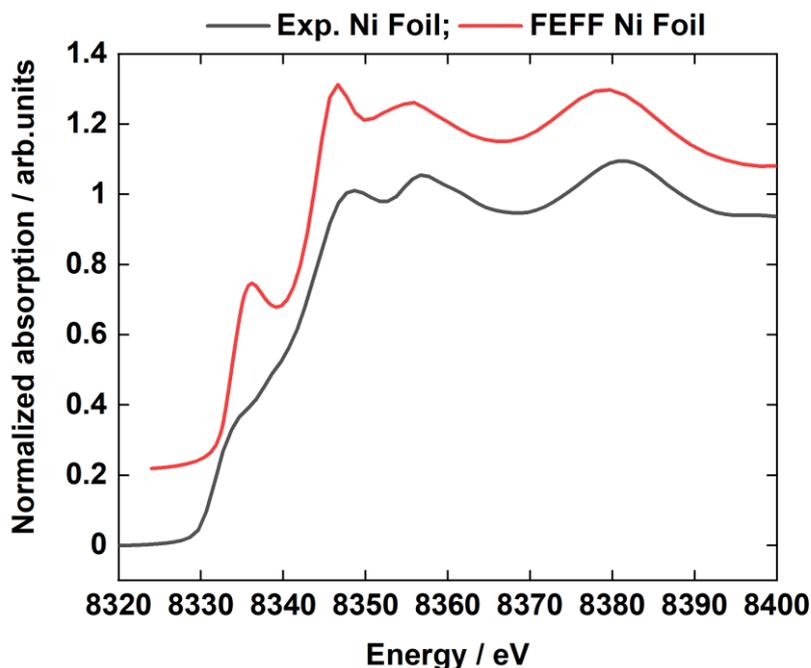
Figure 2-16. Comparison of experimental Ni K-edge XANES with theoretical XANES spectra of Ni foil.

2.6.2.2.   Theoretical EXAFS Calculations Using FEFF

The self–consistent potential is necessary for the calculation of the scattering phase shifts. The calculation of potentials and phase shifts can be taken relatively slow, so it is usually best to run it only once and use the results while studying the paths and XAFS. If the sample is completely unknown, only single scattering paths can be created explicitly. Because the number of possible paths increases exponentially with the total path length, we have started with a short total path length and then examined few paths and gradually increased the total path length. If the model changes significantly, the phase shifts should be recalculated. Any time change the phase shift, XAFS parameters will also have to be recalculated.[25] The EXAFS spectrum has been obtained as the sum of these paths in "xmu.dat" file for Cu complex system is shown in Figure 2-17. In this Figure, the experimental and the theoretical spectrum has also been compared.
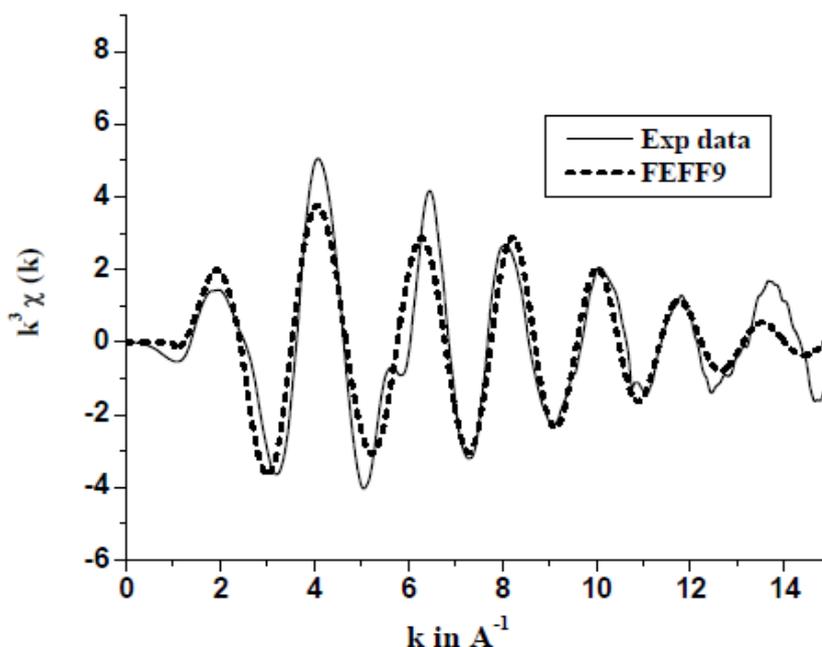
Figure 2-17.   Comparison of experimental Cu K-edge EXAFS with theoretical EXAFS spectra of Cu complex.[26]

2.7.   Theoretical FPMS Model

Full potential multiple scattering (FPMS) is a brand new method for XANES calculations. Conventional theoretical XANES has been calculated by the FEFF

method, which uses Multiple Scattering Theory (MST) over a Muffin-Tin (MT) approximation.[21, 27] The muffin-tin approximation is a shape approximation, where the potential is assumed to be spherically symmetric in each atomic sphere and constant outside the spheres, which is known as the interstitial region. This MT approximation is good for close-packed systems and works poorly for covalently bonded and low-dimensional systems and diamond-like structures.[28–31] To overcome this problem, the pioneering work done by Williams&Morgan (1974) reformulated the MS theory for arbitrary local potentials by partitioning the space with space-filling truncated cells. When the space-filling cells or Voronoi polyhedra do not contain an atom or are in the interstitial region but still contains charge density, it is called an empty cell (EC). Hatada et al. (2010) developed the FPMS code, which provides a straightforward extension of MS theory in the MT approximation.[30]

2.7.1.   Theoretical XANES calculation Using FPMS

The FPMS code focuses on the calculations of XANES spectra.[32] It incorporates a part of ES2MS code, an interface to use charge densities and potentials generated by electronic structural code. FPMS is incorporated into the MXAN code (the so-called FP-MXAN code) to perform structural fitting of XANES spectra without the need for the MT approximation.[33]

Figure 2-18.   Screen capture from FPMS input file "data.ms" for FPMS calculations.

The code is platform-independent; it may run on Linux, Windows, and Mac OS X. The prepared executable is provided only for the serial mode, and it is stand-alone; no additional programs or libraries are required. The input file must be named as "data.ms". For non-MT calculation, you should add NMT = "NM" and truncate = .true. (Voronoi), or truncate = .false. (ASA). Some of the components of the "data.ms" file for $GeCl_4$ are shown in Figure 2-18.

Figure 2-19 shows the application of the FPMS method to the XANES calculation of the Ge K-edge absorption spectra of the tetrahedral molecule $GeCl_4$.[34] The MT approximation could never reproduce the first bump after the main peak presence in $GeCl_4$ XANES spectra where FPMS successfully reproduced this one. The details of the FPMS analysis have been discussed in Chapter 5.
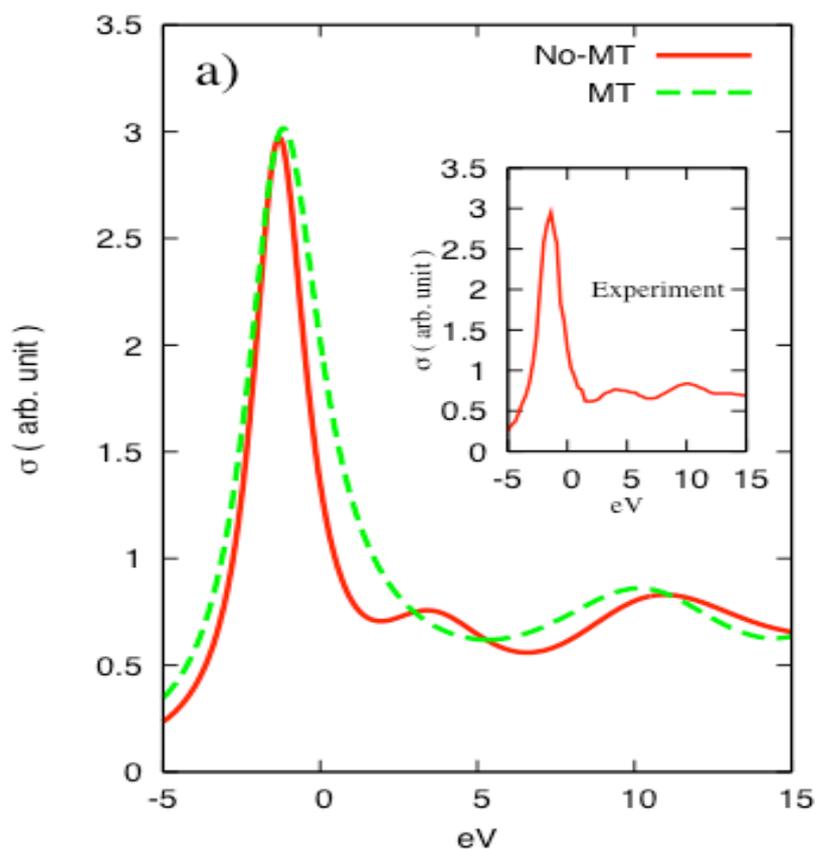
Figure 2-19.   Comparison of MT and FPMS (NMT) XANES spectra of $GeCl_4$.

Reference

1. Iwasawa, Y., Asakura, K. & Tada, M. *XAFS Techniques for Catalysts, Nanomaterials, and Surfaces*. *XAFS Techniques for Catalysts, Nanomaterials, and Surfaces,* (Springer, chem. 2017).

2. J. D. Hanawalt. The dependence of X-ray Absorption Spectra upon Chemical and Physical State. *Phys. Rev.* **37**, 715 (1931).

3. Daley, T. Advanced Characterisation of Catalytic Materials Using Synchrotron Radiation Techniques, Doctoral dissertation (2015).

4. Blewett, J. P. Synchrotron Radiation – Early History. *J. Synchrotron Radiat.* **5**, 135–139 (1998).

5. Hofmann, A. *Synchrotron radiation*. *Reviews of Accelerator Science and Technology* **01**, (World Scientific, 2008).

6. Tsoulfanidis, N. & Landsberger, S. *Measurement and Detection of Radiation*. (CRC Press, 2015).

7. Bunker, G. *Introduction to XAFS, A Practical Guide to X-ray Absorption Fine Structure Spectroscopy*. *Introduction to XAFS* (Cambridge University Press, 2010).

8. Newville, M. Fundamentals of XAFS. *Rev. Mineral. Geochemistry* **78**, 33–74 (2014).

9. Calvin, S. *XAFS for Everyone*. (CRC Press, 2013).

10. Asakura, K. Analysis of EXAFS. in (ed. Iwasawa, Y.) **58**, 33–58 (World Scientific, 1996).

11. Koningsberger, D. & Prins, R. *X-ray absorption: Principles, applications, techniques of EXAFS, SEXAFS, and XANES*. *Endeavour* vol. 12 (Wiley, 1988).

12. Taguchi, T., Ozawa, T. & Yashiro, H. REX2000: Yet another XAFS analysis package. *Phys. Scr. T* **T115**, 205–206 (2005).

13. Taguchi, T. REX2000 version 2.5: Improved DATA handling and enhanced user-interface. *AIP Conf. Proc.* **882**, 162–164 (2007).

14. Sayers, D. E., Stern, E. A. & Lytle, F. W. New technique for investigating

noncrystalline structures: Fourier analysis of the extended x-ray-absorption fine structure. *Phys. Rev. Lett.* **27**, 1204–1207 (1971).

15. Lytle, F. W., Sayers, D. E. & Stern, E. A. Extended x-ray-absorption fine-structure technique. II. Experimental practice and selected results. *Phys. Rev. B* **11**, 4825–4835 (1975).

16. Stern E A, Sayers D E & Lytle F W. Extended x-ray-absorption fine-structure technique. III. Determination of physical parameters. *Phys. Rev. B* **11**, 4836–4846 (1975).

17. Rehr, J. J. *et al.* Ab initio theory and calculations of X-ray spectra. *Comptes Rendus Phys.* **10**, 548–559 (2009).

18. Rehr, J. J. & Albers, R. C. Theoretical approaches to x-ray absorption fine structure. *Rev. Mod. Phys.* **72**, 621–654 (2000).

19. Farges, F. *et al.* The effect of redox state on the local structural environment of iron in silicate glasses: A combined XAFS spectroscopy, molecular dynamics, and bond valence study. *J. Non. Cryst. Solids* **344**, 176–188 (2004).

20. Henderson, G. S., De Groot, F. M. F. & Moulton, B. J. A. X-ray absorption near-edge structure (XANES) spectroscopy. *Rev. Mineral. Geochemistry* **78**, 75–138 (2014).

21. Rehr, J. J. & Albers, R. C. Theoretical approaches to x-ray absorption fine structure. *Rev. Mod. Phys.* **72**, 621–654 (2000).

22. Zabinsky, S. I., Rehr, J. J., Ankudinov, A., Albers, R. C. & Eller, M. J. Multiple-scattering calculations of x-ray-absorption spectra. *Phys. Rev. B* **52**, 2995–3009 (1995).

23. Ankudinov, A. & Rehr, J. Relativistic calculations of spin-dependent x-ray-absorption spectra. *Phys. Rev. B - Condens. Matter Mater. Phys.* **56**, R1712–R1716 (1997).

24. Ankudinov, A. & Ravel, B. Real-space multiple-scattering calculation and interpretation of x-ray-absorption near-edge structure. *Phys. Rev. B - Condens. Matter Mater. Phys.* **58**, 7565–7576 (1998).

25. Rehr, J. J., Ankudinov, A. & Ravel, B. *User's Guide, FEFF v.8.40.* http://monalisa.phys.washington.edu/feffproject-feff-documentation.html (2006).

26. Gaur, A. & Shrivastava, B. D. Theoretical calculations of X-ray absorption spectra of a copper mixed ligand complex using computer code FEFF9. *J. Phys. Conf. Ser.* **534**, 5–10 (2014).

27. Newville, M. *et al.* Analysis of multiple-scattering XAFS data using theoretical standards. *Phys. B Phys. Condens. Matter* **208–209**, 154–156 (1995).

28. Hatada, K., Hayakawa, K., Benfatto, M. & Natoli, C. R. Full-potential multiple scattering for x-ray spectroscopies. *Phys. Rev. B - Condens. Matter Mater. Phys.* **76**, (2007).

29. Hatada, K., Hayakawa, K., Benfatto, M. & Natoli, C. R. Full-potential multiple scattering for core electron spectroscopies. *J. Phys. Condens. Matter* **21**, (2009).

30. Hatada, K., Hayakawa, K., Benfatto, M. & Natoli, C. R. Full-potential multiple scattering theory with space-filling cells for bound and continuum states. *J. Phys. Condens. Matter* **22**, (2010).

31. Xu, J. *et al.* X-ray absorption spectra of graphene and graphene oxide by full-potential multiple scattering calculations with self-consistent charge density. *Phys. Rev. B - Condens. Matter Mater. Phys.* **92**, 1–11 (2015).

32. K. Hatada, J. Xu, K. Hayakawa, C. R. N. FPMS : Data analysis for XANES spectra by Non-Muffin tin. https://www.lnf.infn.it/theory/CondensedMatter/fpms.html (2005).

33. Hayakawa, K., Hatada, K., Della Longa, S., D'Angelo, P. & Benfatto, M. Progresses in the MXAN fitting procedure. *AIP Conf. Proc.* **882**, 111–113 (2007).

34. Filipponi, A. & D'Angelo, P. Accurate determination of molecular structures by x-ray absorption spectroscopy. *J. Chem. Phys.* **109**, 5356–5362 (1998).

Chapter 3

EXAFS Curve Fitting Analysis for NOCM Catalytic Active Phase Determination of Ni Phosphide Catalysts

3.1. Introduction

Methane is an important raw material for the production of fuels and chemicals. Methane can be converted to higher hydrocarbon in two ways, either via syngas or directly into C_2 hydrocarbon. But the direct conversion of methane to higher hydrocarbons without going through the intermediate syngas production would be potentially more economical and environmentally friendly. Recently, Yamanaka et al. screened catalytic activities of various Ni-M/SiO$_2$ compounds (M = metals or metalloids) for the non-oxidative coupling of methane (NOCM) reactions using a fixed bed-gas-flow system at 1173 K and found that SiO$_2$-supported Ni phosphide catalysts showed the highest activity for the NOCM reaction to produce hydrocarbons at 1173 K among the others. [1,2] They also observed the effect of phosphorus content on the NOCM reaction activities over initial ratio Ni:P ratios of 1:1, 2:1, 3:1. The NOCM activity was high for the initial Ni:P ratio of 1:1, and the yields of hydrocarbons of initial Ni:P ratios of 2:1, 3:1 extremely decreased (Figure 3-1). These results indicated that the catalyst Ni-P/SiO$_2$ with an initial Ni:P ratio of 1:1 is more effective for the non-oxidative conversion of methane to higher hydrocarbon. But the structure of Ni-P/SiO$_2$ with initial Ni:P = 1:1 is not unveiled. In my research, I applied the EXAFS technique to elucidate the active structure of Ni phosphide catalysts with an initial Ni:P ratio of 1:1.

Extended X-ray absorption fine structure (EXAFS) spectroscopy is a popular tool for the determination of local structures in various materials. Because it provides us element-specific information and can be used for materials in any physical state (solids, liquids, gases).[3] To extract accurate interatomic distances (R), coordination number (N), and Debye-Waller factors (σ^2) from EXAFS spectra requires comparison with well known "standard" phase-shift and backscattering amplitude functions, derived from either experimental reference compounds or theoretical calculations.[4] The recent development of ab initio theoretical standards such as FEFF, which is readily available to users in automated computer codes, directly provides us "standard" phase shift and backscattering amplitude functions. Quantitative analysis of EXAFS spectra using

experimental standards requires compounds in which the atomic environment of the absorber is similar in the model and the unknown. Normalized, background-subtracted EXAFS for model and unknown spectra are filtered over a similar k-range and Fourier transformed to produce radial structure functions. The non-linear least square curve fitting (CF) analysis was used to search for the lowest R-factor in k- or r-space.[5] The curve fitting (CF) analysis provide structural parameters such as the coordination number (N), the bond length (R), and the Debye-Waller (σ^2) for each coordination shell. Although the CF results give a reasonably low R-factor, it would be challenging to execute the structural parameters. A good reference sample CF structural information can help to confirm the analysis sample structure. In this case, I have a reference sample Ni_2P that I can compare with the analyzed sample CF results.
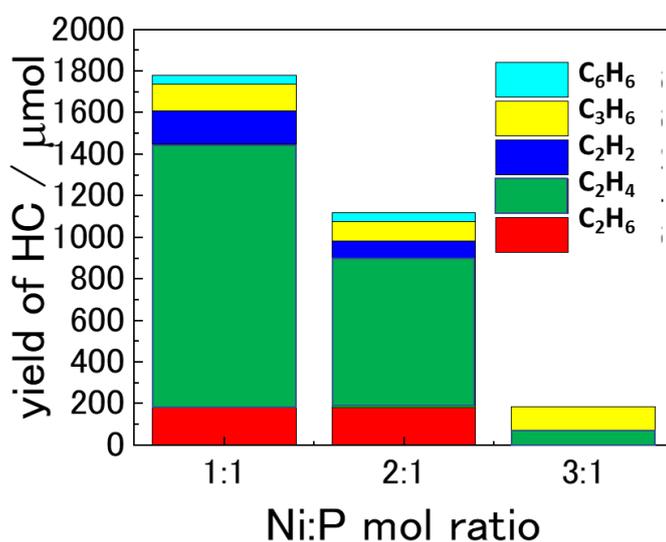
Figure 3-1. Hydrocarbon yield of CH_4 for non-oxidative coupling of methane (NOCM) reaction.

3.2. Structural Properties of Nickel Phosphide (Ni_2P)

Ni_2P catalysts show high catalytic activity in hydrogen-related reactions, such as hydrodesulfurization reactions[6,7], hydrodeoxidation[8], and hydrogen evolution reactions[9]. Ni_2P has a crystal structure, as shown in Figure 3-2.[10] Along the c axis, two-layer structures are alternatively stacked. One is called Ni_3P, and the other is Ni_3P_2. The Scanning Tunneling Microscopy (STM) and Low Energy Electron Diffraction (LEED) of the Ni_2P single crystal showed the Ni_3P_2 was mainly present on the Ni_2P [0001]

surface.[11–13] The details of the Ni$_2$P crystal structure describe as below:

Ni$_2$P has a hexagonal structure that belongs to the space group $P\bar{6}2m$ with lattice parameters a = 0.5859 nm and c = 0.3382, as shown in Figure 3-2.
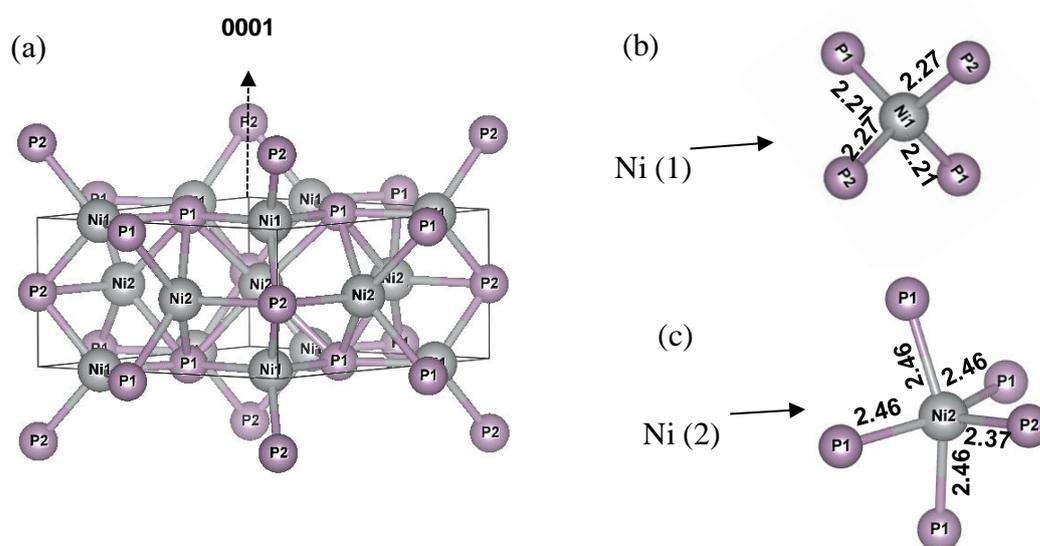
Figure 3-2. a) The crystal structure of Ni$_2$P. b) The tetragonal Ni (1) site; c) The square pyramidal Ni (2) site. Legend: pale pink and dark grey indicates P and Ni, respectively. The bond distance unit is Å.

Ni$_2$P consists of two consecutive planes denoted as Ni$_3$P$_2$ and Ni$_3$P alternatively along the (0001). There are two types of P atoms, P (1) and P (2), as well as two types of Ni atoms, Ni (1) and Ni (2), as shown in Figure 3-2. Ni (1) site surrounded by four P atoms in a near tetrahedral manner, producing Ni-P distances of 2.21 Å [with two P(1)] and 2.27Å [with two P (2)]. The Ni (2) site is surrounded by five P atoms in a square pyramidal structure, in which one Ni-P bond is 2.37 Å with P (2) and the others four Ni-P bonds are 2.46 Å with P (1).

3.3. Experimental

3.3.1. Preparation of Catalysts

The SiO$_2$-supported Ni phosphide catalysts with initial Ni:P ratios of 1:1, 2:1, and 3:1 were prepared by a conventional impregnation method, followed by

temperature-programmed reduction. The catalytic activities were tested at 1173 K using a conventional fixed-bed gas-flow system (Figure 3-3). The sample was denoted as Ni-P/SiO$_2$ (Ni:P = X:Y, Z h), where X:Y represents the initial Ni:P molar ratio and Z is the reaction time. Professor Yamanaka and his research group prepared this samples[2]; preparation and experimental details are described below as:

The samples SiO$_2$-supported Ni phosphide catalysts with initial Ni:P ratios of 1:1, 2:1, and 3:1 were prepared from Ni(NO$_3$)$_2$.6H$_2$O and (NH$_4$)$_2$HPO$_4$, which were dissolved in deionized water. To form a suspension, added SiO$_2$ powder in the solution. Before use to CARiACT Q-3 powder was calcined in air at 1273 K for 3 h to remove the micropores. The precursor was dried and calcined at 393 K for 2 h and 773 K for 3 h, respectively. The obtained Ni-P/SiO$_2$ powder was reduced with hydrogen at 773 K for 1 h with the rate of 10 K min^{-1} for the catalyst screening. Before performing each NOCM reaction, the catalyst was purged by 10 mL min^{-1} of Ar while the temperature increased from room temperature to 1173 K at a rate of 25 K min^{-1}. Pure methane flowed at 10 mL min^{-1} into the reactor at 1173 K. The catalytic activity of Ni-P/SiO$_2$ with Ni:P ratios of 1:1, 2:1, and 3:1 compounds were screened using a fixed bed gas flow system. After confirming uniform temperature along the catalyst bed, pure methane of 10 mL min^{-1} flowed into the reactor. The catalytic activity was observed for 3 h, 9 h, and 12 h. The product yields like ethane, ethylene, acetylene, and propylene were analyzed using a gas chromatograph every 30 minutes.
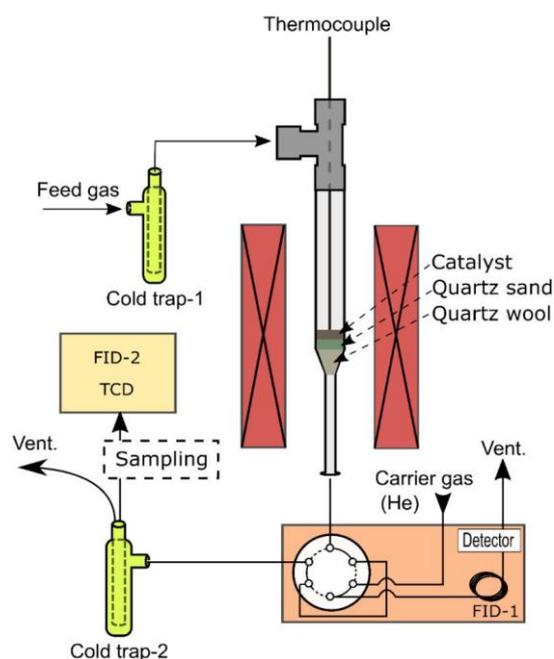
Figure 3-3. Schematic diagram of experimental apparatus for the NOCM reaction.[2]

3.4. XAFS Measurement

EXAFS measurements were carried out at BL9C of the Photon Factory (PF) in Institute for Structure Materials Science, High Energy Accelerator Research Organization (KEK) operated at 2.5 GeV, 450 mA. The emitted X-ray was monochromatized by a Si (111) double crystal and focused with an Rh-coated bent cylindrical mirror. The Ni K-edge data were collected in transmission mode. The incident and transmitted X-rays were detected by 100% N_2 gas-filled and (15% N_2 + 85% Ar) mixed-gas-filled ionization chambers, respectively.

3.4.1. Data Processing

At first, the raw data is reduced and then analyzed data using the EXAFS CF method. As a reference, the details of the different steps for extracting the oscillatory part $\chi(k)$ vs. k data from the raw experimental $\mu(E)$ vs. E data of an X-ray absorption spectrum for Ni_2P have been described in this section. All these steps have been carried out by the computer program REX2000.[5,14] Figure 3-4 shows stepwise the raw data analysis. A brief description of those processes has been described in Chapter 2 (Section 2.5).
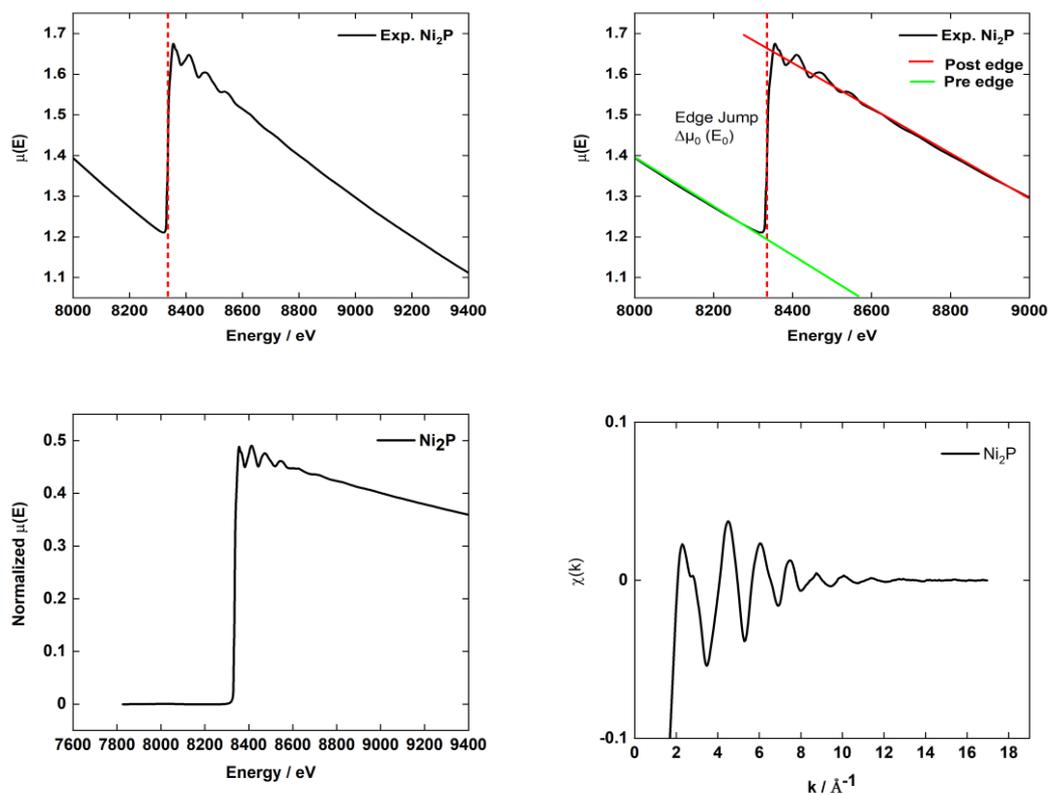
Figure 3-4. Stepwise raw X-ray absorption data analysis of Ni K-edge for Ni_2P.

Finally, $\chi(k)$ is multiplied by k^n (n=1,2,3) better to visualize the spectrum (Figure 3-5 (a)). The Fourier transform was also done by REX2000. The Fourier transformation of the Ni_2P is shown in Figure 3-5 (b). The raw data analysis of three analyzing samples $Ni-P/SiO_2$ with different Ni:P ratios of 1:1, 2:1, and 3:1 followed the same process.

a)   b)
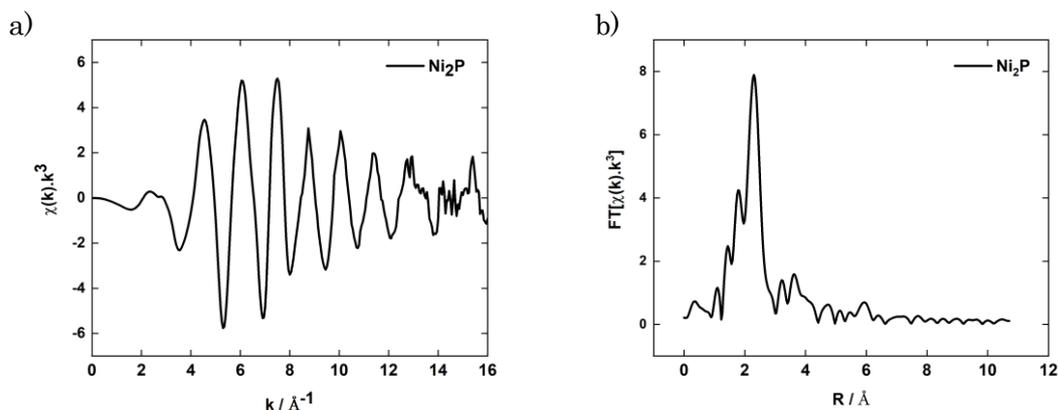
Figure 3-5. (a) EXAFS $\chi(k).k^3$ vs. k data of Ni K-edge for Ni_2P. (b) Fourier transform of Ni K-edge EXAFS data for Ni_2P.

3.4.2.   Generating Theoretical Models

To extract the quantitative information (N, R, σ^2) from EXAFS data, the data has to be compared with accurately known "standard," i.e., either theoretical model or experimental reference. Generally, theoretical models are preferable over experimental references because the computer program for the theoretical calculation is easily available.[16] In this research, the theoretical amplitude and phase shift functions of Ni–Ni and Ni–P atom-pairs were calculated by FEFF8.[16] The FEFF program can generate the theoretical model, and REX2000 adjusts the structural parameters in the EXAFS equation until a list square fit is obtained between theoretical and experimental EXAFS data. Hamilton's method was used to estimate the error of CF analysis.[17]

3.5.   Results and Discussion

3.5.1.   FT of EXAFS Data for Ni foil, NiO and Ni_2P

In order to understand the effect of phosphorus content on the catalyst, the extended X-ray absorption fine structure (EXAFS) data was analyzed. Figure 3-6 shows the Ni

K-edge EXAFS results for Ni foil, NiO, and Ni_2P.
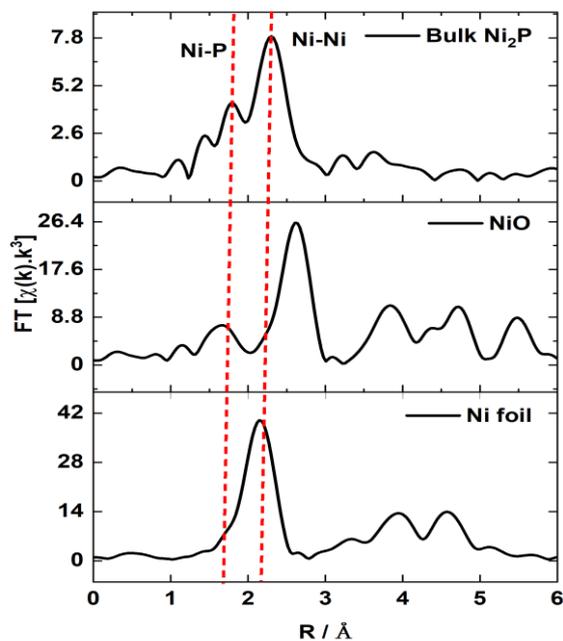
Figure 3-6. Comparison of nickel K-edge Fourier transforms of Ni foil, NiO, and Ni_2P.

The Ni foil and NiO show the main peak corresponding with the Ni-Ni bond distance. In contrast, the bulk Ni_2P shows the main peak with a shoulder at a lower interatomic distance. This shoulder is corresponding with Ni-P bond distance. There is no such agreement with the features of Ni foil and NiO. The reference Ni_2P sample shows two distingue peaks: the main peaks of Ni-Ni and the first peak of Ni-P, comparable with the Ni-P/SiO_2 sample of different Ni:P ratios of 1:1, 2:1, and 3:1.

3.5.2. EXAFS Spectrum for Reference Ni_2P and Ni-P/SiO_2 Sample

Ni K-edge EXAFS spectrum for both fresh and spent samples are compared with reference Ni_2P after background subtraction in Figure 3-7. The three different Ni:P ratios samples give different EXAFS oscillations. Figure 3-7(b) shows the EXAFS oscillation of the sample Ni-P/SiO_2 (Ni:P = 1:1), similar to that of the Ni_2P reference, indicating that Ni-P/SiO_2 (Ni:P = 1:1) had the Ni_2P structure. Ni-P/SiO_2 (Ni:P = 2:1) and Ni-P/SiO_2 (Ni:P = 3:1) have quite different oscillations from the Ni_2P reference. This

different oscillation is indicating different Ni phosphide phase forms in these two samples.
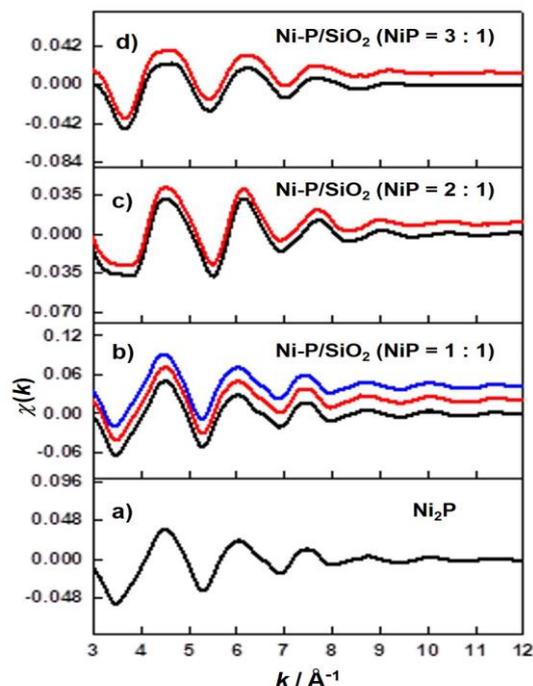
Figure 3-7. Comparison of nickel K-edge EXAFS spectrum: a) bulk Ni_2P, b) Ni-P/SiO_2 (Ni:P = 1:1), c) Ni-P/SiO_2 (Ni:P = 2:1), d) Ni-P/SiO_2 (Ni:P = 3:1). The reaction times for the Ni-P/SiO_2 samples are 0 h (black), 3 h (red), and 12 h (blue).

3.5.3.   FT for Reference Ni_2P and Ni-P/SiO_2 Sample

The Fourier transform of the Ni K-edge EXAFS spectra and the fresh and spent samples have been shown in Figures 3-8. The Ni-P/SiO_2 (Ni:P = 1:1) showed two distinct peaks in this Fourier transform (Figure 3-8(b)). The main peak and first peak are corresponding to the Ni-Ni and Ni-P bond distances, respectively. Compared to the reference Ni_2P, the Fourier transform depicted a similar pattern to that of Ni_2P. The situation is different for the sample Ni-P/SiO_2 (Ni:P = 2:1) (Figure 3-8(c)). In this case, the Ni-P peak was reduced to a shoulder, and the Ni-Ni peak shifts to the metallic position. It is evident that this sample is different from Ni_2P. For the Ni-P/SiO_2 (Ni:P =3:1), the two Fourier transform peaks were merged into one, and a broad peak appears at a shorter bond distance (Figure 3-8(d)). Clearly, in this case, there is disruption from the Ni_2P structure.

68
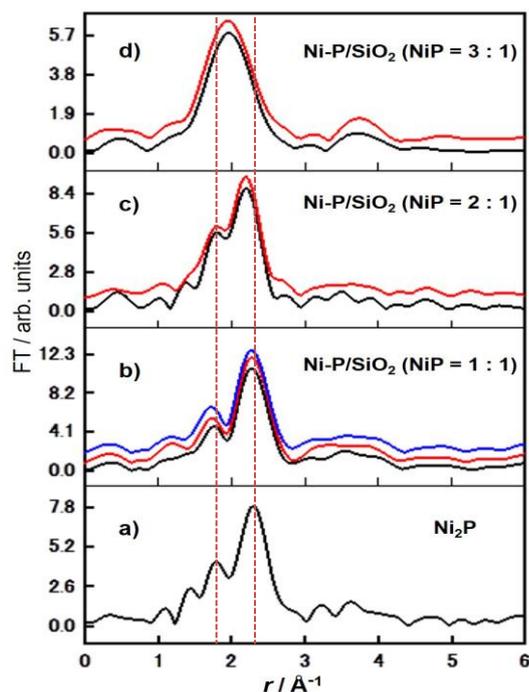
Figure 3-8. Comparison of Ni K-edge EXAFS oscillation results Fourier transforms: a) reference Ni_2P , b) Ni-P/SiO$_2$ (Ni:P = 1:1), c) Ni-P/SiO$_2$ (Ni:P = 2:1), d) Ni-P/SiO$_2$ (Ni:P = 3:1). The reaction times for the Ni-P/SiO$_2$ samples are 0 h (black), 3 h (red), and 12 h (blue).

3.5.4. Curve Fitting Results for Reference Ni$_2$P and Ni-P/SiO$_2$ Sample

Table 3-1 shows the curve fitting analysis of the peaks in Figure 3-8. The curve fitting analysis was conducted for EXAFS oscillations [$\chi(k).k^3$] in the k space which was obtained by backscattering Fourier transform filtered FT spectra. The curve fitting analysis indicated the Ni-P and Ni-Ni bond distances were 2.19 Å and 2.62 Å, respectively, for Ni-P/SiO$_2$ (Ni:P = 1:1). These bond distances agree well with those found in Ni$_2$P reference within the error bar. In the case of Ni-P/SiO$_2$ (Ni:P = 2:1), the curve fitting analyses indicated the Ni-Ni bond distance 2.52 Å while that of Ni-P was 2.18 Å. But the Ni-Ni and Ni-P distances were 2.45 Å, and 2.28 Å observed in Ni-P/SiO$_2$ (Ni:P = 3:1) from the curve fitting analysis. The Ni-Ni bond distance was shorter than that of Ni metal.

69

Table 3-1. Curve fitting results of the Ni K-edge EXAFS spectra for the Ni$_2$P reference and different samples with initial Ni:P ratios of 1:1, 2:1, and 3:1.

Samples	Ni-Ni				Ni-P				R%[e]
	CN[a]	R (Å)[b]	σ(Å)[c]	$\Delta E(eV)$[d]	CN[a]	R (Å)[b]	σ(Å)[c]	$\Delta E(eV)$[d]	
				Fresh samples					
Ni$_2$P reference	4.0±0.3	2.62±0.02	0.092	5.4	1.0±0.3	2.21±0.02	0.071	-5.1	0.5
Ni-P (1:1, 0h)	4.6±0.6	2.62±0.02	0.085	3.4	1.3±0.3	2.19±0.02	0.081	-7.5	0.3
Ni-P (2:1, 0h)	4.2±0.3	2.52±0.02	0.093	-1.1	0.6±0.3	2.18±0.03	0.036	-7.3	0.1
Ni-P (3:1, 0h)	4.6±0.9	2.45±0.02	0.116	-7.2	2.0±0.5	2.28±0.02	0.139	-3.6	0.5
				Spent samples					
Ni-P (1:1, 3h)	4.5±0.8	2.62±0.03	0.082	3.5	1.5±0.5	2.18±0.03	0.084	-9.8	0.5
Ni-P (2:1, 3h)	4.3±0.3	2.53±0.03	0.095	-0.7	0.7±0.3	2.17±0.03	0.058	-8.8	0.3
Ni-P (3:1, 3h)	4.6±1.0	2.46±0.02	0.117	-6.6	2.1±0.6	2.28±0.03	0.131	-2.3	0.4

[a] Coordination number.
[b] Interatomic distance.
[c] Debye-Waller factor.
[d] Edge shift.
[e] Residual factor.

3.5.5. Structure Stabile for NOCM Reaction

The catalytic stability during the reaction is one of the indicators for effective catalysts. Figure 3-9 shows the comparison of the Fourier transforms of the k^3 weighted EXAFS spectra in fresh and spent sample Ni-P/SiO$_2$ (Ni:P = 1:1). In all cases, the Fourier transform shows the two distinguish peaks: the main Ni-Ni peak and the Ni-P peak shoulder. The peak pattern remained almost unchanged in fresh and spent samples under the 1173 K reaction conditions. Thus, the EXAFS data suggested that the sample of Ni-P/SiO$_2$ (Ni:P = 1:1) is highly stable during the reductive NOCM reactions at 1173K.
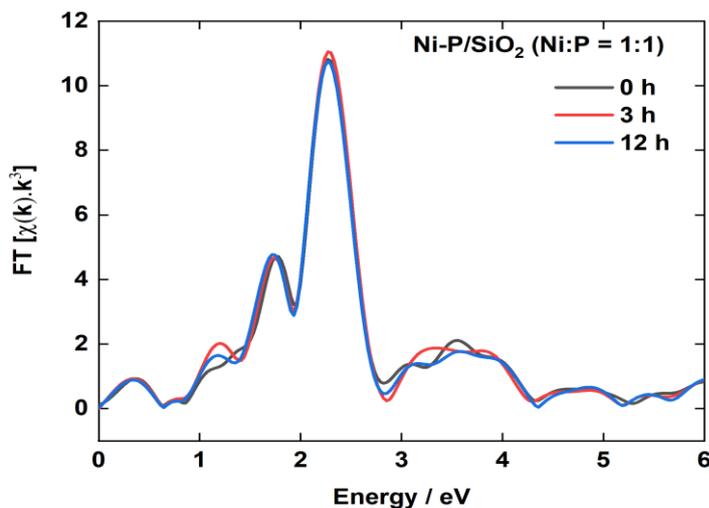
Figure 3-9. Fourier transform of Nickel K-edge EXAFS spectra of the fresh and spent sample of Ni-P/SiO$_2$ (Ni:P = 1:1) with different reaction times: 0 h , 3 h, and 12 h.

3.6. Conclusion

In this chapter, I have analyzed three samples Ni-P/SiO$_2$ with different initial Ni:P ratios of 1:1, 2:1, and 3:1. The structural properties were characterized by extended X-ray absorption fine structure (EXAFS), which showed that Ni-P/SiO$_2$ (Ni:P = 1:1) had a structure of Ni$_2$P. So, the NOCM catalytic activity was high due to the presence of Ni$_2$P phase, and it was stable during non-oxidative coupling of methane (NOCM) reactions at 1173 K. Still, the other two samples were less active in catalytic reaction might be the absence of Ni$_2$P structure. P might control the Ni activity not to from the C-C bond by geometrically or electrically.

71

Reference

1. Dipu, A., Obuchi, S., Nishikawa, Y., Ogihara, H. & Yamanaka, I. Nickel phosphide catalyst for direct dehydrogenative conversion of methane to higher hydrocarbons. in *The 8th Tokyo Conference on Advanced Catalytic Science and Technology (TOCAT8)* P1235, 2018 (2018). https://www.shokubai.org/tocat8/pdf/Poster/P1235.pdf.

2. Dipu, A. L. *et al.* Direct Nonoxidative Conversion of Methane to Higher Hydrocarbons over Silica-Supported Nickel Phosphide Catalyst. *ACS Catal.* **10**, 375–379 (2020).

3. Iwasawa, Y., Asakura, K. & Tada, M. *XAFS Techniques for Catalysts, Nanomaterials, and Surfaces*. (Springer International Publishing. 2017).

4. Day, O., Rehr, J., Zabinsky, S. I. & Brown, G. E. Extended X-ray Absorption Fine Structure (EXAFS) Analysis of Disorder and Multiple-Scattering in Complex Crystalline Solids. 2938–2949 (1994).

5. Asakura, K. Analysis of EXAFS. in (ed. Iwasawa, Y.) **58**, 33–58 (World Scientific, 1996).

6. Oyama, S. T., Gott, T., Zhao, H. & Lee, Y.-K. Transition metal phosphide hydroprocessing catalysts: A review. *Catal. Today* **143**, 94–107 (2009).

7. Rodriguez, J. A., Kim, J.-Y., Hanson, J. C., Sawhill, S. J. & Bussell, M. E. Physical and Chemical Properties of MoP, Ni 2 P, and MoNiP Hydrodesulfurization Catalysts: Time-Resolved X-ray Diffraction, Density Functional, and Hydrodesulfurization Activity Studies. *J. Phys. Chem. B* **107**, 6276–6285 (2003).

8. Iino, A., Takagaki, A., Kikuchi, R., Oyama, S. T. & Bando, K. K. Combined In Situ XAFS and FTIR Study of the Hydrodeoxygenation Reaction of 2-Methyltetrahydrofuran on Ni 2 P/SiO 2. *J. Phys. Chem. C* **123**, 7633–7643 (2019).

9. Moon, J.-S. *et al.* The nature of active sites of Ni 2 P electrocatalyst for hydrogen evolution reaction. *J. Catal.* **326**, 92–99 (2015).

10. Rundqvist, S. *et al.* X-Ray Investigations of Mn3P, Mn2P, and Ni2P. *Acta Chemica Scandinavica* vol. 16 992–998 (1962).

11. Moula, G. *et al.* The First Atomic-scale Observation of a Ni 2 P (0001) Single Crystal Surface. **35**, 90–91 (2006).

12. Hernandez, A. B. *et al.* Dynamical LEED analysis of Ni2P (0 0 0 1)-1 × 1: Evidence for P-covered surface structure. *Chem. Phys. Lett.* **513**, 48–52 (2011).

13. Ariga, H., Kawashima, M., Takakusagi, S. & Asakura, K. Density Function Theoretical Investigation on the Ni 3 PP Structure and the Hydrogen Adsorption Property of the Ni 2 P(0001) Surface. *Chem. Lett.* **42**, 1481–1483 (2013).

14. Taguchi, T., Ozawa, T. & Yashiro, H. REX2000: Yet another XAFS analysis package. *Phys. Scr. T* **T115**, 205–206 (2005).

15. Stern, E. A. Number of relevant independent points in x-ray-absorption fine-structure spectra. *Phys. Rev. B* **48**, 9825–9827 (1993).

16. Rehr, J. J. & Albers, R. C. Theoretical approaches to x-ray absorption fine structure. *Rev. Mod. Phys.* **72**, 621–654 (2000).

17. Hamilton, W. C. Significance tests on the crystallographic R factor. *Acta Crystallogr.* **18**, 502–510 (1965).

Chapter 4

Theoretical XAFS Analysis of Nickel Phosphide Catalysts with Different Initial Ni and P Ratios for NOCM Reactions

4.1. Introduction

X-ray absorption fine structure (XAFS) spectroscopy is a promising technique for studying the local structure of absorbing atoms contained within the material. Especially XAFS is sensitive to the oxidation state, coordination chemistry, bond distances, and species atoms that immediately surround the particular element. For this reason, XAFS is a significant probe of materials, which is important to progress in many scientific fields, whether for biology, chemistry, electronics, geophysics, metallurgy, or materials science.[1] The X-ray absorption spectrum is divided into two regimes: X-ray absorption near edge structure (XANES) and extended X-ray absorption fine structure (EXAFS). XANES region provides us qualitative information that is extremely sensitive to the absorbing atom's oxidation state and coordination chemistry. On the other hand, the EXAFS region provides us quantitative information, which is used to determine the distances, coordination number, and species of the neighbors of the absorbing atom.

An XAFS is a wonderful mixture of modern physics and chemistry. Although the measurement of XAFS is relatively straightforward, the data analysis is somewhat challenging. The existence of third-generation synchrotron radiation sources alone was not enough to achieve qualitative and quantitative information. The full success of the XAFS technique must be attributed in large part to advances in theory, which have a significant contribution to extract the information of the target element. The theoretical techniques have to be improved to keep abreast with the experimental advancement to extract better information from the experimental data. The development of advanced X-ray absorption theory has paralleled with modern synchrotron radiation sources. The basic theory of EXAFS is now well established. The theory of XANES is not yet fully quantitative. It requires different physical considerations. But significant progress has been made in third-generation theories, which include theories of X-ray near edge structure (XANES), i.e., the structure within about 30 eV of threshold where multiple scattering contributions are important. Multiple scattering (MS) theory now provides a uniform treatment of the structure in both EXAFS and XANES. These theoretical

advances have led to the development of ab initio codes for XAS calculations in arbitrary systems, for example, CONTINUUM[2], EXCURVE[3], FEFF[4–6], GNXAS[7], and WIEN98[8], as well as various band-structure codes[9].

In the previous Chapter 3, I have studied SiO_2-supported Ni phosphide catalysts with different Ni:P ratios of 1:1, 2:1, and 3:1 for non-oxidative coupling of methane (NOCM) reaction using the conventional curve fitting method. I have revealed the SiO_2-supported nickel phosphide compound with initial Ni:P = 1:1 showed the Ni_2P structure by extended X-ray absorption fine structure (EXAFS). The nickel phosphide compounds with the other initial Ni:P ratios of 2:1 and 3:1 are less active. It is interesting and important to make the relation between activity and structure to know the reason for fewer activities of initial Ni:P ratios of 2:1 and 3:1 and to design another new type of Ni-P/SiO_2 catalysts. Nickel phosphide has different phases, namely Ni_3P, $Ni_{12}P_5$, Ni_2P, Ni_5P_4, NiP, NiP_2, and NiP_3.[10,11] Those in the Ni-rich phase have very complicated structures with different sites and various Ni-P distances. Therefore, it is not easy to determine the nickel phosphide phase only by the EXAFS CF method. X-ray absorption near-edge structure (XANES) is a powerful technique for investigating the local structure of inorganic-oxide-supported catalysts, which is more sensitive to the electronic states and 3-dimensional geometric structures than EXAFS spectroscopy.[12] I may have determined the Ni phosphide compounds with various compositions by EXAFS and XANES. But the problems were that I did not have the appropriate reference compounds. Thus I carried out XANES and EXAFS calculations based on the model structures using FEFF8. Theoretical XAFS calculations using the FEFF program have enabled us to reproduce the XAFS spectra in both the XANES and EXAFS regions.[13,14] I attempted to analyze the structure of Ni phosphide catalysts by comparing with the theoretical XAFS spectra of reference compounds based on their crystal structures instead of by comparing with experimental XAFS spectra of analyzing compounds. In this chapter, I carried out structural analyses of Ni-P/SiO_2 catalysts with initial Ni:P ratios of 1:1, 2:1, and 3:1 using theoretical FEFF models without experimental reference compounds.

4.2. Theoretical FEFF Model

FEFF8 is a common program for calculating multiple scattering to XAFS (EXAFS and XANES) simulation.[15] It uses muffin-tin like potential approximation for the potential geometry of the crystal lattice. FEFF calculates with Hartree-Fock

self-consistent orbitals to obtained the scattering potentials. A FEFF calculation starts with two basic tasks: calculations of potentials, followed by calculation of the scattering phase shifts. There are two ways to do this: either using an explicit enumeration and summation, most appropriate for extended absorption spectra: or using the implicit summation of full multiple scattering, suitable for near-edge absorption spectra.[15] FEFF8 can be used for several different calculations. In this chapter, I have demonstrated its use for XANES and EXAFS calculations.

4.2.1. Muffin-Tin Potential

The muffin-tin is a shape approximation of the potential field in an atomistic environment. This approximation was proposed by John C. Slater.[16] The basic approximation is the potential assumed to be spherically symmetric in the muffin-tin region and constant in the interstitial region (Figure 4-1).
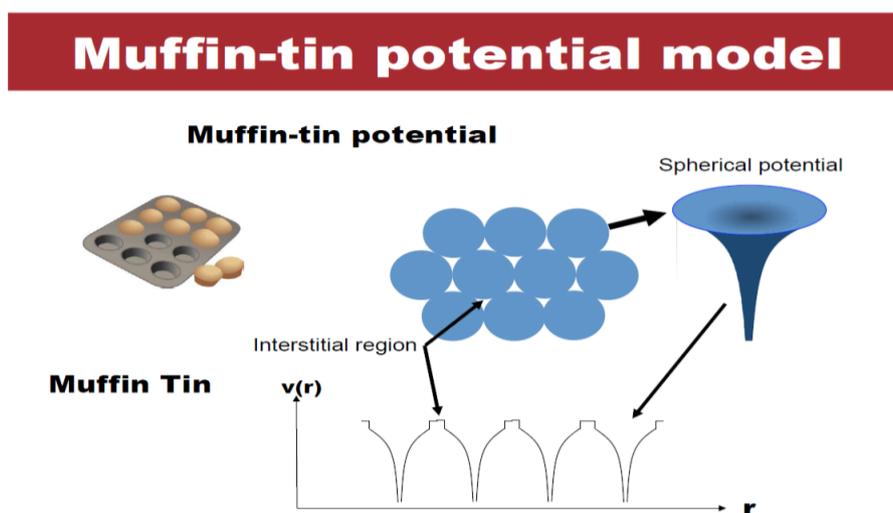
Figure 4-1.   Schematic diagram of spherical muffin-tin approximation. In the muffin-tin potential, the flat potential indicating the interstitial region between atoms.[17]

A tremendous amount of methodical machinery has been built up over the last century that relies on spherical symmetry. The spherical muffin-tin geometry makes it possible to apply this machinery in a very efficient way. In the multiple scattering approach that most directly connects to the underlying atomic structure of a material, the muffin-tin approximation provides atomic scattering centers that are entirely described by phase shifts, which are calculated from spherically symmetric atomic like

potentials inside the muffin-tins. Green's function propagators are employed to connect these scattering centers. Accurate calculations depend on good potentials since they determine the strength of the scattering at each site.[13] In EXAFS spectroscopy, the excited electron is less sensitive to the potential at the outer edges of the atom and in the region between the atom. The electron is mainly scattered by the inner parts of the atomic potential and move more or less freely in the constant potential interstitial region. For this reason, the muffin-tin approximation works well in the EXAFS region, where the details of the shape of interatomic potential are much more important in the XANES region.

4.3. Crystal Structure of Transition Metal Compounds

The main goal of this chapter is the determination of the crystal structure of Ni-P/SiO$_2$ with Ni:P ratios of 1:1, 2:1, and 3:1 using the theoretical FEFF model. Also, I want to make a relation between structure and catalytic activity for NOCM reaction. For this purpose, I need to know the detailed crystal structure of various nickel phosphides. Seven different phases of nickel phosphides have been described in Chapter 1 (Section 1.3). Here the crystal structure information of various nickel phosphides has been shown in Table 4-1.

Table 4-1. Crystal structure information of several nickel phosphides.

Ni$_3$P (Tetragonal)	Geometry	Ni-P Bond distance (Å)
Ni(0)P4	Tetrahedral	2.34 (1)
		2.32 (1)
		2.33 (1)
		2.29 (1)
Ni(1)P2	Water like	2.21(1)
		2.26(1)
Ni(2)P3	Distorted trigonal	2.21(1)
		2.27(1)
		2.32(1)

Ni$_{12}$P$_5$ (Tetragonal)	Geometry	Ni-P Bond distance (Å)
Ni(0)P4	Tetrahedral	2.21 (1)
		2.23 (1)
		2.41 (1)
		2.45 (1)
Ni(1)P2	See-Saw like	2.23 (2)
		2.58 (2)

Ni$_2$P (Hexagonal)	Geometry	Ni-P Bond distance (Å)
NiP5	Trigonal Bipyramidal	2.37 (1)
		2.46 (4)
NiP4	Tetrahedral	2.21(2)
		2.27(2)

Ni$_5$P$_4$ (Hexagonal)	Geometry	Ni-P Bond distance (Å)
NiP5	trigonal bipyramids	2.29–2.46
NiP4	trigonal pyramids	2.16 Å (3)
		2.19 Å (1)
NiP4	distorted tetrahedra	2.27–2.46
NiP5	distorted trigonal bipyramids	2.28–2.41

NiP (Orthomobic)	Geometry	Ni-P Bond distance(Å)
Ni(0)P5	5-coordinate geometry	2.25 (1)
		2.27 (1)
		2.28 (1)
		2.31 (1)
		2.33 (1)

NiP$_2$ (Monoclinic)	Geometry	Ni-P Bond distance(Å)
NiP4	square co-planar	2.28 (6)

NiP$_3$ (Cubic)	Geometry	Ni-P Bond distance(Å)
NiP6	octahedra	2.28 (6)

4.4. Theoretical Data Calculations Using FEFF

The FEFF program carries out various tasks to generate the theoretical signals to be used at the fitting stage. The main actions in a run for XANES and EXAFS analysis are listed below:

- Calculations of atomic potentials in the muffin-tin approximation from a given cluster

- Calculate the phase shifts.

- Analysis of the cluster with identification of the multiple scattering paths.

- Calculate the signals.

A series of modules sequently do all these operations.

An example of input file "feff.inp" of Ni_2P for XANES and EXAFS calculations has been below: Input file for XANES calculations

```
*feff - Notepad
File  Edit  Format  View  Help
* This feff8 file was generated by Demeter 0.9.26
* Demeter written by and copyright (c) Bruce Ravel, 2006-2019


*  Ni K edge energy = 8333 eV
EDGE      K
*S02      1.0

*         pot   xsph  fms   paths genfmt ff2chi
CONTROL   1     1     1     1     1      1
PRINT     1     0     0     0     0      3

*         ixc  [ Vr  Vi ]    *** ixc=0 means to use Hedin-Lundqvist
EXCHANGE  0
                             *** Radius for self-consistent pots (2 shells is a good choice)
*         r_scf [ l_scf   n_scf    ca ]   *** l_scf = 0 for a solid, 1 for a molecule
SCF       5.0      0       81      0.2

*         kmax  [ delta_k  delta_e ]    *** Upper limit of XANES calculation.
 XANES    5.0       0.07     0.0

*         r_fms      l_fms     *** Radius for Full Mult. Scatt. l_fms = 0 for a solid, 1 for a molecule
 FMS      6.0        0


POTENTIALS
*   ipot   Z   element      l_scmt  l_fms   stoichiometry
    0      28     Ni          2       2        0.001
    1      15     P           2       2        1
    2      28     Ni          2       2        2


ATOMS                  * this list contains 83 atoms
*   x          y          z     ipot tag          distance
   0.00000    0.00000    0.00000  0  Ni1           0.00000
  -2.07613    0.75454    0.00000  1  P1.1          2.20899
  -0.38461   -2.17525    0.00000  1  P1.1          2.20899
   1.30657    0.75435    1.69100  1  P2.1          2.26619
   1.30657    0.75435   -1.69100  1  P2.1          2.26619
  -1.71604   -0.99076    1.69100  2  Ni2.1         2.60497
  -1.71604   -0.99076   -1.69100  2  Ni2.1         2.60497
```

(follows the positions of the atoms up to the 6 Å)

END

Input file for EXAFS calculations:

```
File  Edit  Format  View  Help
* This feff8 file was generated by Demeter 0.9.26
* Demeter written by and copyright (c) Bruce Ravel, 2006-2019


*  Ni K edge energy = 8333 eV
EDGE      K
S02       0.8

*         pot   xsph  fms   paths genfmt ff2chi
CONTROL   0     0     0     0     0      1
PRINT     1     0     0     0     0      3

*         ixc [ Vr  Vi ]     *** ixc=0 means to use Hedin-Lundqvist
EXCHANGE  0       10  4

                                *** Radius for self-consistent pots (2 shells is a good choice)
*         r_scf  [ l_scf   n_scf   ca ]   *** l_scf = 0 for a solid, 1 for a molecule
SCF       5.0

*         kmax   [ delta_k  delta_e ]    *** Upper limit of XANES calculation.
* XANES    4.0

*         r_fms     l_fms      *** Radius for Full Mult. Scatt. l_fms = 0 for a solid, 1 for a molecule
* FMS     10.70454  0

*         emin  emax   eimag  *** Energy grid over which to calculate DOS functions
* LDOS    -30   20     0.1

            *** for EXAFS: RPATH 5.0 and uncomment the EXAFS card
RPATH     3.0
EXAFS     12
 * POLARIZATION  0   0   0

POTENTIALS
*   ipot   Z  element      l_scmt  l_fms   stoichiometry
    0     28    Ni            2      2       0.001
    1     28    Ni            2      2       3
    2     28    Ni            2      2       3
    3     15    P             2      2       2
    4     15    P             2      2       1

SIG2 0.009

ATOMS               * this list contains 43 atoms
*    x         y          z     ipot tag          distance
   0.00000    0.00000    0.00000  0  Ni0          0.00000
  -2.06983    0.76257    0.00000  3  P2.1         2.20583
  -0.37450   -2.17381    0.00000  3  P2.1         2.20583
   1.32081    0.76257    1.67467  4  P3.1         2.26507
   1.32081    0.76257   -1.67467  4  P3.1         2.26507
  -1.73535   -1.00190    1.67467  2  Ni1.1        2.61147
  -1.73535   -1.00190   -1.67467  2  Ni1.1        2.61147
   2.64163    0.00000    0.00000  1  Ni0.1        2.64163
   1.32081    2.28771    0.00000  1  Ni0.1        2.64163
```

(follows the positions of the atoms up to the 6 Å)

END

4.4.1. Modules

The calculation proceeds as follows: First, the program is instructed that a K-edge spectrum has to be calculated (EDGE card). Then various modules of the program are marked to be run (1) or not (0) in sequence (CONTROL card) performing the following operations:

pot: Calculates the (atomic, muffin-tin) scattering potentials

xsph: Calculates the phase shift

fms: Full multiple scattering calculations of the absorption cross-section

paths: path identification

genfmt: Scattering amplitude calculation

ff2ci: Output of the various theoretical paths on a file

4.4.2. Cards

Two input cards, POTENTIALS, and ATOMS are strictly necessary. The card EXCHANGE defines the energy-dependent potential type to be used, ixc=0 corresponding to the complex Hedin-Lunquvist potential. Cards like SCF, XANES, FMS, LDOS are needed only for XANES simulations. An EXAFS analysis will be commented on with a " * " character. For the EXAFS simulations, the card EXAFS and RPATH are necessary. The output χ can be found in the file "chi.dat". The important card has been described below[15]:

ATOMS: ATOMS specifies the absorbing atom and its environment. Alternatively, if atomic coordinates are not known, the OVERLAP card can be used to construct approximate potentials. Without the structural information of either ATOMS or the OVERLAP card, no calculations can be done.

POTENTIALS: The potentials card is followed by a list that assigns a unique potentials index to each distinguishable atom. The potentials index ipot is the index of the potential to the user for the phase shift calculations.

SCF: This card controls FEFF's automated self-consistent potential calculations. All fields except rfms1 are potential. If this card is not specified, then all calculations are done with non-self-consistent potentials.

FMS: Compute full multiple scattering within a sphere of radios rfms centered on the absorbing atom (real space) or for the unit cell of the crystal (k-space).

RPATH: The RPATH card determines the maximum effective (half-path) distance, rpath, of a given path. Typically RPATH is needed for EXAFS calculations.

EXAFS: EXAFS is the default type of spectroscopy. The EXAFS card sets the maximum value of k for EXAFS calculations. k is set by k_{max}, and the default value is 20Å^{-1}.

XANES: The XANES card is used when a calculation of the near edge structure, including the atomic background and absolute energies, is desired. The XANES card is generally accompanied by the FMS card for accurate results.

4.5. Results and Discussion

Figure 4-2 shows the comparison of Ni K-edge XANES, inversely Fourier Transform (IFT) and Fourier transform (FT) of the Ni_2P reference sample with the FEFF8 calculated theoretical spectra. The experimental and theoretical XANES spectra of Ni_2P show the same three features (labeled A, B, and C). To estimate the systematic error, I compared the peak positions in the experimental and calculated Ni_2P spectra. The differences between the experimental and calculated peak energies were 0.0, −0.4, and 0.0 eV for features A, B, and C, respectively (Table 4-2).

Table 4-2. Experimental and theoretical peak positions in XANES spectra of Ni_2P.

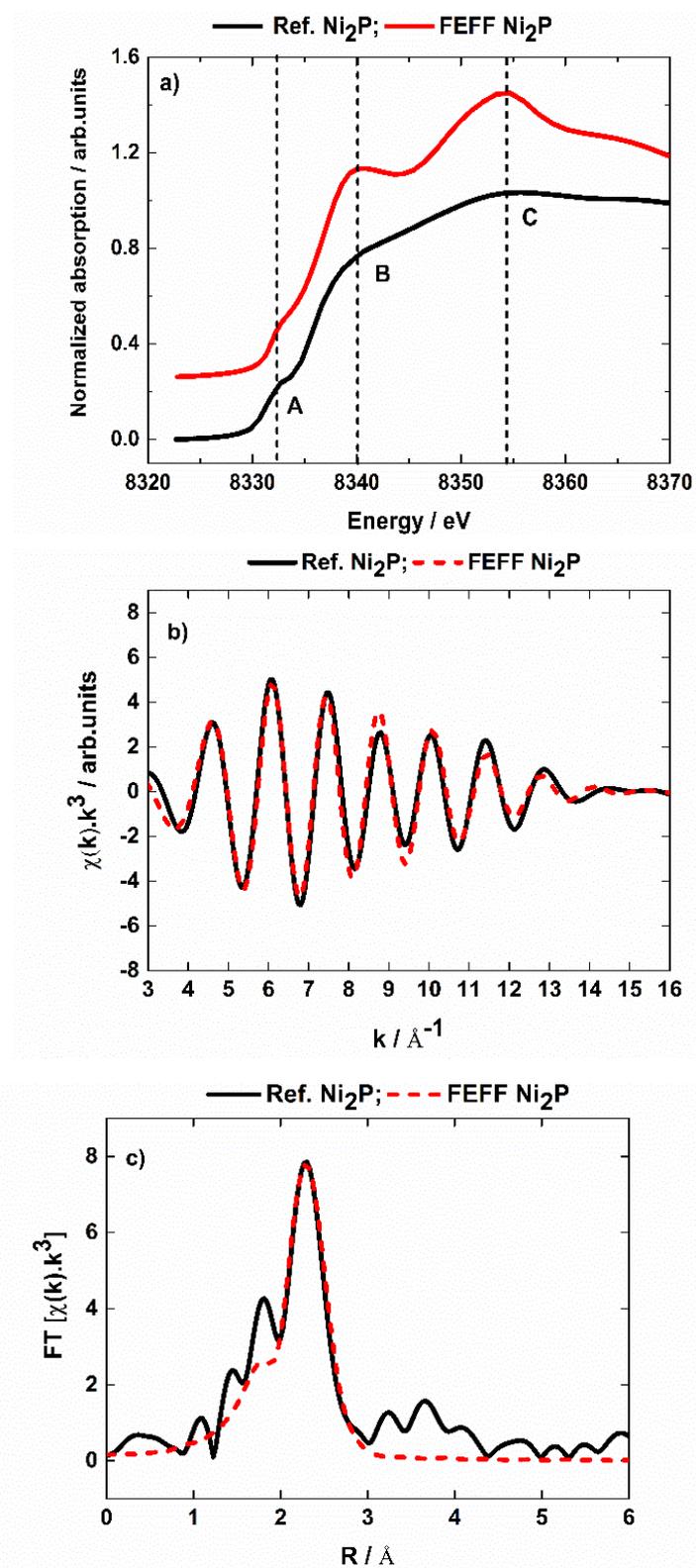| Ref. Ni_2P (eV)	FEFF8 Ni_2P (eV)	ΔE (eV)
8332.7	8332.7	0.0
8339.7	8340.1	−0.4
8354.7	8354.7	0.0

Figure 4-2. a) Comparison of experimental and theoretical Ni K-edge XANES spectra of Ni₂P; b) comparison of experimental (solid line) and theoretical Ni K-edge EXAFS (red broken line) spectra of Ni₂P; c) corresponding Fourier transform.

Thus, the experimental and calculated peak positions coincide with each other within ±0.4 eV. Peaks B and C were broadened in the experimental XANES spectrum. Since FMS strongly affects XANES spectra, I observed FEFF calculated XANES spectra with two different FMS radios 3Å and 5Å (Figure 4-3). Our observation of peak broadening with a smaller FMS radius in the FEFF calculation suggests that the broadening may arise from the shorter coherence length of photoelectrons in the Ni_2P crystal. Notably, however, the peak position was independent of the FMS radius. Thus, I herein concentrate mainly on the peak positions in the comparison of the experimental and calculated data.
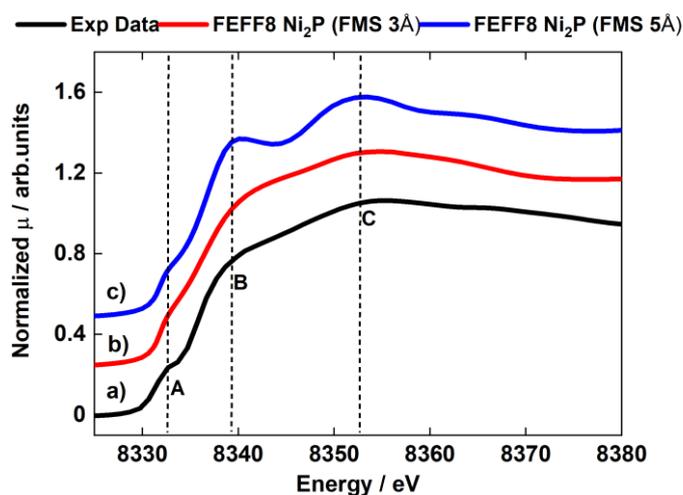
Figure 4-3. Comparison of Ni K-edge experimental and theoretical XANES spectra: a) Ni_2P (black line), b) Ni_2P FEFF (cluster size 3Å) (red line), and c) Ni_2P FEFF (cluster size 5Å) (blue line).

I also used the FEFF8 program to carry out an EXAFS simulation based on the Ni_2P crystal structure. The simulation well reproduced the experimental data for Ni_2P (Figure 4-2). This approach differs from the CF method in that the simulated EXAFS spectrum was calculated on the basis of the coordinates of all atoms (Ni and P) without any adjustable parameters except the amplitude reduction factor (S_0^2) and the Debye-Waller factors (σ^2), which had been optimized. By contrast, in the CF analysis, eight parameters were optimized [coordination number (CN), bond distance (R), Debye-Waller factor (σ^2), and edge-shift (ΔE) for both Ni–Ni, and Ni–P bonds]. Although the CF analysis gave much better fitting results, the obtained parameters were not directly related to the real structure. The FEFF simulation approach based on the crystal structure enabled us to elucidate the catalyst structures, although the goodness of

fit was slightly worse. I attempted to predict the structures of Ni-P/SiO$_2$ with different Ni:P ratios in a similar manner.

4.5.1. XANES Analysis

Figure 4-4 shows XANES spectra of Ni-P/SiO$_2$ with Ni:P ratios of 1:1, 2:1, and 3:1; the spectra show three different peaks (denoted A, B, and C) at different energy positions for Ni-P/SiO$_2$ (Ni:P = 1:1) and (Ni:P = 3:1). By contrast, the Ni-P/SiO$_2$ (Ni:P = 2:1) spectrum shows four peaks (A, B, C, and D).
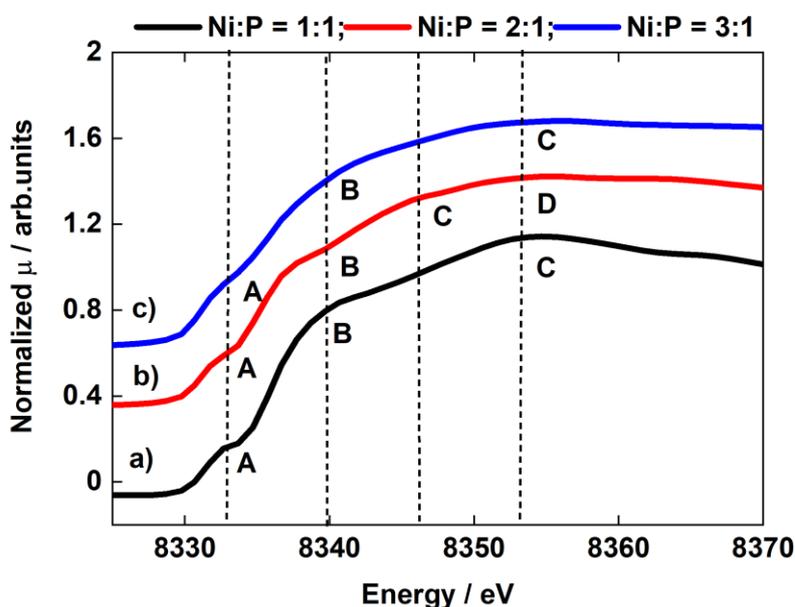
Figure 4-4. Comparison of Ni K-edge experimental XANES spectra of Ni-P/SiO$_2$: a) Ni:P = 1:1 (black line), b) Ni:P = 2:1 (red line), and c) Ni:P = 3:1 (blue line).

For XANES calculations in FEFF8, the self-consistent potential (SCF) and Full multiple scattering (FMS) must be specified to run the theoretical calculations. In this thesis, for theoretical XANES spectra calculations of seven different nickel phosphide (Ni-P), self-consistent potentials with a cluster radius of 5Å and Full multiple scattering (FMS) cluster size 5Å was used. Figure 4-5 shows the FEFF-calculated theoretical XANES spectra of NiP$_3$, NiP$_2$, NiP, Ni$_5$P$_4$, Ni$_2$P, Ni$_{12}$P$_5$, and Ni$_3$P. For the peak positions comparison of experimental and theoretical XANES spectra, I extracted peak positions in XANES spectra. Figure 4-6 shows details of the peak energies for all of the experimental and theoretical Ni K-edge XANES spectra. The calculated XANES

spectra for different Ni phosphides show three peaks, whereas the NiP_2 and $Ni_{12}P_5$ spectra show four peaks.
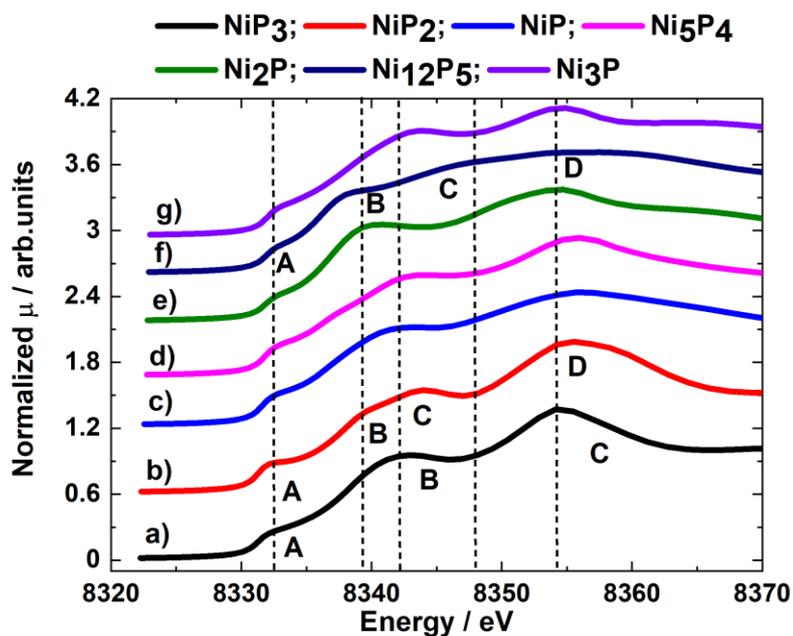
Figure 4-5. Comparison of Ni K-edge theoretical XANES spectra of reference compounds: a) FEFF NiP_3 (black line), b) FEFF NiP_2 (red line), c) FEFF NiP (blue line), d) FEFF Ni_2P (pink line), e) FEFF Ni_5P_4 (green line), f) FEFF $Ni_{12}P_5$ (navy line), and g) FEFF Ni_3P (violet line).
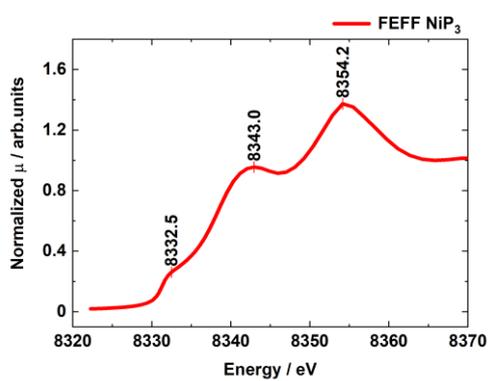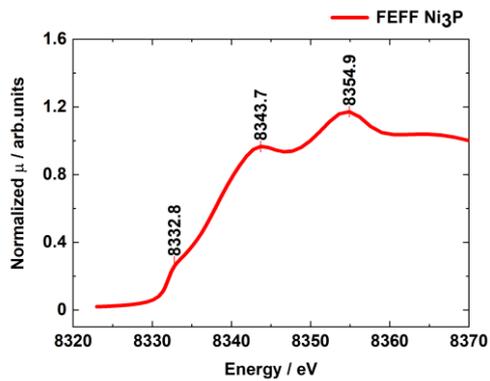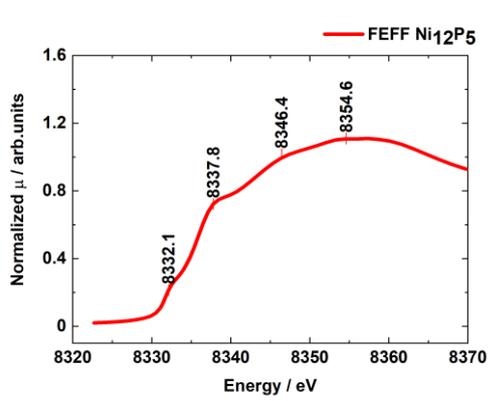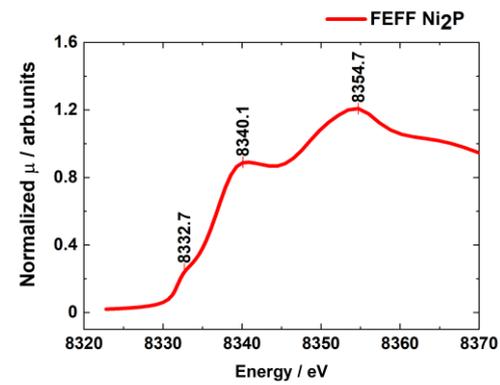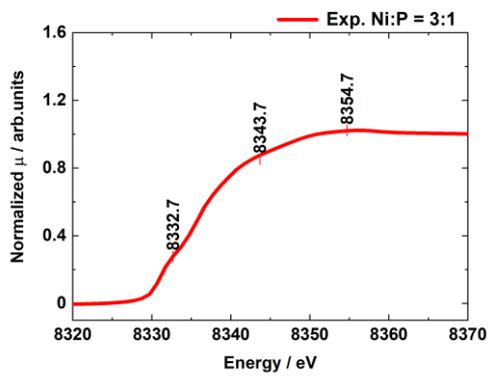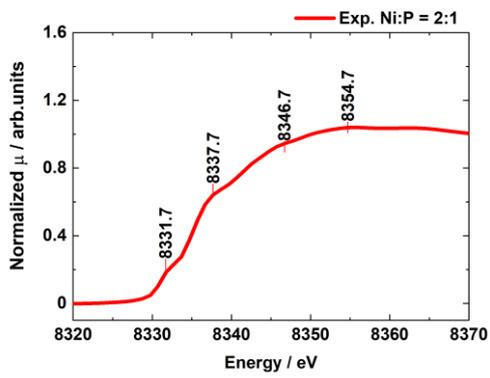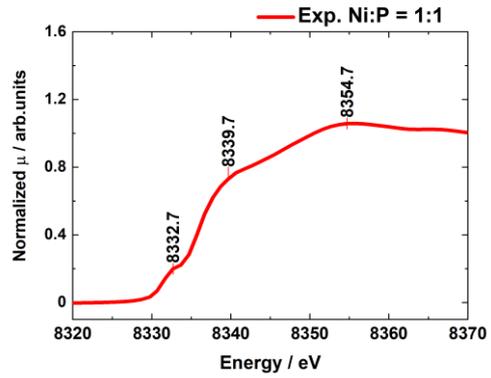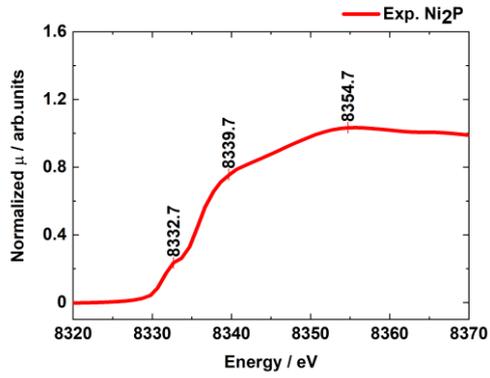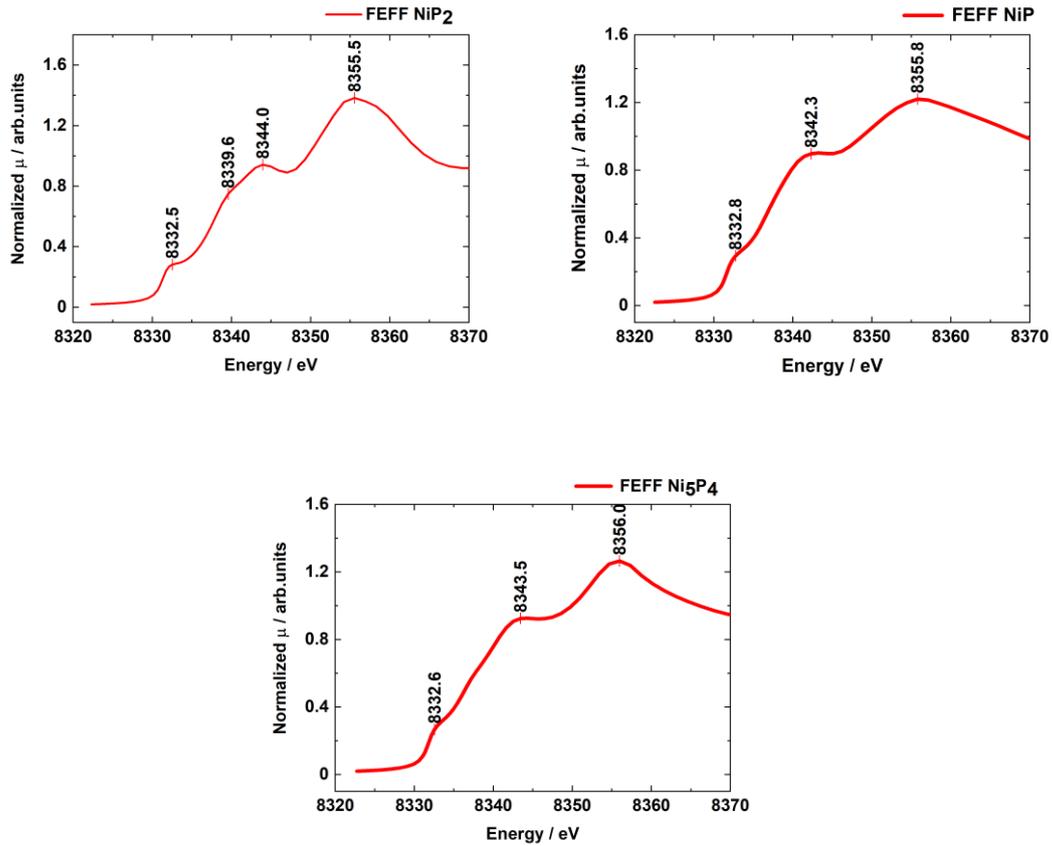
Figure 4-6. Peak Position of Ni K-edge XANES spectra of Ref. Ni_2P, experimental samples Ni-P/SiO$_2$: Ni:P = 1:1, Ni:P = 2:1, Ni:P = 3:1, and theoretical Ni K-edge XANES spectra of Ni_2P, $Ni_{12}P_5$, Ni_3P, NiP_3, NiP_2, NiP, and Ni_5P_4 respectively.

Figure 4-7 shows the Ni K-edge XANES spectrum of Ni-P/SiO$_2$ (Ni:P = 1:1), together with those of Ni$_2$P, NiP$_2$, and NiP calculated using FEFF8. The experimental XANES spectrum of Ni-P/SiO$_2$ (Ni:P = 1:1) shows three main peaks (A, B, and C). The Ni K-edge peak pattern in the theoretical XANES spectrum of the reference Ni$_2$P compound agrees with the experimental spectrum of Ni- P/SiO$_2$ (Ni:P = 1:1). Peaks A, B, and C in their theoretical XANES spectrum appeared at positions corresponding to Ni-P/SiO$_2$ (Ni:P = 1:1): 8332.7, 8339.7, and 8354.7 eV (Table 4-3).
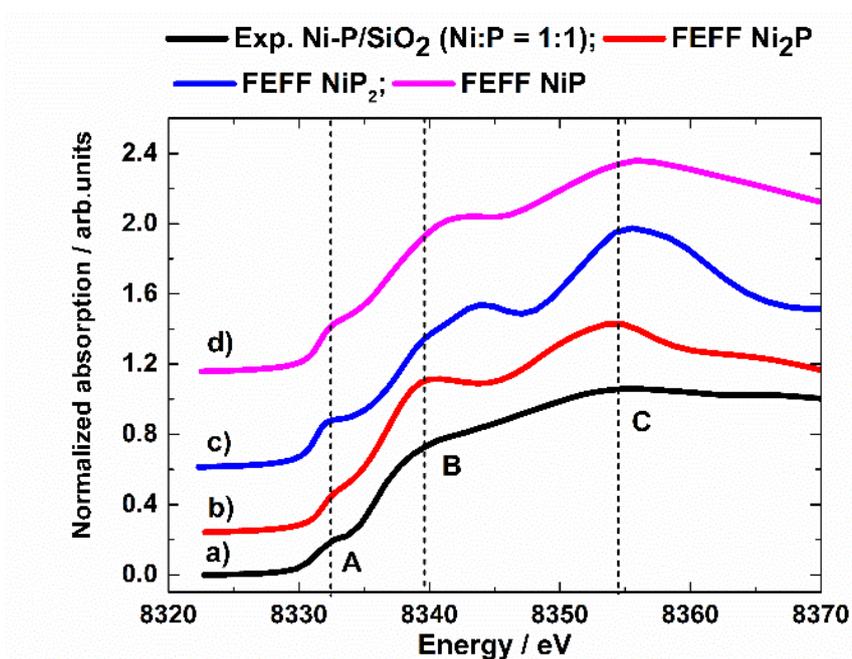
Figure 4-7. Comparison of Ni K-edge XANES spectra for a) Ni-P/SiO$_2$ (Ni:P = 1:1) (black), b) FEFF Ni$_2$P (red), c) FEFF NiP$_2$ (blue), and d) FEFF NiP (pink).

The theoretical XANES spectra of the other reference compounds show peaks at different positions, as summarized in Table 4-3. These results suggest that Ni-P/SiO$_2$ (Ni:P = 1:1) predominantly had the Ni$_2$P structure. These results agreed with our previous CF results (Chapter 3).

Table 4-3. Peak positions of theoretical and experimental XANES spectra of different nickel phosphides with experimental Sample Ni-P/SiO$_2$ (Ni:P = 1:1).

| Exp Ni:P = 1:1 (eV)	FEFF8 Ni$_2$P (eV)	ΔE (eV)
8332.7	8332.7	0.0
8339.7	8340.1	-0.4
8354.7	8354.7	0.0
Exp Ni:P = 1:1 (eV)	**FEFF8 NiP$_2$**	**ΔE (eV)**
8332.7	8332.5	0.2
8339.7	8339.6	0.1
8354.7	8344.0	10.7
Exp Ni:P = 1:1 (eV)	**FEFF8 NiP**	**ΔE (eV)**
8332.7	8332.8	-0.1
8339.7	8342.3	-2.6
8354.7	8355.8	-1.1
Exp Ni:P = 1:1 (eV)	**FEFF8 Ni$_5$P$_4$**	**ΔE (eV)**
8332.7	8332.6	0.1
8339.7	8343.5	-3.8
8354.7	8356.0	-1.3
Exp Ni:P = 1:1 (eV)	**FEFF8 NiP$_3$**	**ΔE (eV)**
8332.7	8332.5	0.2
8339.7	8343.0	-3.3
8354.7	8354.2	0.5
Exp Ni:P = 1:1 (eV)	**FEFF8 Ni$_{12}$P$_5$**	**ΔE (eV)**
8332.7	8332.1	0.6
8339.7	8337.8	1.9
8354.7	8354.8	0.1
Exp Ni:P = 1:1 (eV)	**FEFF8 Ni$_3$P**	**ΔE (eV)**
8332.7	8332.8	-0.1
8339.7	8343.7	-4.0
8354.7	8354.9	-0.2

* Peak position estimated error ±0.4.

Figure 4-8 shows a comparison of the experimental and theoretical XANES spectra of Ni-P/SiO$_2$ (Ni:P = 2:1). Four peaks (A, B, C, and D) appear in the spectra. The experimental spectrum agrees well with the theoretical Ni K-edge XANES spectrum of Ni$_{12}$P$_5$ (Table 4-4). For this composition, the energy differences between the experimental and theoretical peak positions are all within ±0.4 eV. The theoretical XANES spectra for other compositions show larger deviations in peak positions from the experimental spectrum. Consequently, I concluded that the experimental spectrum was consistent with the phase Ni$_{12}$P$_5$.
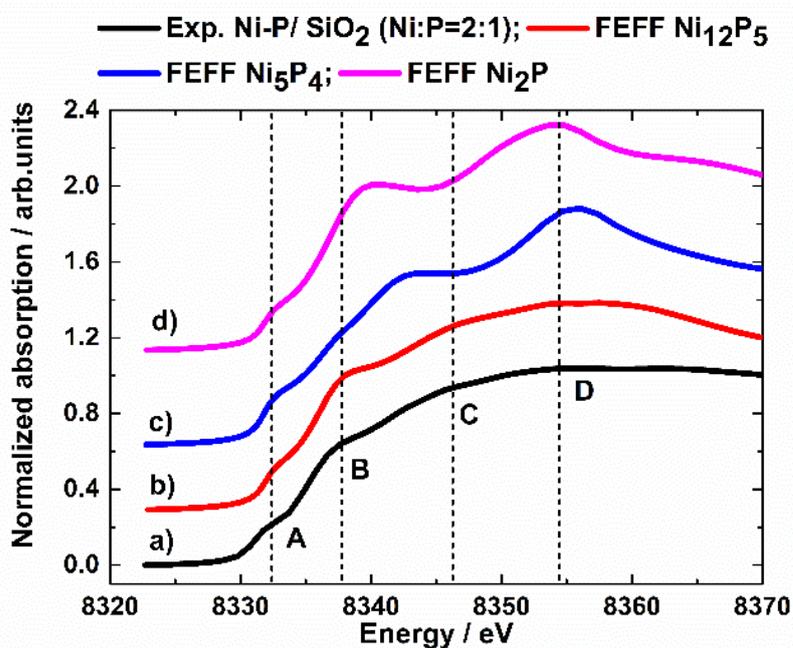
Figure 4-8. Comparison of Ni K-edge XANES spectra: a) Ni-P/SiO$_2$ (Ni:P = 2:1) (black line), b) FEFF Ni$_{12}$P$_5$ (red line), c) FEFF Ni$_5$P$_4$ (blue line), and d) FEFF Ni$_2$P (pink line).

Table 4-4. Peak positions of theoretical and experimental XANES spectra of different nickel phosphides with experimental Sample Ni-P/SiO$_2$ (Ni:P = 2:1).

Exp Ni:P = 2:1 (eV)	FEFF8 Ni$_{12}$P$_5$ (eV)	ΔE (eV)
8331.7	8332.1	-0.4
8337.7	8337.8	-0.1
8346.7	8346.4	0.3
8354.7	8354.6	0.1
Exp Ni:P = 2:1 (eV)	**FEFF8 Ni$_5$P$_4$ (eV)**	**ΔE (eV)**
8331.7	8332.6	-0.9
8337.7	8343.5	-5.8
8346.7	-	-
8354.7	8356.0	-1.3
Exp Ni:P = 2:1 (eV)	**FEFF8 Ni$_2$P (eV)**	**ΔE (eV)**
8331.7	8332.7	-1.0
8337.7	8340.1	-2.4
8346.7	-	-
8354.7	8354.7	0.0
Exp Ni:P = 2:1 (eV)	**FEFF8 Ni$_3$P (eV)**	**ΔE (eV)**
8331.7	8332.8	-1.1
8337.7	8343.7	-6.0
8346.7	-	-
8354.7	8354.9	-0.2
Exp Ni:P = 2:1 (eV)	**FEFF8 NiP$_2$ (eV)**	**ΔE (eV)**
8331.7	8332.5	-0.8
8337.7	8339.6	-1.9
8346.7	8344.0	2.7
8354.7	8355.5	-0.8
Exp Ni:P = 2:1 (eV)	**FEFF8 NiP**	**ΔE (eV)**
8331.7	8332.8	-1.1
8337.7	8342.3	-4.6
8346.7	-	-
8354.7	8355.8	-1.1
Exp Ni:P = 2:1 (eV)	**FEFF8 NiP$_3$**	**ΔE (eV)**
8331.7	8332.5	-0.8
8337.7	8343.0	-5.3
8346.7	-	-
8354.7	8354.2	0.5

* Peak position estimated error ±0.4.

Figure 4-9 shows a comparison of the experimental XANES spectrum of Ni-P/SiO$_2$ (Ni:P = 3:1) and the calculated spectra of three Ni-rich reference compounds. I observed three peaks (A, B, and C) in the spectrum of Ni-P/SiO$_2$ (Ni:P = 3:1). The peak positions in the spectra of the three reference compounds corresponded well with the peak positions in the theoretical Ni$_3$P spectrum (Figure 4-9 and Table 4-5).
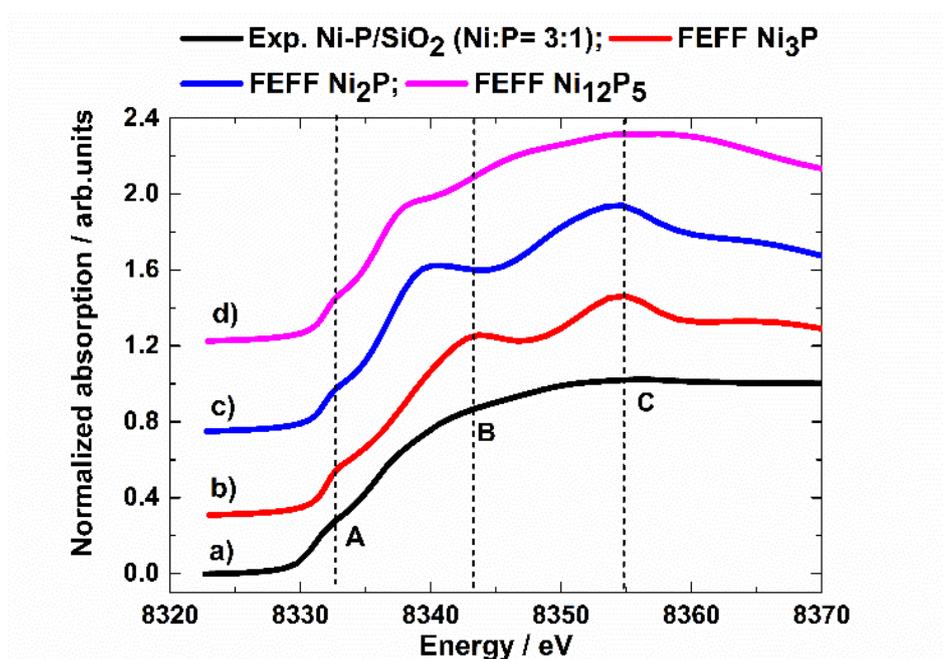

Figure 4-9. Comparison of Ni K-edge XANES spectra: a) Ni-P/SiO$_2$ (Ni:P = 3:1) (black line), b) Ni$_3$P FEFF (red line), c) Ni$_2$P FEFF (blue line), and d) Ni$_{12}$P$_5$ FEFF (pink line).

Table 4-5. Peak positions of theoretical and experimental XANES spectra of different nickel phosphides with experimental Sample Ni-P/SiO$_2$ (Ni:P = 3:1).

Exp Ni:P = 3:1 (eV)	FEFF8 Ni$_3$P (eV)	ΔE (eV)
8332.7	8332.8	-0.1
8343.7	8343.7	0.0
8354.7	8354.9	-0.2
Exp Ni:P = 3:1 (eV)	**FEFF8 Ni$_2$P (eV)**	**ΔE (eV)**
8332.7	8332.7	0.0
8343.7	8340.1	3.6
8354.7	8354.7	0.0
Exp Ni:P = 3:1 (eV)	**FEFF8 Ni$_{12}$P$_5$ (eV)**	**ΔE (eV)**
8332.7	8332.1	0.6
8343.7	8337.8	5.9
8354.7	8354.6	0.1
Exp Ni:P = 3:1 (eV)	**FEFF8 NiP$_2$**	**ΔE (eV)**
8332.7	8332.5	0.2
8343.7	8339.6	4.1
8354.7	8344.0	10.7
Exp Ni:P = 3:1 (eV)	**FEFF8 NiP**	**ΔE (eV)**
8332.7	8332.8	-0.1
8343.7	8342.3	1.4
8354.7	8355.8	-1.1
Exp Ni:P = 3:1 (eV)	**FEFF8 Ni$_5$P$_4$**	**ΔE (eV)**
8332.7	8332.6	0.1
8343.7	8343.5	0.2
8354.7	8356.0	-1.3
Exp Ni:P = 3:1 (eV)	**FEFF8 NiP$_3$**	**ΔE (eV)**
8332.7	8332.5	0.2
8343.7	8343.0	0.7
8354.7	8354.2	0.5

* Peak position estimated error ±0.4.

4.5.2. EXAFS Analysis

For the FEFF8 calculated EXAFS spectra, the calculation of potentials and phase shifts has been done only once. The generated paths using FEFF8 for the Ni$_2$P are shown in Table 4-6. The EXAFS spectrum has been obtained as the sum of these paths. The theoretical EXAFS spectra have been compared with experimental EXAFS spectra to confirm Ni phosphide structure with different Ni:P ratios.

Table 4-6. The path generated by FEFF8

```
list - Notepad
File  Edit  Format  View  Help
PATH  Rmax= 3.000,  Keep_limit= 0.00, Heap_limit 0.00  Pwcrit= 2.50%
----------------------------------------------------------------
  pathindex    sig2     amp ratio    deg    nlegs   r effective
       1      0.00000    100.000    2.000     2      2.2058
       2      0.00000     94.013    2.000     2      2.2651
       3      0.00200     55.260    2.000     2      2.6115
       4      0.00200     55.600    2.000     2      2.6416
       5      0.00200    105.411    4.000     2      2.6551
```

I calculated the EXAFS oscillation based on the Ni_2P crystal structure and compared the spectrum with that of the Ni-P/SiO$_2$ (Ni:P = 1:1) catalyst in k- and R-spaces without optimization as shown in Figures 4-10. I found good agreement between the experimental and calculated spectra. In this analysis, I used an S_0^2 of 0.9 and σ^2 values of 0.009 and 0.0095 Å^2 for Ni–P and Ni–Ni bonds, respectively. By theoretical approaches, I concluded that the Ni-P/SiO$_2$ (Ni:P = 1:1) consisted mainly of the Ni_2P structure, consistent with XANES analysis. I applied the same methods to the other Ni phosphide catalysts.

Figure 4-10. a) Comparison between theoretical Ni_2P (red broken line) and experimental EXAFS spectra of Ni-P/SiO$_2$ (Ni:P = 1:1) (black line); (b) corresponding Fourier transform.

Figure 4-11 compares the experimental EXAFS spectrum of Ni-P/SiO$_2$ (Ni:P = 2:1) with the theoretical spectrum of Ni$_{12}$P$_5$, along with the corresponding FTs. The Fourier peak positions correspond well with each other. The S_0^2 factors for Ni–P and Ni–Ni were both fixed at 0.9, and the σ^2 factors were fixed at 0.007 and 0.0075 Å^2, respectively.
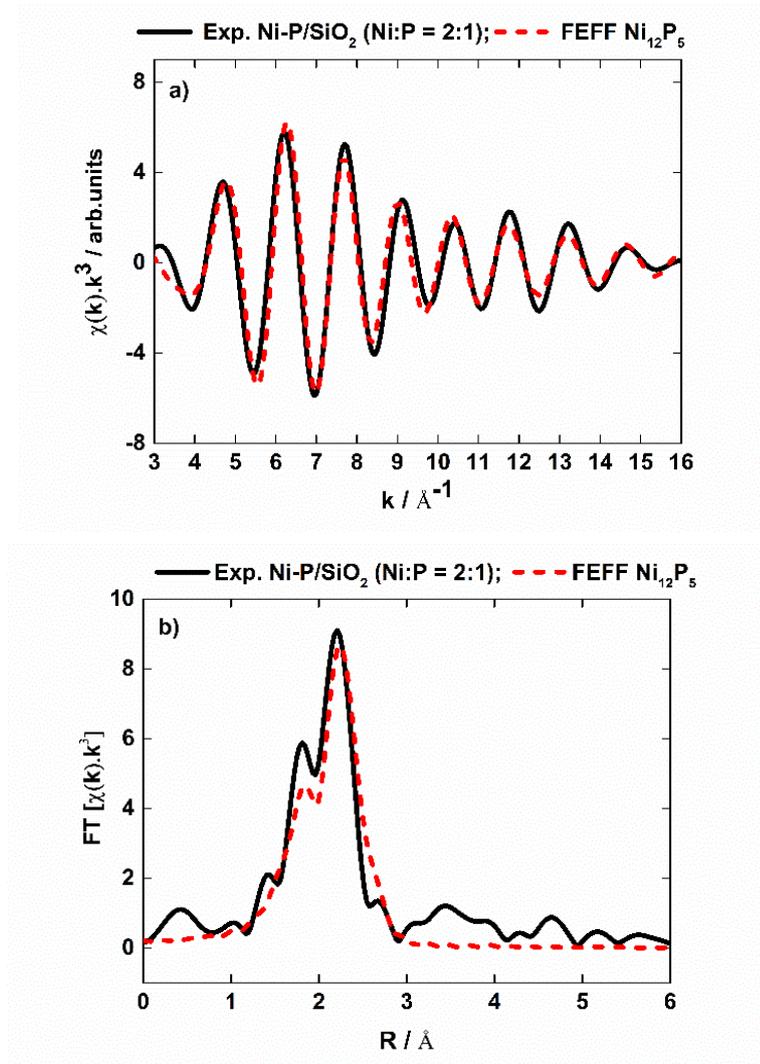
Figure 4-11. a) Comparison between theoretical Ni$_{12}$P$_5$ (red broken line) and experimental Ni-P/SiO$_2$ (Ni:P = 2:1) (black line) EXAFS spectra, and b) corresponding Fourier transform.

I simulated theoretical EXAFS spectra on the basis of the Ni$_3$P crystal structure. The S_0^2 and σ^2 values for Ni–P and Ni–Ni were set at 0.9 and 0.009 Å^2, respectively. Figure 4-12 shows the theoretical EXAFS spectra for the Ni$_3$P structure, the experimental EXAFS spectra for Ni-P/SiO$_2$ (Ni:P = 3:1), and their corresponding FTs. I found that the

calculated EXAFS data successfully reproduced the experimental data. In particular, I observed a single peak in the FT of the Ni-P/SiO$_2$ (Ni:P = 3:1) spectrum and the Ni$_3$P spectrum. Thus, I confirmed the formation of the Ni$_3$P phase in Ni-P/SiO$_2$ catalysts with an initial Ni:P ratio of 3:1.
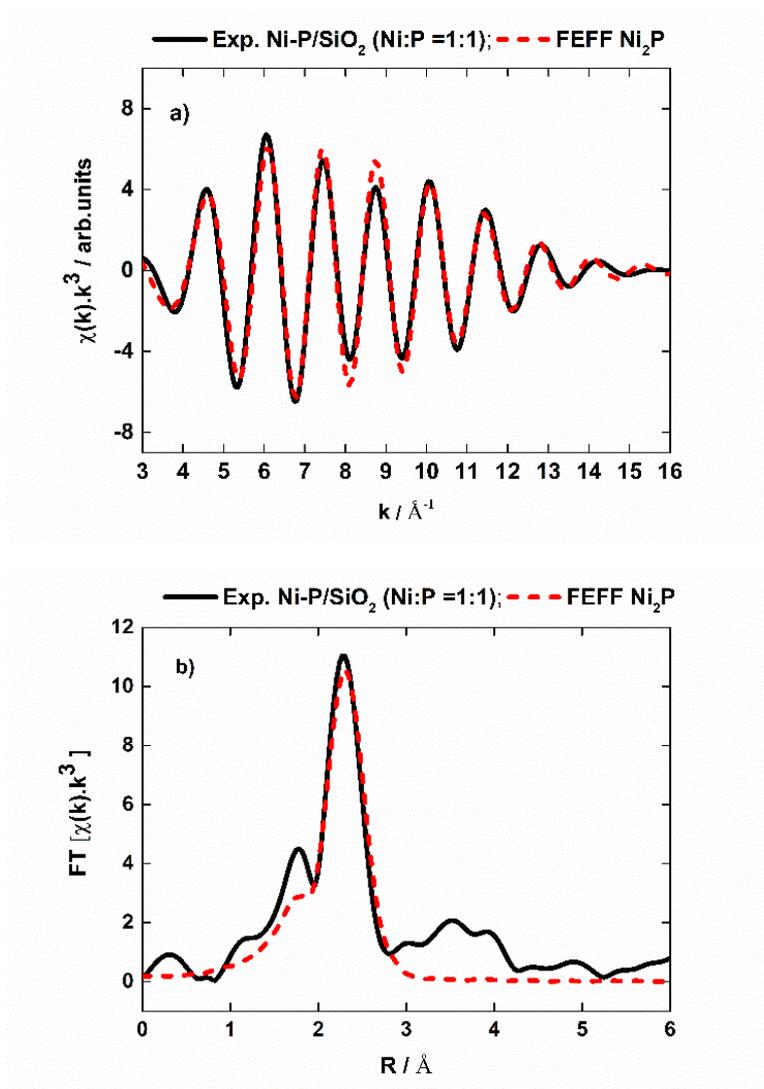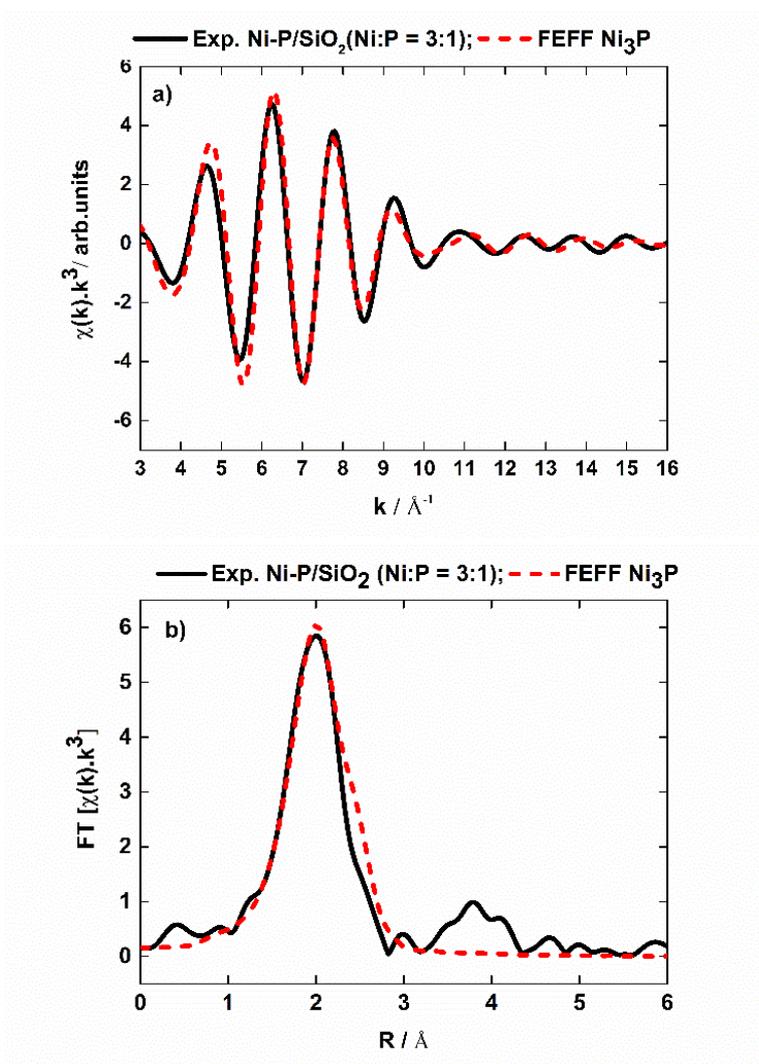

Figure 4-12. a) Comparison between theoretical Ni$_3$P (red broken line) and experimental (black line) EXAFS spectra of Ni-P/SiO$_2$ (Ni:P = 3:1) (black line); b) corresponding Fourier transforms.

4.6. Structure and Catalytic Activity Relationship

Ni phosphides crystalline show a wide range of electronic, magnetic, optical, and catalytic properties. Metal-rich Ni_3P catalysts are known to exhibit high selectivity for the hydrogenation of dimethyl oxalate to methyl glycolate.[18] The P-rich catalyst NiP_2 has been used as an active reversible Li-ion battery electrode.[19] $Ni_{12}P_5$ exhibits high conductivity and has been used in hybrid battery–superconductor devices.[20] Ni_2P has been used to catalyze hydrotreatment and hydrogen evolution reactions, as described in the introduction. Ni_2P surfaces show unique and complex surface reconstructions.[21]

In the case of NOCM reactions, Ni-P/SiO_2 (Ni:P = 1:1) exhibited the highest catalytic performance among the investigated Ni phosphide catalysts. The Ni-P/SiO_2 (Ni:P = 1:1) structure corresponded to Ni_2P. More Ni-rich phosphide compounds such as $Ni_{12}P_5$ and Ni_3P exhibited lower activity. Pure metallic Ni efficiently activated the C–H bond in CH_4 and decomposed the CH_4 to coke, which poisoned and deactivated the Ni surface. In the crystal structure of Ni_2P, the shortest Ni-Ni bond length is 2.61 Å (Table 4-7). In $Ni_{12}P_5$ and Ni_3P, the shortest Ni-Ni bond lengths are 2.53 Å and 2.44 Å, respectively. These shorter bond lengths might have led to the higher activity for C–H bond cleavage in CH_4 and the formation of coke that suppressed the catalytic activity. A higher P content increases the Ni-Ni bond length, which decreases Ni activity. Thus, an appropriate Ni:P ratio provides a good balance between CH_4 activity and preventing coke formation during NOCM reactions. The Ni_2P/SiO_2 catalyst had a suitable Ni:P balance that activated a large amount of methane to the methyl radical than the $Ni_{12}P_5$/SiO_2 and Ni_3P/SiO_2 and consequently form ethane, ethylene, benzene and so on.[22] Interestingly, a CF analysis of Ni–P compounds with Ni:P = 2:1 and Ni:P = 3:1 gave Ni-Ni bond lengths of 2.52 and 2.45 Å (Table 4-7), which agreed well with the shortest values for $Ni_{12}P_5$ and Ni_3P. In Table 4-7, the theoretical data have been listed from the crystal structure information [Chapter 1 (Section 1.3)]. This good correlation is attributed to the fact that the EXAFS CF analysis is more sensitive to the rising part of the radial distribution curve or the shortest bond length.[12] When I compared the average Ni–Ni bond length for each crystal structure (Table 4-7), I could not establish a relationship between bond length and catalytic activity.

Table 4-7. Nickel-Nickel bond distances of various nickel phosphide catalysts.

Compound Name	R_{Ni-Ni} (Shortest)^{CF} (Å)	R_{Ni-Ni} (Shortest)$^{The.}$ (Å)	R_{Ni-Ni} (Average) (Å)
Ni_2P	2.62	2.61	2.65
$Ni_{12}P_5$	2.52	2.53	2.58
Ni_3P	2.45	2.44	2.60

4.7. Conclusion

In these analyses, I only used the theoretical XANES and EXAFS spectra as a reference calculated by FEFF8. By comparing the experimental and theoretical XANES data for Ni_2P, I observed that the experimental XANES peaks were broadened, and thus I concentrated on the peak position energy. Even if Ni phosphide compounds' structures were complicated, I could predict an unknown structure by comparing the experimental data with the theoretical XANES and EXAFS data without recording the spectra of the corresponding reference compounds experimentally. I demonstrated that catalysts with Ni to P ratios of 1:1, 2:1, and 3:1 consisted mainly of the Ni_2P, $Ni_{12}P_5$, and Ni_3P, respectively. The catalytic activity of SiO_2-supported Ni phosphide catalysts in NOCM followed the order Ni_3P < $Ni_{12}P_5$ < Ni_2P. Thus, the theoretical XAFS simulation approach predicted the unknown structure of supported metal catalysts with complex structures.

References

1. Gaur, A., Shrivastava, B. D. & Nigam, H. L. X-Ray Absorption Fine Structure (XAFS) Spectroscopy – A Review. *Proc Indian Natn Sci Acad Spl. Issue, Part B* **79**, 921–966 (2013).

2. Natoli, C. R., Misemer, D. K., Doniach, S. & Kutzler, F. W. First-principles calculation of x-ray absorption-edge structure in molecular clusters. *Phys. Rev. A* **22**, 1104–1108 (1980).

3. Feiters, M. C. EXCURVE Tutorial. (2014).

4. Zabinsky, S. I., Rehr, J. J., Ankudinov, A., Albers, R. C. & Eller, M. J. Multiple-scattering calculations of x-ray-absorption spectra. *Phys. Rev. B* **52**, 2995–3009 (1995).

5. Rehr, J. J. & Albers, R. C. Theoretical approaches to x-ray absorption fine structure. *Rev. Mod. Phys.* **72**, 621–654 (2000).

6. Ankudinov, A. & Ravel, B. Real-space multiple-scattering calculation and interpretation of x-ray-absorption near-edge structure. *Phys. Rev. B - Condens. Matter Mater. Phys.* **58**, 7565–7576 (1998).

7. Filipponi, A., Di Cicco, A. & Natoli, C. R. X-ray-absorption spectroscopy and n-body distribution functions in condensed matter. I. Theory. *Phys. Rev. B* **52**, 15122–15134 (1995).

8. Blaha, P., Schwarz, K., Sorantin, P. & Trickey, S. B. Full-potential, linearized augmented plane wave programs for crystalline systems. *Comput. Phys. Commun.* **59**, 399–415 (1990).

9. Müller, J. E., Jepsen, O. & Wilkins, J. W. X-ray absorption spectra: K-edges of 3d transition metals, L-edges of 3d and 4d metals, and M-edges of palladium. *Solid State Commun.* **42**, 365–368 (1982).

10. Massalski, T. B., Okamoto, H. & International., A. S. M. Binary Alloy Phase Diagrams. in *Alloy Phase Diagrams* 89–89 (ASM International, 1990).

11. Ren, J., Wang, J. guo, LI, J. fen & LI, Y. wang. Density functional theory study on crystal nickel phosphides. *Ranliao Huaxue Xuebao/Journal Fuel Chem. Technol.* **35**, 458–464 (2007).

12. Koningsberger, D. & Prins, R. *X-ray absorption: Principles, applications, techniques of EXAFS, SEXAFS, and XANES. Endeavour* **12**, (Wiley, 1988).

13. Rehr, J. J. & Albers, R. C. Theoretical approaches to x-ray absorption fine structure. *Rev. Mod. Phys.* **72**, 621–654 (2000).

14. Bosman, E. & Thieme, J. Modeling of XANES-spectra with the FEFF-program. in *Journal of Physics: Conference Series* **186**, (2009).

15. Rehr, J. J., Ankudinov, A. & Ravel, B. *User's Guide, FEFF v.8.40.* (2006).

16. Slater, J. C. Wave functions in a periodic potential. *Phys. Rev.* **51**, 846–851 (1937).

17. Hisazumi Akai. The University of Tokyo, *KKR Method* (2014). https://www.slideshare.net/cms_initiative/cmsi-38020198

18. Zhu, J. *et al.* Nanoporous Ni3P Evolutionarily Structured onto a Ni Foam for Highly Selective Hydrogenation of Dimethyl Oxalate to Methyl Glycolate. *ACS Appl. Mater. Interfaces* **11**, 37635–37643 (2019).

19. Gillot, F. *et al.* Electrochemical reactivity and design of NiP2 negative electrodes for secondary Li-Ion batteries. *Chem. Mater.* **17**, 6327–6337 (2005).

20. Gan, Y. *et al.* High conductivity Ni12P5 nanowires as high-rate electrode material for battery-supercapacitor hybrid devices. *Chem. Eng. J.* **392**, (2020).

21. Yuan, Q., Ariga, H. & Asakura, K. An Investigation of Ni2P Single Crystal Surfaces: Structure, Electronic State and Reactivity. *Top. Catal.* **58**, 194–200 (2015).

22. Dipu, A. L., Nishikawa, Y., Inami, Y., Iguchi, S. & Yamanaka, I. Development of Highly Active Silica-Supported Nickel Phosphide Catalysts for Direct Dehydrogenative Conversion of Methane to Higher Hydrocarbons. *Catal. Letters* **365**, (2021).

Chapter 5

XANES Analysis of Nickel Phosphide Complex System Using

Full Potential Multiple Scattering (FPMS)

5.1.   Introduction

X-ray absorption near edge structure (XANES) is a powerful tool to investigate the oxidation state and local structure geometry of a material. In the XANES region, multiple scattering is predominant, where single scattering is predominant in the EXAFS region. For the theoretical computation of XANES spectra, the spherical average of atoms, the so-called muffin-tin approximation, is widely adopted for the sake of simplicity of the theory. But muffin-tin approximation cannot properly describe a large number of physical systems such as low dimensional systems and systems having large interstitial space like, e.g., diamond and layered structure. For light elements, atomic potential scattering is rather weak, and thus scattering of the interstitial potential is comparatively strong. Hence full potential (FP) corrections are important. There have been attempts to extend the MS theory to FP, called as full potential multiple scattering (FPMS) theory. The real space FPMS theory with space-filling cells is valid for both bound and continuum states. It contains only one truncation parameter, maximum angular momentum $l_{max} = kR_b$, where k is the photo-electron wave vector, and R_b is the radius of the bounding sphere of the scattering cell.[1,2] In the full potential (FP) approximation, the XANES spectra show strong spectral features due to the strong scattering effects, and the peaks are sharp because of the long hole lifetimes.[3] Therefore, the FP is necessary to increase the precision of the calculations. In the previous chapter, I showed that FEFF could predict the unknown structure for Ni phosphide complex systems with some systematic error. FEFF can successfully reproduce the peaks features in the XANES spectra for the Ni_2P complex system (Figure 5-1). But due to the difference in peak shape in FEFF calculated XANES spectra at B, I observed that the peak position difference is -0.4 eV. Since FPMS is a different approach that used non-muffin tin approximation where the potential is assumed to be anisotropic in each atomic sphere, and the interstitial region contains charge density, I expect quietly good

results in the Ni_2P complex system to overcome the peak shape problem. In this chapter, the FPMS method has been applied in the Ni_2P complex system for XANES calculations and compared between FPMS (NMT) calculated XANES spectra with FEFF (MT) calculated XANES spectra.
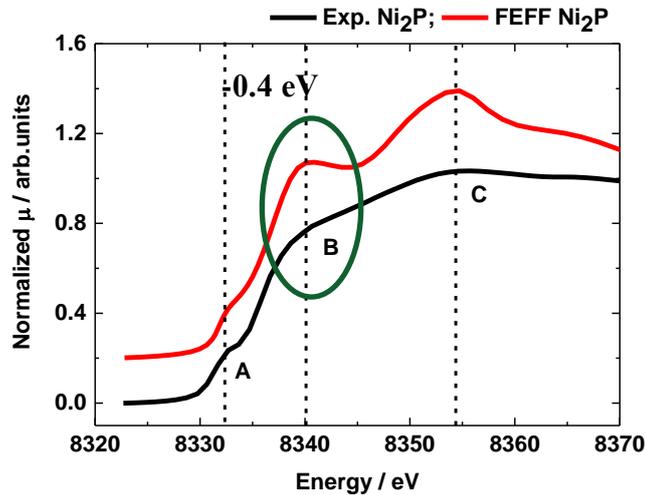

Figure 5-1.　Comparison of theoretical (FEFF) and experimental XANES for Ni_2P.

5.2.　Full Potential Multiple Scattering (FPMS) Theory

The FPMS theory with space-filling cells used here is valid for both continuum and bound states and contains only one truncation parameter, l_{max}, the maximum angular momentum of the spherical wave basis. This approach provides a straightforward extension of multiple scattering theory (MST) in the muffin-tin approximation.

5.2.1.　Multiple Scattering Theory (MST)

Multiple scattering (MS) theory is a very powerful approach to calculating the electronic structure of solids and spectroscopic response functions. It is implemented by dividing the space into the non-overlapping domain (cells), solving the differential equation separately in each of the cells, and then assembling the equation together with the partial solutions into a global solution that is continuous and smooth across the whole region and satisfies the given boundary condition. It has been widely used to solve the Schrödinger equation (SE) in quantum mechanics both for scattering and bound states. It was proposed originally by Korringa and by Kohn and Rostoker as a convenient method for calculating the electronic structure of solids.[4,5] For the application purpose of the KKR method were first made muffin-tin (MT) approximation

for the potential. The potential is separated by non-overlapping spheres in this approximation, spherically symmetrized, and the interstitial region contains a constant value.

When a photon is absorbed by an atom and a deep core electron is photo-excited, in this case, Fermi's Golden rule

$$\mu(E) \propto \sum_f |\langle f| \bar{\mathsf{E}} \rangle. r |i\rangle|^2 \delta(\omega_f - \omega_i - E) \tag{5.1}$$

Here $\mu(E)$ is the absorption cross-section as a function of incident photon energy, $|i\rangle$ and $|f\rangle$ are the initial (deep core) and final (photo-excited) states of the electron. The transition between the states is medicated by a dipole interaction $\bar{\mathsf{E}}. r$. The availability of the Geen function makes MST a versatile tool to investigate more complex systems other than the perfect crystal. With the operator associated with this Green's function, $\sum_f |f\rangle G \langle f|$, the expression for $\mu(E)$ is rewritten as

$$\mu(E) \propto \langle i| \bar{\mathsf{E}}^*. rG(r, r^{\square}; E) \bar{\mathsf{E}}. r^{\square} |i\rangle \Theta(E - E_f) \tag{5.2}$$

Where Θ is a broadened Heaviside step function assuring that $\mu(E)$ is non-zero only above the Fermi level energy, i.e., only for incident photon energies which can promote a deep core electron into an unfilled state.

G is the one-electron propagator function in the presence of the MT potential. That means that G describes all possible ways that the photo-electron can propagate away from the absorber and scatter from the surrounding atoms. The multiple scattering is successive scattering due to many potentials (Figure 5-2). The total scattering amplitude is the sum of the amplitude of those processes. G can be expressed in a series expansion as

$$G = G_0 + G_0 T G_0 \tag{5.3}$$

Here, T is the atomic scattering matrix. T is expressed in terms of the single-atom scattering matrix as

$$T = t + t G_0 t + t G_0 t G_0 t + \ \dots\dots \tag{5.4}$$

Where, t-matrix describes scattering due to each potential.

Substitute this equation into equation (5.3)

$$G = G_0 + G_0 t G_0 + G_0 t G_0 t G_0 + G_0 t G_0 t G_0 t G_0 + \ \dots\dots \tag{5.5}$$

The matrix G_0 is the free electron propagator, which describes the ways an electron can travel from one point in space to another. T is the single atom scattering matrix. It describes how an electron scatters from each atom in the cluster. The second term in equation 5.5 describes all the ways the propagates away from the absorber and scatters exactly once from a surrounding atom. The third term describes all the ways the photo-electron scatters twice, propagating between and scattering from two other atoms in the cluster. At each order of Equation 5.5, scattering is considered from all atoms in the cluster used to compute the MT potential.
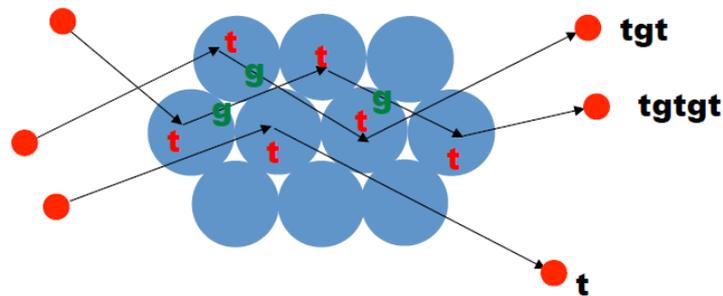

Figure 5-2. Multiple scattering due to assembly of potentials.[6]

5.2.2. Full Potential (FP) Theory

It is known that MT approximation is only good for close-packed systems and does not work perfectly for covalently bonded and low dimensional systems.[1,3,7,8] Conventional MS theory relies on the muffin-tin approximation, where the potential is assumed to be spherically symmetric in each atomic sphere, and the interstitial region contains constant potential (Figure 5-3). MT approximation is poor for the graphene-like systems because of the anisotropic charge density of the C-C σ and π bonding. Due to the poor performance of the MT approximation for both bound and continuum states, many investigate started to overcome this approach. Williams and Morgan (1974) were pioneering work to reformulate the MS theory for arbitrary local potentials by partitioning the space with space-filling truncated cells (Voronoi polyhedral) and successfully applied this to a model of crystalline silicon. When a Voronoi polyhedron does not contain an atom or is in the interstitial region but still

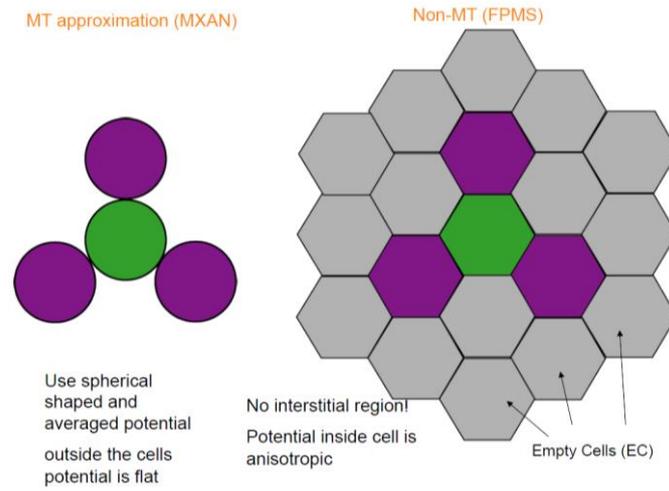contains charge density, it is called an empty cell (ES) (Figure 5-3).

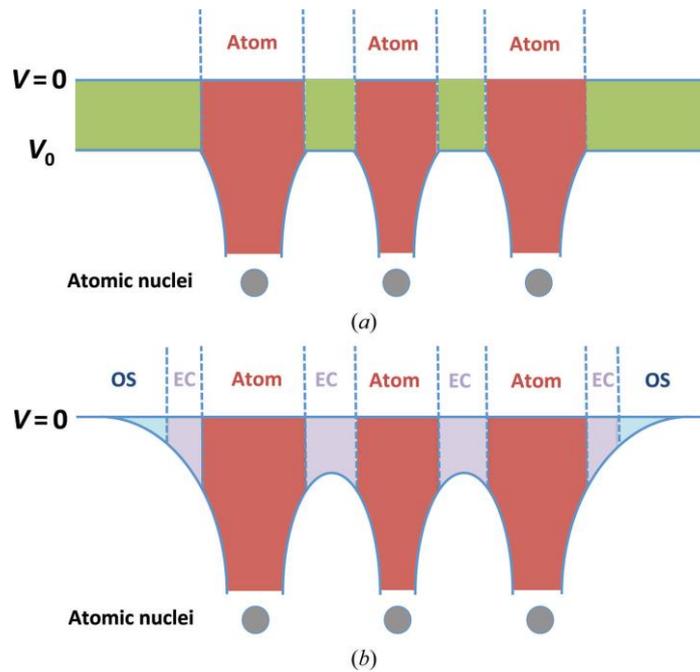**Figure 5-3.** Muffin-tin (MT) and Non-Muffin-tin (NMT) approximation.[9]

Figure 5-4. Schematic representation of the potential for a three atom molecule: a) MT case, b) FP case.[10]

The empty cell (EC) is necessary for the diamond-type lattice of silicon to adequately represent the potential in a substantial region and satisfy geometrical constraints imposed by the re-expansion of the free Green function (GF) around two sites. Figures 5-4 (a) and (b) show a schematic representation of the potential in the MT and FP cases. Hatada et al. presented the derivation of a real space FPMS theory which is valid for both continuum and bound states.[8]

5.3. FPMS Analysis

Hatada et al. developed FPMS code that uses the approximation to separate the space by truncated spheres and Voronoi cells in order to avoid overlapping spheres and remove the interstitial region.[11] These non-spherical cells are used as scattering sites for multiple scattering calculations. The FPMS code mainly focuses on calculating XANES spectra, but this code also calculates projected DOS and resonant X-ray elastic scattering. For electronic and structural studies of materials, it is important to figure out the MT approximation, especially for systems with open structures such as layers or a diamond structure. In this chapter, I have applied MT and FP approximation to calculate the XANES spectra for $GeCl_4$ to understand the FPMS analysis procedure. Then I have applied the FPMS method to calculate the XANES spectra of the Ni_2P complex system.

5.3.1. XANES Analysis of GeCl₄ Using FPMS

$GeCl_4$ has a local tetrahedral structure. For FPMS analysis, the interstitial region of the $GeCl_4$ molecule was partitioned with ten empty cells located at the sites of the BCC lattice (Figure 5-5 (a)). Figure 5-5 (b) shows that the MT approximation could never reproduce the first bump after the main peak. But in the FP approximation, I observed this peak after the main peak, consistent with the experimental XANES spectra. This characteristic peak appearance is due to the introduction of anisotropy of the potential inside the atoms and the presence of ten empty Voronoi cells in the BCC lattice.
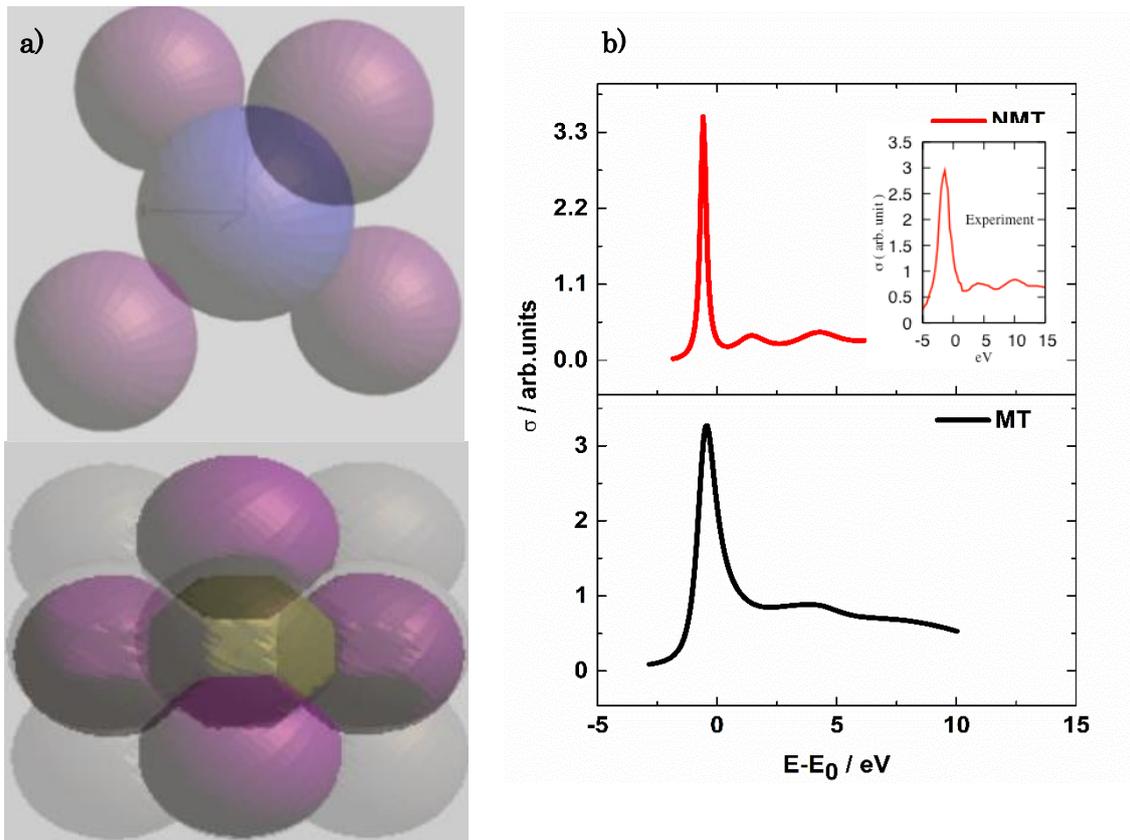
Figure 5-5. a) Partition of space in non-overlapping cells compared with an MT partition, b) compared with the MT results and experimental.

For the angular momentum, $l_{max} = 4$ was sufficient to reach convergence of the spectrum (Figure 5-6).
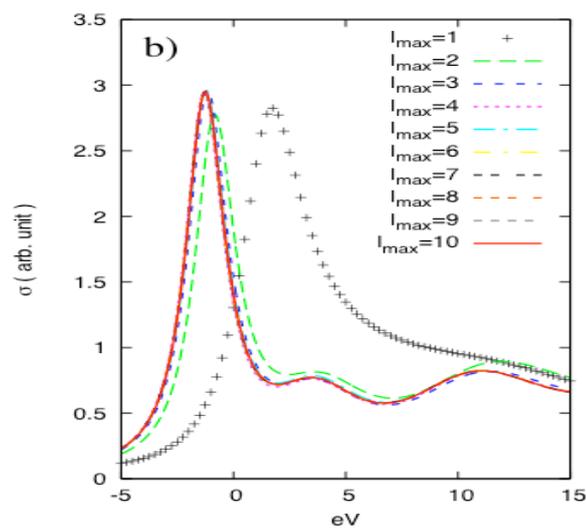

Figure 5-6. Study of convergence rate as a function of l_{max} up to $l_{max} = 10$.[1]

To execute the FPMS code, the input file name must be "data.ms". The input file of GeCl$_4$ is shown in Figure 5-7. In this case, the important parameters are shown below:

nsca = 15   ! Number of scattering sites. Normally, the converged cluster
                               radius is 5 - 8 angstrom.
typot = "xalph"   ! Type of Self-energy.
                             ! "xalph" - X-alpha XC potential
                             ! "hlcmp" - energy-dependent complex Hedin-Lundqvist self
                               energy
                             ! "hlrel" - real part of Hedin-Lundqvist self energy
                             ! "dihar" - Dirac-Hara XC potential (only exchange)

NMT = "NM"   ! "NM" - full potential; "MT" - Muffin-Tin
norman = "extrad"   ! For full potential calculation. "extrad" means the radii of
                               scattering sites (right after the Cartesian
                             ! coordinates) must be given by hands.
                             ! Be careful! norman cannot be "stdcrm". When use
                               Muffin-Tin approximation, "stdcrm" is used to decide
                             ! radii of atoms automatically by a rule.
truncate = .true.   ! Spheres are truncated so that there's no overlapping between
                               atomic and empty cells.
                             ! Normally, ".true." is necessary for full potential
                               calculation.

```
data.ms - Notepad                                                    —   □   :
File  Edit  Format  View  Help
&JOB
!!!!! General parameters
!
nsca      = 15           ! Number of scattering sites. Normally, the converged cluster radius is !
- 8 angstrom.
lmax      = 3            ! Angular moment cutoff. Normally, 3 - 5. The convergence should be
ensured! By default,
                         ! it's 0, so that lmax will be calculated automaticallly.
edge      = 'k '         ! Some examples: 'k' - K-edge; 'l2' - L2-edge; 'm4' - M4-edge.
emin      = -5.0
emax      = 30.0
delta     = 0.20
xscale    = 1.0          ! Decide energy points. Ei = Emin + delta * (i-1)**xscale
coor      = "angs"       ! Unit of length. It's the default. "angs" - angstrom. Otherwise, atomic
unit.
eng unit = "ev"          ! Unit of energy. It's the default. Otherwise, atomic unit.
!
!!!!! Full potential parameters
!
NMT       = "NM"       ! "NM" - full potential; "MT" - Muffin-Tin
norman  = "extrad"    ! For full potential calculation. "extrad" means the radii of scattering sites (right after the Cartesian
                      ! coordinates) must be given by hands.
                      ! Be careful! norman cannot be "stdcrm". When use Muffin-Tin approximation, "stdcrm" is used to decide
                      ! radii of atoms automatically by a rule.
truncate = .true.     ! Spheres are truncated so that there's no overlapping between atomic and empty cells.
                      ! Normally, ".true." is necessary for full potential calculation.
!
!!!!! Symmetry parameters
! For symmetric systems, you may need this part to speed up the calculation and save memory. Please check them in "XXX.XXX".
group_sym = "no"      ! Without symmetry
!
gl_plot  = .true.     ! Plot atoms and empty cells. The executable file should be complied with option "glut".
/
tit1
tit2
tit3
iz    x      y        z      radii  ilig   distance  comment ! For norman="stdcrm", the column "radii" is not needed.

32  0.00000  0.00000  0.00000  1.3550   0   0.00000  GE____000
17  1.21244  1.21244  1.21244  1.3550   0   0.00000  CL____eq1
17 -1.21244 -1.21244  1.21244  1.3550   0   0.00000  CL____eq2
17 -1.21244  1.21244 -1.21244  1.3550   0   0.00000  CL____eq3
17  1.21244 -1.21244 -1.21244  1.3550   0   0.00000  CL____eq4
 0  1.21244 -1.21244  1.21244  1.3550   0   0.00000  ES____eq1
 0 -1.21244  1.21244  1.21244  1.3550   0   0.00000  ES____eq2
 0 -1.21244 -1.21244 -1.21244  1.3550   0   0.00000  ES____eq3
 0  1.21244  1.21244 -1.21244  1.3550   0   0.00000  ES____eq4
 0  0.00000  0.00000  2.42488  1.3550   0   0.00000  ES____eq5
 0  0.00000  0.00000 -2.42488  1.3550   0   0.00000  ES____eq6
 0  2.42488  0.00000  0.00000  1.3550   0   0.00000  ES____eq7
 0 -2.42488  0.00000  0.00000  1.3550   0   0.00000  ES____eq8
 0  0.00000  2.42488  0.00000  1.3550   0   0.00000  ES____eq9
 0  0.00000 -2.42488  0.00000  1.3550   0   0.00000  ES____eq10
```

Figure 5-7. Data input file for Ge K-edge XANES analysis of $GeCl_4$ using FPMS.

5.3.2. XANES Analysis of Ni_2P Using FPMS

I have tested the present full potential multiple scattering (FPMS) schemes for X-ray absorption near edge structure (XANES) calculations of the Ni_2P complex system. As I described in Chapter 1, Ni_2P consists of two consecutive planes Ni_3P_2 (tetrahedral) and Ni_3P (square pyramidal). I have calculated the partial spectra of two Ni sites and then averaged the single contribution for getting total spectra.

When calculating with FPMS, input information is written in one file, and it must always be "data.ms". Cluster radius and maximum angular momentum convergence determination are important for FPMS execution. Normally the converged cluster radius is 5-8 Å, where angular momentum cutoff converged is 3-5. The convergence should be ensured. At first, the muffin-tin approximation has been applied using the Prof. Hatada coding where NMT = "MT" for muffin-tin potential. The Ni K-edge absorption was calculated with Hedin-Lundqvist (HL) potentials. $l_{max} = 4$ and $l_{max} = 3$ was sufficient to reach convergence of the spectrum for Ni (1) and Ni (2) site, respectively (Figure 5-8).

Good convergence was observed for a cluster radius of about 7Å for both Ni sites (Figure 5-9). Then the single contribution of each Ni site was summarized to calculate XANES spectra of Ni_2P for MT approximation.
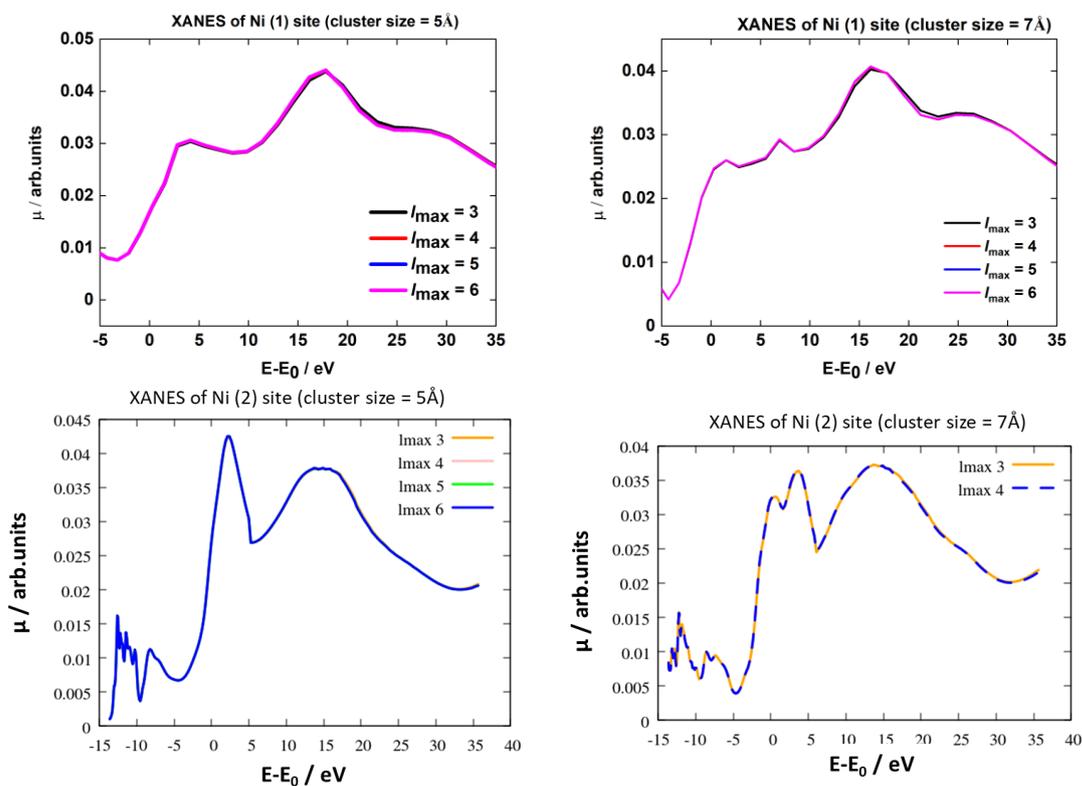

Figure 5-8. Convergence determination of angular momentum l_{max} for Ni (1) and Ni (2) site at 5Å and 7Å cluster size.
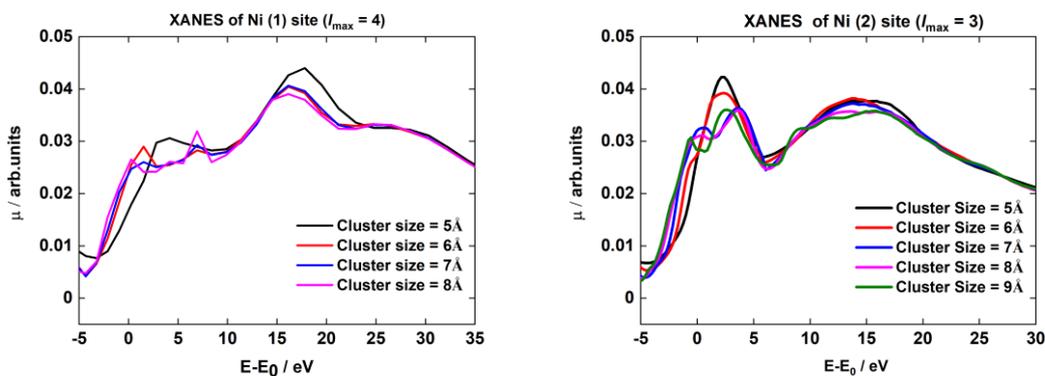

Figure 5-9. Convergence determination of cluster size for Ni (1) and Ni (2) site at l_{max} =4 and l_{max} = 3 respectively.

For full potential (FP) calculations, various parameters were changed in data.ms" input file. In the input file, for FP calculations NMT parameter was "NM". For full potential calculations, norman = "extrad" means the radii of scattering sites which must be given a hand in the input file. I selected the radii for FP calculations as MT radii*1.6. I changed the constant value from 1.0 to 1.6 in 0.2 steps, and I found that 1.6 is large enough to fill the space with cells in Ni_2P (Figure 5-10). Then I found a XANES spectrum of Ni_2P using FPMS, as shown in Figure 5-11.

Scale factor 1.4   Scale factor 1.2

Scale factor 1.4   Scale factor 1.6
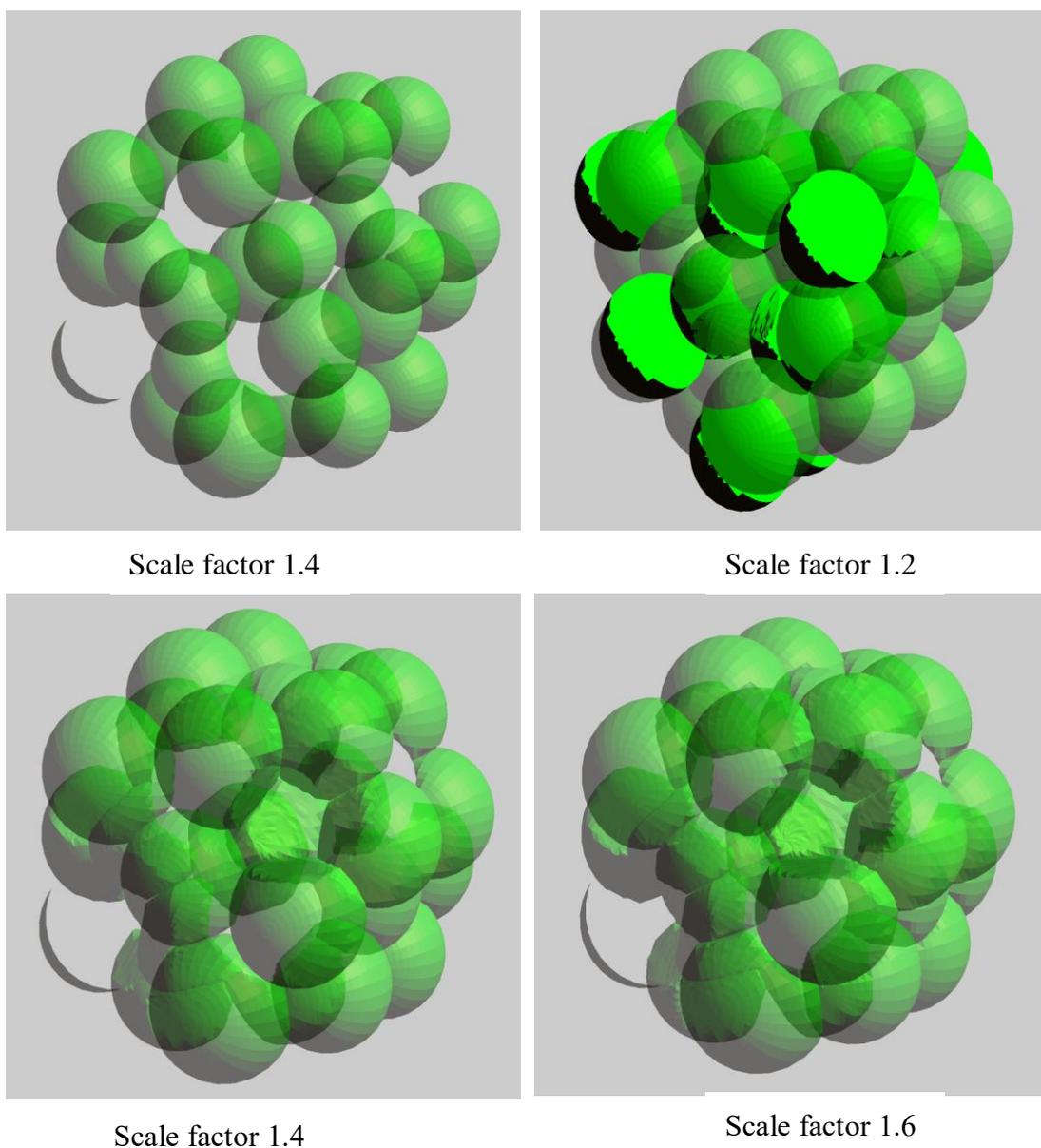
Figure 5-10.   Radii of each cell in Ni_2P complex system.
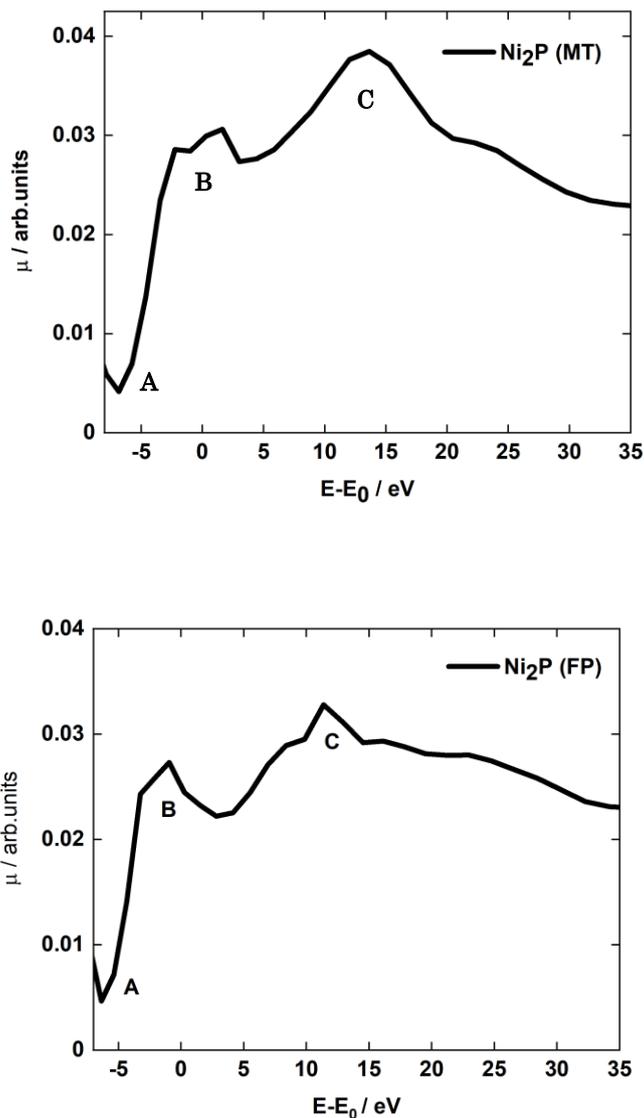
Figure 5-11. Ni K-edge XANES spectra of Ni$_2$P for MT (Prof. K. Hatada coding) and FP using FPMS coding.

5.4. Results and Discussion

5.4.1. Comparison between FEFF Calculated XANES Spectra and FPMS Calculated XANES Spectra

Figure 5-12 shows the comparison of Ni K-edge XANES spectra of Ni$_2$P for the Prof. K. Hatada coding muffin-tin (MT), full potential (FP), FEFF, and experimental analyzing results. In the MT and FP calculated XANES spectra, I found that pre-edge

peak A and the oscillatory features between peak B and C. For FP calculated XANES spectra, the peak features were sharper than the MT calculated XANES spectra. On the other, the experimental and FEFF calculated XANES spectra of Ni_2P had significant A, B, and C peak features that were different from the MT and FP peak features.
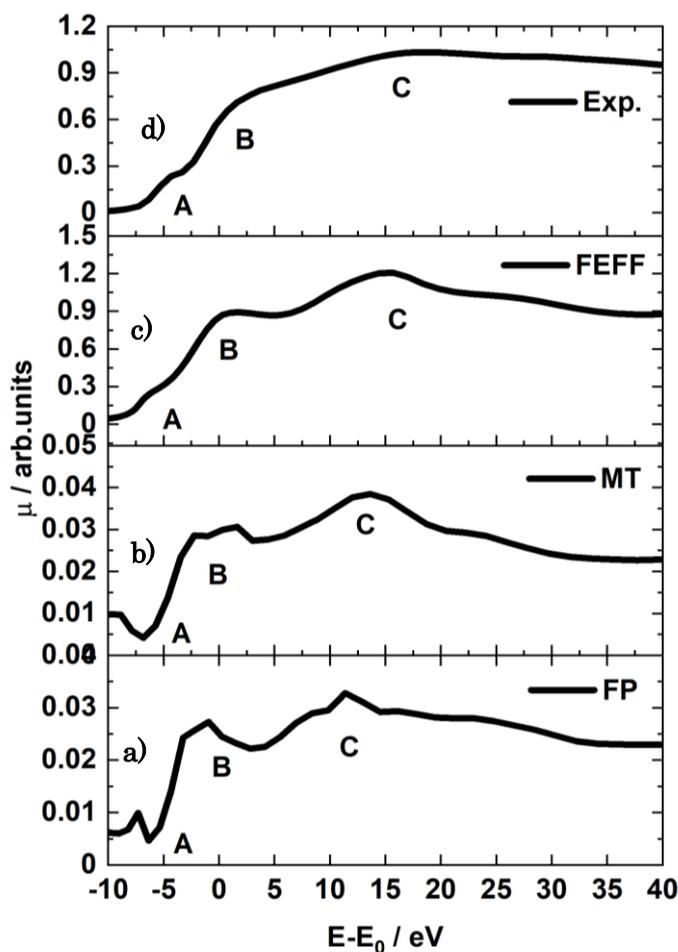
Figure 5-12. Comparison of Ni K-edge XANES spectra in the experimental, FEFF, Muffin-tin (MT, Prof. K. Hatada coding), and Full potential (FP) analyzing results.

The FP calculated XANES spectra had only a vague pre-edge peak position compare to the FEFF. In contrast, B and C peak features were zigzag types in FPMS calculated XANES spectra. But FEFF calculated XANES spectra given clear B and C peak features that agreed well with experimental Ni_2P XANES spectra. Figure 5-12 (b) XANES spectra was calculated by the FPMS executive file where the full potential parameter was "MT" in the input file. This spectrum should be the same as FEFF

calculated XANES spectra (Figure 5-12 (c)), because both potentials were calculated using muffin-tin approximation. But in this case, the peak features of MT (Prof. K. Hatada coding) did not correspond with FEFF. This result was indicating some of the parameters in the data.ms input file did not work well. So, I have to concentrate on the input file parameters to get good results using the FPMS method.

5.4.2. Drawback During FPMS calculations

FPMS is a brand new method for XANES calculations. For the first time, I have tried to apply this method for XANES calculation in the Ni phosphide complex system. This analyzing result was not expecting. Dring the calculations of XANES spectra using FPMS, I faced some problems during the XANES calculations using FPMS: 1) FPMS is a time-consuming program than the FEFF. It takes a long run time to execute the FPMS data file. 2) Peak resolution determination is one of the serious problems for FPMS analysis. Basically, peak resolution can be controlled by "Ei = Emin + delta * (i-1)**xscale". But it is not easy to find out suitable peak resolution parameters. 3) Radius of scattering site and empty cell determination is also difficult for the FPMS calculations. Due to the lack of a user guide in English, I cannot execute the input file properly. I need to adjust some parameters to get the good XANES spectra using FPMS. I will continue the FPMS analysis; after that, I can expect high-quality XANES spectra for Ni_2P using the FPMS method.

5.5. Conclusions

I have presented FPMS calculations for XANES of Ni_2P. The Ni K-edge XANES spectra contain zigzag peak features above edge. The FPMS analyzing results have been compared with the experimental results. Unfortunately, I did not get a good agreement with the experimental spectra as well as FEFF spectra for the Ni_2P complex system. The FPMS studying spectra show three peak features with a zigzag pattern in the Ni_2P XANES spectra. FPMS is still developing to overcome this problem. I expected that I would be able to adjust these peak features with experimental XANES spectra in the future.

Reference

1. Hatada, K., Hayakawa, K., Benfatto, M. & Natoli, C. R. Full-potential multiple scattering for x-ray spectroscopies. *Phys. Rev. B - Condens. Matter Mater. Phys.* **76**, (2007).

2. Hatada, K., Hayakawa, K., Benfatto, M. & Natoli, C. R. Full-potential multiple scattering theory with space-filling cells for bound and continuum states. *J. Phys. Condens. Matter* **22**, (2010).

3. Xu, J. *et al.* X-ray absorption spectra of graphene and graphene oxide by full-potential multiple scattering calculations with self-consistent charge density. *Phys. Rev. B - Condens. Matter Mater. Phys.* **92**, 1–11 (2015).

4. Kohn, W. & Rostoker, N. Solution of the schrödinger equation in periodic lattices with an application to metallic lithium. *Phys. Rev.* **94**, 1111–1120 (1954).

5. Korringa, J. On the calculation of the energy of a Bloch wave in a metal. *Physica* **13**, 392–400 (1947).

6. Hisazumi Akai. The University of Tokyo, *KKR Method*. (2014), https://www.slideshare.net/cms_initiative/cmsi-38020198

7. Hatada, K., Hayakawa, K., Benfatto, M. & Natoli, C. R. Full-potential multiple scattering for core electron spectroscopies. *J. Phys. Condens. Matter* **21**, (2009).

8. Hatada, K., Hayakawa, K., Benfatto, M. & Natoli, C. R. Full-potential multiple scattering theory with space-filling cells for bound and continuum states. *J. Phys. Condens. Matter* **22**, (2010).

9. Hatada, K. & Maurizio, B. *XANES: MXAN and FPMS codes*. https://www.iucr.org/__data/assets/pdf_file/0004/60781/IUCr2011-XAFS-Tutorial-Hatada.pdf

10. Hatada, K., Xu, J., Hayakawa, K. & Natoli, C. R. FPMS : full potential multiple scattering. IT 1–5 (2020).

11. K. Hatada, J. Xu, K. Hayakawa, C. R. N. FPMS : Data analysis for XANES spectra by NON-Muffintin. (2005). Available at: https://www.lnf.infn.it/theory/CondensedMatter/fpms.html.

12. Bethe, H. A. & Salpeter, E. E. Quantum mechanics of one and two-electron systems. *Encycl. Phys.* **35**, (1957).

Chapter 6

General Conclusion

In this thesis, I have successfully revealed the local structure of silica-supported Ni phosphide with different Ni:P ratios by X-ray absorption fine structure (XAFS) and determined the unknown structure for non-oxidative coupling of methane (NOCM) reactions. I have shown that the XAFS analysis is powerful to unveil the structure of the complex system, which is sensitive to the local structure of the supported metal catalysts and is usually used to determine the structure. I have demonstrated the further use of XAFS than ever believed. The followings are the summary of my findings. These findings open a new way to bring the catalysis field to real science.

Ni-P/SiO$_2$ with different initial Ni:P ratios 1:1, 2:1, and 3:1 are investigated for NOCM reactions. The unknown structure of Ni-P/SiO$_2$ with different Ni:P ratios samples was determined using the XAFS (XANES and EXAFS) technique. The initial Ni:P ratio strongly influences the Ni phosphide structure. In contrast, Ni phosphide has seven different phases, namely Ni$_3$P, Ni$_{12}$P$_5$, Ni$_2$P, Ni$_5$P$_4$, NiP, NiP$_2$, and NiP$_3$. The conventional curve fitting results demonstrated that Ni-P/SiO$_2$ with initial Ni:P ratio 1:1 had a Ni$_2$P phase for NOCM reaction. Interestingly, the schematic mol ratio of Ni:P is 1:1, where the formation mol ratio of Ni:P was 2:1 for Ni$_2$P structure. More P had been used to prepare the Ni$_2$P structure because some of the P is evaporated under reduction or ultra vacuum conditions. Less P induces the phase transition to Ni$_{12}$P$_5$ or the other phase. This result is indicating the excess P to modify the properties of nickel phosphide catalyst.

Due to the limitation of degrees of freedom, the CF EXAFS analysis of complex structures has problems. So the conventional curve fitting EXAFS analysis cannot reveal the others two unknown sample's structures with different initial Ni:P ratios of 2:1 and 3:1 without reference spectra. Therefore, I tried to determine the structure of Ni-P/SiO$_2$ samples with different initial Ni:P ratios1:1, 2:1, and 3:1, by the X-ray absorption near edge structure (XANES) using the theoretical method. The theoretical FEFF method has been used for the calculation of reference spectra used as pattern fitting. The experimented and theoretical XANES spectra of Ni$_2$P confirmed the validity for the prediction of unknown complex structures. Then, the XANES spectra of Ni-P/SiO$_2$ with different initial Ni:P ratios 1:1, 2:1, and 3:1 were compared with the theoretical reference

119

XANES spectra. The pattern fitting results of XANES spectra confirmed that the Ni:P ratio of the 1:1 sample generated Ni_2P, which ensured the EXAFS CF results, where $Ni_{12}P_5$ and Ni_3P phases were introduced with the change Ni:P ratios as 2:1 and 3:1 respectively. The theoretical EXAFS data were also simulated to compared with the experimental EXAFS data using the theoretical FEFF method. Here, I carried out an EXAFS simulation based on the crystal structure using FEFF. This approach was different from the CF method. The theoretical EXAFS data were successfully reproduced the experimental EXAFS data. It was ensured that the theoretical model which produced the experimental data well could predict the unknown complex structure.

I observed the effect of the Ni:P ratio on the structure and activity of the catalysts. The suitable amount of Ni:P ratio controls the NOCM catalytic activity. Since Ni_2P is the most active phase for NOCM reactions than the other two, so Ni_2P/SiO_2 had the best balance of Ni:P ratio. Another important parameter, Ni-Ni bond distance, played an important role in catalytic activity. In the Ni_2P structure, the shortest Ni-Ni bond distance is 2.61 Å, where the shortest bond distance of $Ni_{12}P_5$ and Ni_3P are 2.53 Å and 2.44 Å, respectively. These results demonstrated that the moderate bond lengths of Ni-Ni balanced the C–H bond cleavage in CH_4 and the formation of coke that suppressed the catalytic activity.

Another brand new theoretical method full potential multiple scattering (FPMS) were used to calculate the XANES. This method is different from the conventional FEFF method. This method based on the absorption signal calculated in the FP approximation sometimes proves excellent fits to the experimental spectra. However, I expected a better result from this new theoretical approach. But unfortunately, the results were not satisfying. The selection of parameters was not appropriate for the reproduction of XANES spectra of Ni_2P structure. It might be a lack of calculations of the radius of the scattering sites with others input data. Suitable input parameters and speed of calculations were the main problems for this calculation. We need many further studies to improve the FPMS analysis and the applicability to the unknown structure determination.

In summary, the XAFS method can determine the local structure around metal and provide us quantitative and qualitative information. Furthermore, the theoretical approach determines the unknown complex structures without experimental reference. I have revealed that Ni_2P is the most active phase for methane conversion reactions. Moreover, I have established a relation between structure and catalytic structure in this thesis, which is important for developing the new active Ni phosphide catalyst. I hope this thesis has made an epoch for the XAFS analysis in this new century.